Diffusion and Weak Turbulence in Capillary Waves and in the Complex Ginzburg-Landau Equation

Elsebeth Schröder
Niels Bohr Institute
University of Copenhagen
e-mail: schroder@nbi.dk

April 28, 1997

Contents

Introduction

The central issue of this thesis is the diffusion of tracers in weak turbulence. Specifically, we consider the motion of particles in capillary surface waves and in the complex Ginzburg-Landau equation.

There are two possible descriptions of fluid dynamics, the Eulerian and the Lagrangian. In the more common Eulerian description the focus is on the motion at a particular location. A set of dynamical variables, e.g. the fluid velocity, entropy, characterizes the fluid dynamics at this position. The entire flow is described through a set of dynamical fields.

In contrast, the Lagrangian description emphasizes the dynamics of the so-called fluid elements, that is, small volume elements of the liquid flow. Specifying the detailed motion of the set of such elements also provides a complete specification of the fluid dynamics. The Lagrangian description of fluid dynamics can be experimentally visualized by adding particle tracers, which are assumed to follow the path of the displaced fluid elements.

We study the diffusion of single particles and of pairs of particles. In principle, the motion of one particle and the motion of pairs of particles should yield the same information, since they are measured as tracers in the same background field. However, little is know theoretically about the relation between the two types of measurements, and it is therefore of interest to study both single-particle motion and the relative motion of pairs of particles. Measurements of the relative motion of pairs emphasizes the flow on length scales at or below the distance of the two particles, whereas the single-particle motion is affected by flows on all length scales.

In turbulence the wavenumber scales at which the energy enters the system (at the source) and the wavenumber scales at which the energy leaves the system (at the sink) are well separated. The range in-between is called the inertial range, and it is assumed that energy cascades through this range from the source to the sink in a manner independent of the actual composition of the source and the

sink.

As opposed to fully developed turbulence, weak turbulence is characterized by the presence of small-amplitude homogeneous-background waves. In the theory of weak turbulence the nonlinearity of the background waves is assumed to be small. This enables an expansion of the system in the parameter of the small nonlineary, which leads to a truncation of the otherwise infinite hierarchy of correlation functions in turbulence theory. Such are the systems we consider here.

This thesis is based on work that was partially reported in the following five papers:

Paper I E. Schröder, J. S. Andersen, M. T. Levinsen, P. Alstrøm, and W. I. Goldburg, *Relative Particle Motion in Capillary Waves*, Phys. Rev. Lett. **76**, 4717 (1996).

Paper II G. Huber, E. Schröder, and P. Alstrøm, *Self-diffusion and relative diffusion in defect turbulence*, Physica D **96**, 1 (1996).

Paper III E. Schröder, M. T. Levinsen, and P. Alstrøm, *Fractional Brownian Motion of Particles in Capillary Waves*, preprint [to appear in Physica A **239** (1997)].

Paper IV O. Törnkvist and E. Schröder, *Vortex Dynamics in Dissipative Systems*, Phys. Rev. Lett. **78**, 1908 (1997).

Paper V A. E. Hansen, E. Schröder, P. Alstrøm, and M. T. Levinsen, *Fractal Particle Trajectories in Capillary Waves, Imprint of Wavelength*, preprint (submitted for publication).

The thesis is organized as follows. The first four chapters are related to diffusion measurements of particles in surface waves in the Faraday experiment. **Chapter 1** describes the setup of the Faraday experiment and explains how the particle positions are measured. **Chapter 2** introduces the *relative diffusivity* and discusses some of the many definitions thereof. The major part of the chapter contains the particle-pair data analysis. In **Chapter 3** the theory of weak turbulence is described and from this we derive a prediction which is compared to the particle-pair measurements. **Chapter 4** is concerned with the diffusion of individual particles in the Faraday experiment.

The theme of the two last chapters is diffusion and vortex motion in the complex Ginzburg-Landau (CGL) equation. **Chapter 5** contains a short introduction to the CGL equation and a description of diffusion measurements in the CGL equation. In **Chapter 6** we derive an expression for the vortex velocity in the CGL equation. The **Papers I–V** are reproduced at the end of the thesis.

I wish to thank my collaborators, my colleagues, and my friends and family near and far for much appreciated inspiration, help, and encouragement during my time as a student at the Niels Bohr Institute and as a visitor at Boston University. I am grateful to all of you — *tusind tak!*

This thesis is in submitted in partial fulfillment of the requirements of the Ph.D. degree in Physics at University of Copenhagen. The work was supported by the Danish Natural Science Research Council (SNF) and by the Fulbright Commission.

Chapter 1

Diffusion in Surface Waves

In the following four chapters we investigate the motion of particles on fluid surfaces. We describe measurements in the Faraday experiment, introduced below, of particles moving in capillary waves, and we compare the Faraday measurements to theoretical predictions and to oceanographic and atmospheric measurements.

This chapter concentrates on the Faraday experiment. The experiment is described, the necessary notation for the ensuing data analysis is introduced, and a short discussion of capillary and gravitational surface waves is given. The experiment described in the following chapters is reported in Papers I, III, and V.

1.1 The Faraday Experiment

A simple, yet enticing, experiment is the vertical vibration of a fluid, on which surface waves may form if the amplitude of vibration exceeds a certain critical value. The surface waves created by such vertical vibrations were first studied by Faraday [2] in 1831 and by Lord Rayleigh in 1883 [3]. They observed that if the vibration amplitude $\mathcal{A}$ exceeds some critical amplitude $\mathcal{A}_c$, standing waves will form on the surface. The waves will exhibit a standing wave square pattern; see Fig. 1.1. This instability of the surface is of the parametric type; in this case the frequency of the standing waves is half the driving frequency. When the amplitude $\mathcal{A}$ is slightly increased, the surface pattern becomes somewhat disordered by the occurrence of moving defects. These defects result from the transverse amplitude modulational (TAM) instability. For water this happens at such a small increase of $\mathcal{A}$ that, in reality, a perfect square pattern, like the one shown in Fig. 1.1 where the fluid is ethanol, is not seen. The waves obey a dispersion relation, which relates the wave frequency to their wavelength. In

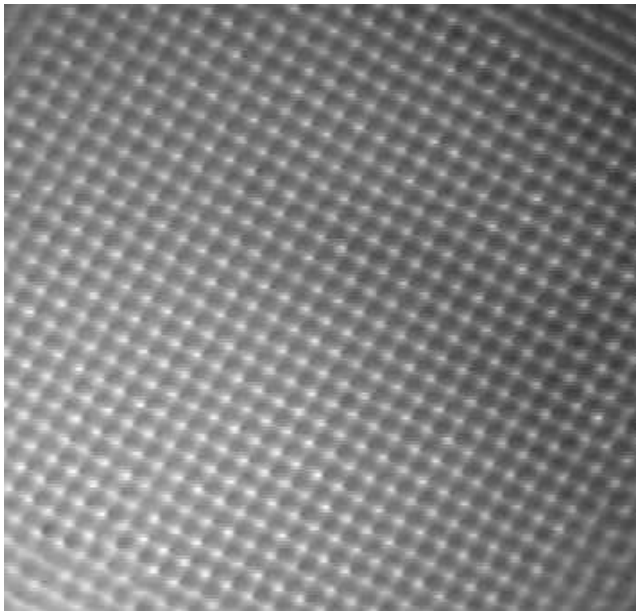

Figure 1.1: The Faraday experiment. Square pattern formed by the capillary waves right above the critical vibration amplitude $\mathcal{A}_c$. In this case the fluid was ethanol, and the driving frequency was 400 Hz. By O. Klembt Andersen, J. Sparre Andersen, and M. Stoklund Johansen.

our experiment the external conditions are such that the waves formed have a small wavelength. This means that they obey the dispersion relation for capillary waves. A short discussion of capillary and gravitational waves is given at the end of this chapter.

When increasing $\mathcal{A}$ to 10% or more above $\mathcal{A}_c$, nonlinear wave interactions become important and the defects dominate. The wave pattern becomes random in appearance, however, on time averaging the motion of the surface over many oscillation periods, the square pattern remains discernible [4]. This indicates that the long-range correlations of the capillary waves are not destroyed. The flow is spatio-temporally chaotic, not fully turbulent. Most of our measurements were in this region.

Since measurements are relatively easily made in this system, it has become an important system in many respects. For studying pattern formation [5], the aspect ratio can be varied by varying the driving frequency, and the amplitude $\mathcal{A}$, which acts as the control parameter around the instability, can be tuned by changing the voltage applied to the vibrator (see below). The surface wave pattern can be seen by eye, and can be measured by shadow graphs [6]. The

pattern formation is not yet fully understood from a theoretical point of view [7, 8, 9].

Also, since the system exhibits spatio-temporal chaos, it is of considerable interest to measure particle motion on the surface. This motion can be quite complex, as observed by Ramshankar, Berlin, and Gollub (RBG) [10, 11]. Inspired by their measurements of single particle motion and of spreading of dye on the surface of capillary waves in the Faraday experiment we measured both single particle motion and relative motion, i.e. the motion of one particle as seen from another particle.

1.2 Experimental Setup

In the following, a short description of the setup for recording particle motion in the Faraday experiment is given. The aim is to give a description as seen from a theoreticians point of view. A more detailed description of the experimental setup can be found in Ref. [12].

The container used to store the fluid is a cylindrical dish with an interior diameter of 8.4 cm and a height of 2 cm, filled with water up to a height of approximately 1 cm. The container is fixed to a vibration exciter, which is driven by a sinusoidal signal originating from a frequency synthesizer; see Fig. 1.2. The amplitude $\mathcal{A}$ of the vibrations is proportional to the voltage applied to the exciter, and this applied voltage is the actual control parameter in the experiments. The driving frequency is 260 Hz, which gives the standing waves a frequency of 130 Hz and a wavelength $\lambda = 2.6$ mm.

For the diffusion measurements, floating particles are sprinkled on the surface. The particles used are mushroom spores. They were chosen because of their low mass density and small size (approximately 50 μm), and, more importantly, because they strongly resist being wetted by water, assuring that they will float. When light is shone at a small angle at the surface the particles reflect the light, and images of the particles can be recorded by a charge-coupled device (CCD) camera. The light sources are placed so as to minimize the reflection from the waves, but not all such unwanted reflections can be eliminated at this stage.

The images from the CCD camera are recorded on a VCR tape. The images are later fed into a frame grabber board in a personal computer by replaying the VCR tape, while letting the computer find and store the position of some of the particles at time intervals of 20 ms. To allow for particle positions to be recorded

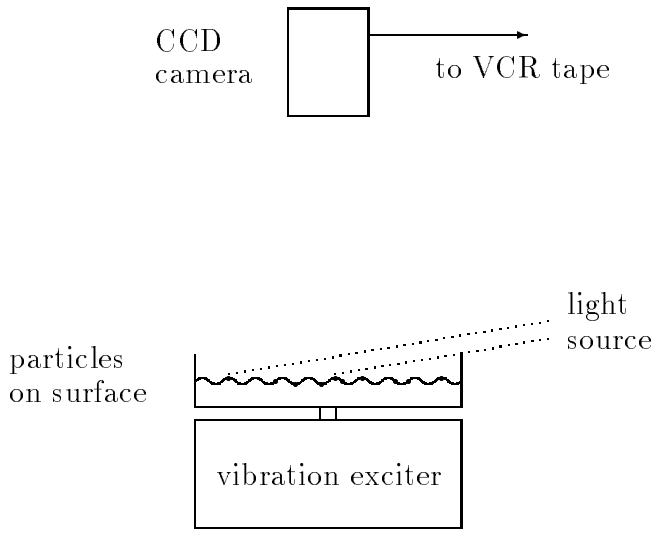

Figure 1.2: The Faraday experiment. Schematic drawing of the experimental setup for the recording of particle images.

in the computer memory the VCR tape has to be replayed at a reduced speed of about one-fifth of the data recording rate.

As a start, the tracking program arbitrarily selects four bright spots in an image. As noted above, some of these spots may be reflections from the waves instead of particles. However, many of these wave reflections have less intensity than the reflections from the particles, and may therefore be excluded by raising the threshold intensity for identifying a particle. For each of the four particles thus found in one image, the next horizontal coordinate $(x(t_i), y(t_i))$ is identified by searching a box of side length approximately 4 mm, centered on the prior coordinate $(x(t_{i-1}), y(t_{i-1}))$ [where $t_i - t_{i-1} = \Delta t = 20$ ms, the time between two images]. If the program fails to find a particle within this box, the track is ended, and the program randomly chooses another particle to track. If more than one particle appears in the search box, the program chooses the one closest to the prior position. Particle tracks consisting of less than 100 time steps (= 2 s) are discarded. This way, the remaining reflections from the waves are excluded, because they usually do not appear in more than a few subsequent images.

The lengths of the particle tracks are limited by the size of the camera window (circular with a radius of 3 cm $\approx$ 70% of the dish radius) and by the fact that at the reduced speed the VCR automatically stops after a time corresponding to approximately 3000–5000 time steps[1]. Furthermore, particle tracks that at some

[1]This restriction can be removed with the use of a sufficiently fast personal computer that

point become separated by a distance smaller than or comparable to the pixel size are discarded, because the tracks measured after that point can be the track from either particle, leading to an ambiguity in the analysis. The size of a pixel is ≈ 0.1 mm in the x-direction and ≈ 0.3 mm in the y-direction. The longest tracks that were measured consist of the order of a few thousand data points.

In terms of the reduced control parameter $\epsilon \equiv (\mathcal{A} - \mathcal{A}_c)/\mathcal{A}_c$ we measured the particle trajectories for the seven values $\epsilon = 0.05$, 0.13, 0.24, 0.34, 0.65, 0.86, and 1.06. At the value $\epsilon = 0.05$ the square pattern is no longer clearly visible, but there are hints of a pattern, whereas at $\epsilon = 1.06$ the system is closer to being (fully) turbulent. In the range between these extremes, the system is spatio-temporal chaotic with a length scale. For each vibration amplitude approximately 1000 particle tracks were recorded. From these, we analysed the single particle motion and the relative motion. Similar measurements of single particle motion were reported in Ref. [10], but at smaller vibration amplitudes ($\epsilon = 0.04$ to 0.4) and with larger particles (diameter 2-4 times larger).

1.3 Notation and Tools

Thus having obtained a number of particle tracks at several vibration amplitudes, we can proceed with a statistical analysis of the data. As mentioned in the Introduction, it is of interest to study both the dynamics of single particles and the relative motion of pairs of particles. We study the horizontal motion of particles on the fluid surface, and neglect the small vertical motion resulting from the vertical motion of the waves. We are interested in the statistical properties of the motion, and experimental realisations of the averaging procedures must be introduced. These will be discussed here, while further data analysis of the particle motion will be discussed in later chapters.

At this point, it is worthwhile to define some of the notation that will be used below and in later chapters. The horizontal position of the ith particle at time t is given by $\boldsymbol{r}_i(t) = (x_i(t), y_i(t))$, and the distance traveled in e.g. the x-direction in a given time interval τ is $\Delta x_i(\tau) = x_i(t+\tau) - x_i(t)$. The difference vector between the two particles i and j is given by $\boldsymbol{R}_{ij}(t) = \boldsymbol{r}_j(t) - \boldsymbol{r}_i(t)$; see Fig. 1.3. The indices will often be omitted. The time unit between two images, the sampling time, is $\Delta t = 20$ ms, which is the shortest time scale available in this experiment.

can track the particles at the real-time speed of the VCR tape. This was not possible at the time of processing the data, but it may become possible in the near future.

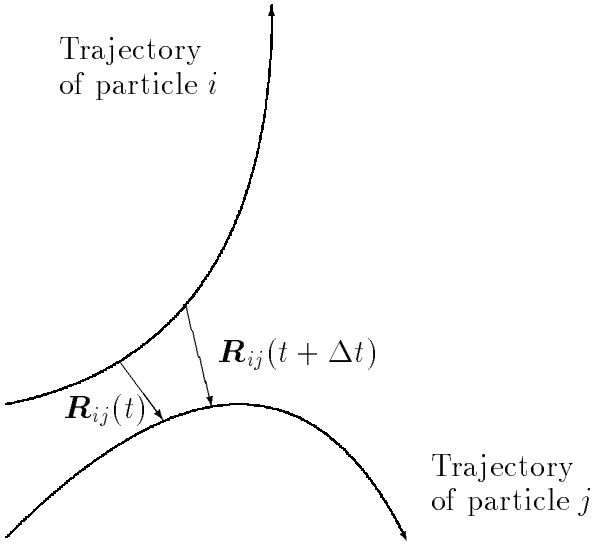

Figure 1.3: Illustration of the relative coordinate $\boldsymbol{R}_{ij}$. $\Delta t = 20$ ms is the time interval between two images of the particles.

Any other time interval (usually an integer multiple of Δt) is generally denoted by τ or $s\Delta t$.

An example of a particle trajectory obtained in the Faraday experiment is shown in Fig. 1.4. The area shown is approximately 15% of the area covered by the camera window (and about 7% of the fluid surface). The spatial resolution of the particle positions is limited by the pixel size. This is seen as a raggedness of the trajectory in Fig. 1.4. The resolution of the trajectory is better in the x-direction than in the y-direction, a consequence of the pixel size in the y-direction being about three times that of the x-direction. A particle is smaller than a pixel.

For the single particle motion, we employ the following averaging method. It involves a summation over the N particle tracks that where measured for a given value of the control parameter ϵ, and a summation over all possible subdivisions of each track. The average of some function g reads

$$\langle g[\Delta x(\tau)]\rangle = \frac{1}{N}\sum_{k=1}^{N}\frac{\Delta t}{T_k-\tau}\sum_{s=1}^{(T_k-\tau)/\Delta t} g\left[x_k(s\Delta t+\tau)-x_k(s\Delta t)\right] \qquad (1.1)$$

The duration of the kth particle track is T_k, which is an integer multiple of the sampling time Δt.

The variance of particle displacements in one direction, i.e. the quantity $V(\tau) = \langle[x(t+\tau)-x(t)]^2\rangle$, is calculated for each of the seven values of ϵ. We find that for length scales larger than the wavelength λ the variance grows almost

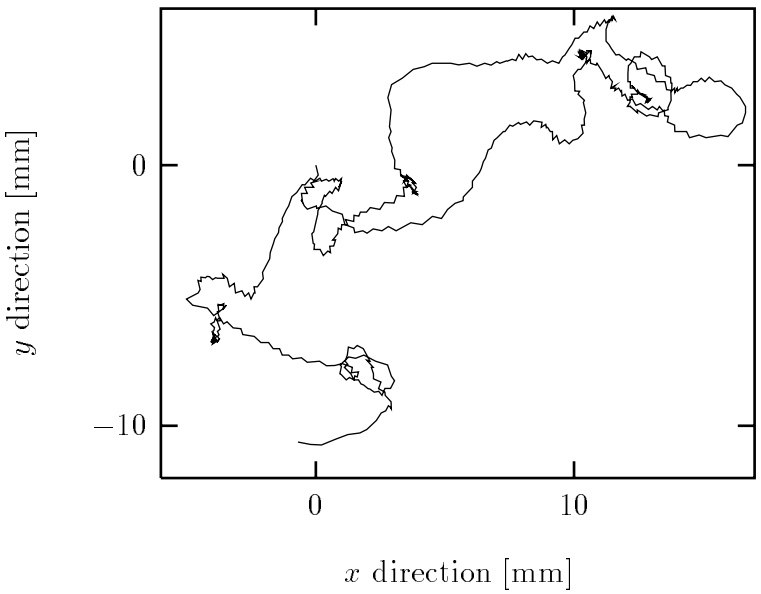

Figure 1.4: The Faraday experiment. The trajectory of a particle at control parameter $\epsilon = 0.34$. The coordinate system is translated to have origo at the starting point of the particle trajectory.

linearly with the time interval τ, as would be expected for Brownian motion. The smaller length scales have a powerlaw dependence with an exponent of approximately 1.55. However, values of the exponents (for large and small length scales) show some dependence on ϵ. This dependence will be investigated theoretically in a later chapter.

By studying the motion of pairs of particles, as opposed to single particles, other aspects of the flow are illuminated. In this experiment, we consider pairs of particles that at some point in time are 'close' together, and we follow their relative motion. According to Richardson [1], the particles will move apart at a rate that increases as the distance between the particles grows. For this reason, we are interested in the motion of the particles after they were 'close'. We let the condition for two particles being 'close' be that their relative distance is 4 mm or less (although at least a pixel size apart); see Fig 1.5. We measure the rate, at which they drift apart, through the relative diffusivity $\langle dR^2/dt \rangle_{\tilde{R}}$, where $R = |\boldsymbol{R}|$ is their separation. The average is over all occurrences of particle pairs where the separation R is in the interval $\tilde{R} - \eta$ to $\tilde{R} + \eta$ with $\eta = 0.5$ mm. The index $\tilde{R}$ will be left out when it is clear from the context which averaging scheme is used. This is the case in most parts of this text.

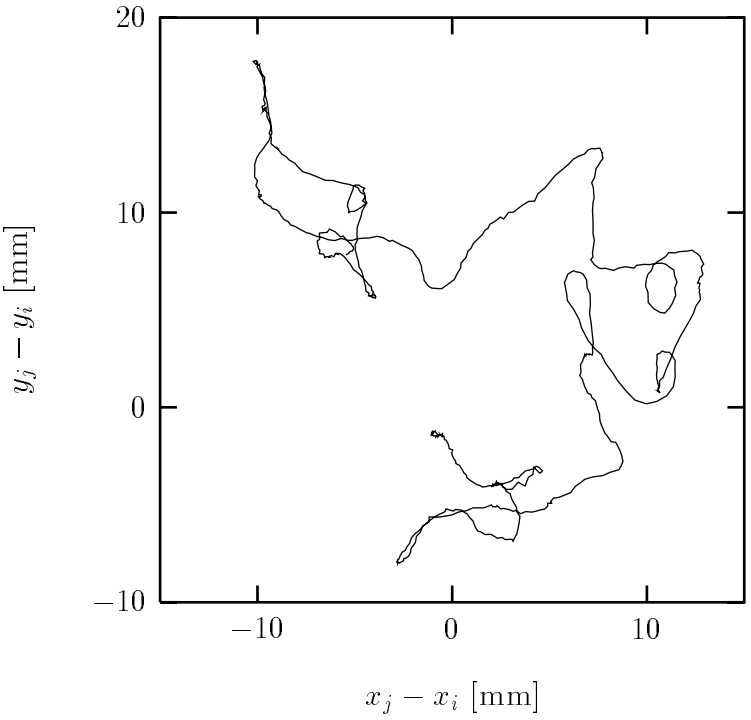

Figure 1.5: The Faraday experiment. The trajectory of one particle as viewed from another particle (relative coordinates), at control parameter $\epsilon = 0.24$. The track starts when the two particles are sufficiently close together [here: at distance vector $\boldsymbol{R} = (-0.47\ \text{mm}, -1.31\ \text{mm})$]. The length of the relative track is 640 units of Δt, i.e. almost 13 s.

We use $\Delta(R^2)/\Delta t$ as an experimental measure of this relative diffusivity. This measure also expresses the difference in the longitudinal particle velocity $\delta v_{\|}(R) = \delta \boldsymbol{v} \cdot (\boldsymbol{R}/R)$

$$\begin{aligned} \frac{\Delta(R^2)}{\Delta t} &= \frac{(\boldsymbol{R}(t) + \delta \boldsymbol{v}\, \Delta t)^2 - \boldsymbol{R}^2(t)}{\Delta t} \\ &= 2\boldsymbol{R} \cdot \delta \boldsymbol{v} + (\delta \boldsymbol{v})^2 \Delta t. \end{aligned} \tag{1.2}$$

where $\delta \boldsymbol{v} = d\boldsymbol{R}/dt$ is the velocity difference of the two particles. It is necessary that Δt be small enough to assure that the term $(\delta \boldsymbol{v})^2 \Delta t$ is negligible compared to the first term $2\boldsymbol{R} \cdot \delta \boldsymbol{v}$. We checked that this condition of small Δt is satisfied for the chosen value of $\Delta t = 20$ ms, by varying Δt.

1.4 Surface Waves

In the experiment reported here, particles diffuse on surface waves. The surface waves are governed by a dispersion relation. In general, the dispersion relation connecting the wave frequency ω and the wavelength $\lambda = 2\pi/k$ for surface waves is

$$\omega^2(k) = k[g + \sigma k^2/\rho]\tanh(kh) = kg[1 + \frac{1}{2}a^2k^2]\tanh(kh). \tag{1.3}$$

Here g is the local gravitational acceleration, σ is the surface tension coefficient, ρ is the fluid density, and $a = \sqrt{2\sigma/(\rho g)}$ is the capillary length of the fluid [13]. h is the mean depth of the fluid. We shall not be concerned with shallow water waves in this work. For a deep fluid ($h \to \infty$) the relation simplifies to

$$\omega^2(k) = k[g + \sigma k^2/\rho] = kg[1 + \frac{1}{2}a^2k^2] \tag{1.4}$$

In the experiment considered here, with wave frequency $\omega/(2\pi) = 130$ Hz and wavelength $\lambda = 2\pi/k = 2.6$ mm, the capillary length is $a = 3.1$ mm when determined from Eq. (1.4).

For long wavelengths, i.e. for small wave numbers, the gravitational force on the displaced fluid (displaced away from the flat surface, equilibrium) acts as the restoring force of the wave. In that case, the first term in (1.4) dominates. Such waves are called gravity waves. In the opposite case of short wavelengths, the effect of gravity can be neglected, and the restoring force due to the surface tension dominates, i.e. the second term of (1.4) dominates. For these waves, called capillary waves, the dispersion relation is

$$\omega^2(k) = \sigma k^3/\rho \ . \tag{1.5}$$

These are the waves present in our experiment: a short check of (1.4) shows that the second term is almost an order of magnitude larger than the first term. Notice that in both cases the dispersion relation is expressed as a power law.

Gravity waves are found e.g. at the surface of the oceans, excited by winds blowing over the surface. For water, capillary waves have wave lengths less than ≈ 4 mm [14].

Chapter 2

Relative Particle Motion

This part of the thesis is concerned with diffusion measurements on capillary waves and theoretical interpretations thereof. The following chapter is an introduction to Paper I and an extension of some of the work described therein. We discuss relative diffusion, and we report the results from relative diffusion in the Faraday experiment.

2.1 Diffusion

Tracers are assumed to follow the path of the fluid element they displace, thus visualizing the motion of the fluid. The tracer dynamics therefore yields important information about the underlying fluid motion.

The motion of a particle with respect to a fixed coordinate system in a turbulent flow — or simply in a "disordered" flow — is affected by eddies of all sizes in the flow. Think of the motion of a balloon in the atmosphere. This balloon will be shoveled back and forth by the local wind gusts, but it will also on a long time scale be carried along with the trade winds. Consequently, the position of the balloon is affected by eddies of the smallest and the largest length scale alike.

In contrast, diffusion based on the separation of two particles only depends on eddies smaller than or of the size of the separation. Relative diffusion measures the average rate of separation between pairs of particles. Consider an example of two balloons released into the atmosphere at a small separation. They will be individually affected by the wind gusts blowing in the vicinity of their respective position, changing their separation. But their relative position will not be affected by the trade winds passing by, because they will cause both balloons to change their positions roughly the same distance, simultaneously.

Richardson [1] was among the first to realize this important difference in the nature of the diffusion measurements. He found that the rate at which the particles move apart grows with the separation. The assumption is, as in the balloon-pair example above, that for a particular particle separation the eddies that contribute to the motion of the particles are those smaller than the separation. The growing separation rate can then easily be understood when considering that the further the particles are apart, the larger is the range of eddy sizes that contribute to their relative velocity. Thus, relative diffusion is an accelerating process until the particles are so far apart that they move independently [15].

Note that here the term "eddy" is not restricted to a simple rotary motion of a certain mass of liquid. Rather, in the spirit of Ref. [16], the term applies to patches of fluid on a certain scale (the "eddy size") that are correlated and have similar velocities. This is a rather weak definition, but it suffices for the current presentation.

Whether absolute diffusion (self-diffusion, diffusion of single particles) or relative diffusion (diffusion of pairs of particles) is measured, the underlying velocity field is the same, and it would be reasonable to expect that there be a close relationship between the results obtained in the two types of measurement. However, such a relationship has not been found in a theoretical form, except for special cases, e.g. for very short diffusion times [17]. Therefore, in addition to the absolute diffusion, the properties of relative diffusion are important.

In this chapter our measurements of relative diffusion in the Faraday experiment are reported. A discussion of the results in connection to the predictions of the theory of weak turbulence is presented in the next chapter. Absolute (or self-) diffusion is covered in a succeeding Chapter.

2.2 Relative Diffusion

The particle separation R is an important parameter for relative diffusion. However, there seems to be a lack of consensus on which quantity, derived from the separation, should be studied. The choice is often influenced by the selection of variables can actually be measured in a particular experiment. A few examples of diffusivity definitions will be given here.

Richardson [1] studied a cloud of particles and defined a neighbor concentration $q(R,t)$ so that $q(R,t)dR$ is the number of particles having neighbors at a

distance between R and $R + dR$, i.e. q is defined as

$$q(R,t) = \lim_{L_1,L_2\to\infty} \frac{\int_{-L_1}^{L_2} \nu(x,t)\nu(x+R,t)dx}{\int_{-L_1}^{L_2} \nu(x,t)dx} \tag{2.1}$$

where $\nu(x)$ is the particle concentration at position x. He defined a neighborhood diffusivity $F(R)$ from the diffusion equation as a measure of the rate of change of separation,

$$\frac{\partial q(R,t)}{\partial t} = \frac{\partial}{\partial R}\left[F(R)\frac{\partial q(R,t)}{\partial R}\right]. \tag{2.2}$$

In the case where the average change in separation $\langle R(t) - R(0)\rangle$ is much less than the initial separation $R(0)$ the neighborhood diffusivity for $R(0)$ can be approximated by

$$F(R(0)) = \frac{\langle[\boldsymbol{R}(t) - \boldsymbol{R}(0)]^2\rangle}{2t} \tag{2.3}$$

where the average is over all pairs that are released at the fixed distance $R(0)$ apart. Richardson found that the neighborhood diffusivity increases as $F(R(0)) \propto R(0)^{4/3}$ for atmospheric turbulence. This has been named the "Richardson 4/3 law".

The Kolmogorov theory (K41) of three-dimensional turbulence [18], which came after Richardson's 1926 paper, gave strong support to Richardson's 4/3 law. The K41 theory predicts that $\langle \delta v_{||}(R)^n\rangle \propto R^{\zeta_n}$ with $\zeta_n = n/3$ in the inertial range of three-dimensional locally isotropic and homogeneous turbulence. The K41-scaling fits well with Richardson's 4/3 law $F(R(0)) \propto R(0)\langle \delta v_{||}(R)\rangle \propto R(0)^{1+1/3}$. Note, however, that the system we consider is a (quasi-) two-dimensional system. Similar to the K41-scaling for three-dimensional turbulence, numerical and experimental evidence [19] suggests that $\langle dR^2/dt\rangle \propto R^2$ for two-dimensional turbulence, i.e. $\langle R^2\rangle \propto \exp(t/t^*)$ where t^* is some characteristic time scale.

Grossmann discusses the ambiguity in defining a diffusivity in Ref. [20]. He chooses to define the diffusivity as

$$K = \frac{1}{6}\frac{d\langle[R(t) - R(0)]^2\rangle}{dt} \tag{2.4}$$

with an average over pairs with fixed initial separation. Hinze [17] and Batchelor [15] agree on defining a relative diffusion, or relative dispersion, as $\langle R^2(t)\rangle$ and a relative diffusion coefficient as

$$\frac{1}{2}\frac{d\langle R^2(t)\rangle}{dt} \quad \text{(Hinze) or} \quad \frac{d\langle R^2(t)\rangle}{dt} \quad \text{(Batchelor).} \tag{2.5}$$

Morel and Larcheveque [21] study large-scale two-dimensional atmospheric turbulence using balloons distributed over the Southern Hemisphere at a constant level. They consider a relative diffusion rate like (2.5), but in addition they also consider the velocity variance $\langle (dR(t)/dt)^2 \rangle$. The balloons were released in groups, and their positions were measured by a satellite. The positions of the balloons were measured at two successive orbits of the satellite. Morel and Larcheveque find that $\langle \Delta(R^2)/\Delta t \rangle \propto R^2$ and $\langle R^2 \rangle \propto \exp[\, t/(1.35 \text{ days})]$, in accordance with the Kolmogorov-like result for two-dimensional turbulence, which was mentioned above. Hentschel and Procaccia [22] also consider a relative diffusion rate like (2.5), and the velocity variance $\langle (dR(t)/dt)^2 \rangle$.

Stommel [16] studies floats that were released in pairs in the ocean. The floats were followed over a large range of scales (length scales 10 cm to 1000 km and time scales 3 s to 3 days), and the velocity variance $\langle (\Delta R(t)/\Delta t)^2 \rangle$ was found with an ensemble average over pairs of equal initial separation. He defines a relative diffusivity as $\langle (\Delta R(t)/\Delta t)^2 \rangle \Delta t$ which he finds to be proportional to $R^{4/3}$.

Okubo [23] studies the spreading of dye in the upper ocean at time scales from a few hours to a month. He finds that the average distance of dye patches grows as $\langle R^2 \rangle \propto (\Delta t)^{2.3}$. This implies [24] that the relative diffusivity in the Hinze/Batchelor definition (2.5) is $d\langle R^2 \rangle/dt \propto (\Delta t)^{1.3} \propto R^{1.3(2/2.3)} = R^{1.1}$, which is far from the turbulence result R^2.

As a final example we mention that Ramshankar and Gollub [11] studied the spreading of dye on capillary waves in the Faraday experiment. They found the fractal dimension of the contours of constant dye concentration to be $d_f = 1.40 \pm 0.05$. Via a theory by Constantin and Procaccia [25] this result yields an exponent ζ^{abs} for $\langle |\delta v_{||}(R)| \rangle \propto R^{\zeta^{abs}}$ which is $\zeta^{abs} = 2d_f - 3 = -0.2 \pm 0.1$; see also Paper I.

It should be clear from these examples that an abundance of relevant definitions exist! However, on long time scales where $R(t)$ is likely to be much larger than $R(0)$, most of the definitions boil down to more or less the same quantity. The choice of expression for this quantity is not essential, as long as care is taken when comparing to other measurements or predictions. We chose to study the relative diffusion coefficient (sometimes also called the relative diffusivity) as given by the expression

$$\left\langle \frac{dR^2(t)}{dt} \right\rangle_{\tilde{R}} \tag{2.6}$$

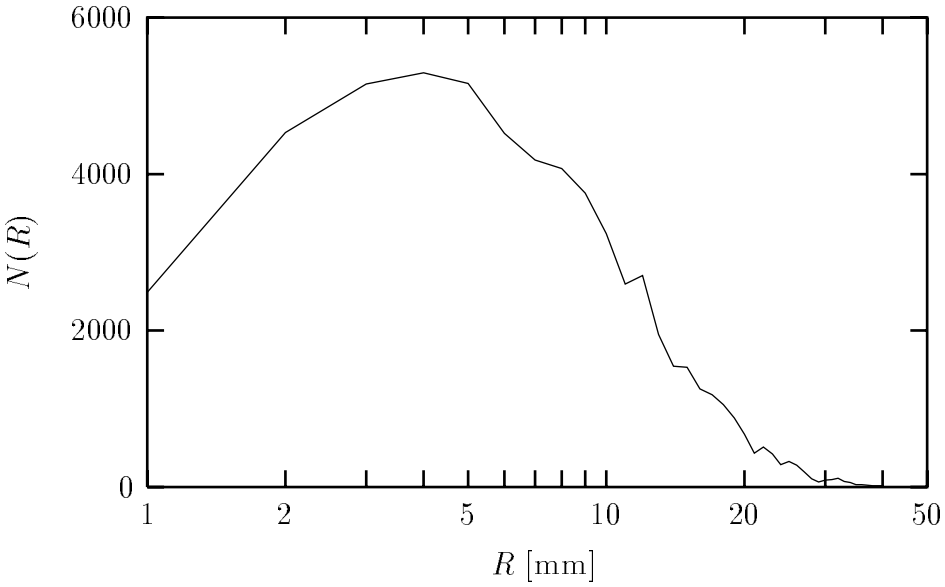

Figure 2.1: Relative diffusion. Sample size $N(R)$ of measurements at control parameter $\epsilon = 0.24$.

implemented by using the finite difference

$$\frac{\Delta(R^2)}{\Delta t} = \frac{\boldsymbol{R}^2(t+\Delta t) - \boldsymbol{R}^2(t)}{\Delta t} \tag{2.7}$$

as already discussed in Chapter 1.

We are interested in the behavior of $dR^2(t)/dt$ and its moments as a function of R. We therefore only need the relative particle tracks chopped up in steps with information about the separations $R(t)$ and $R(t+\Delta t)$ at two succeeding time steps. The average $\langle \cdot \rangle_{\tilde{R}}$ is over all such bits of tracks for which the separation at the first of the two time steps is $\tilde{R} - \eta < R(t) < \tilde{R} + \eta$. Note, though, that all particle pairs considered have an initial separation $R(0)$ less than some small length scale (here: 4 mm). A particle pair can thus contribute more than once to the average, namely once every time the separation is within $\tilde{R} \pm \eta$. Figure 2.1 shows the number $N(R)$ of track pieces with separation R. The number depends on the separation, only few pairs reached a separation larger than 30 mm.

2.3 Moments of the Relative Diffusivity

We analyzed the distribution function $P(dR^2/dt)$ of the diffusivity and the moments of the distribution. Some of the results are reported in Paper I. Below

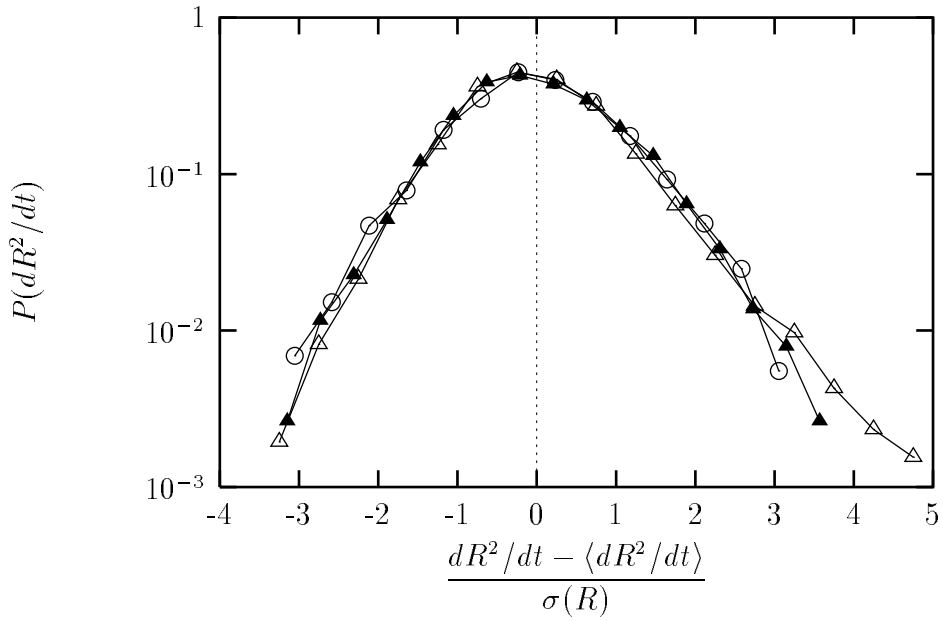

Figure 2.2: Relative diffusivity distribution $P(dR^2/dt)$ (semi-logarithmic scale) for $R = 3$ mm (open triangles), $R = 6$ mm (filled triangles), and $R = 14$ mm (circles); $\epsilon = 0.24$. The error bars are of the size of the symbols.

I summarize the main results of Paper I with regards to the Faraday experiment, and I introduce results that were not reported in Paper I. The rescaled distribution function $P(dR^2/dt)$ is also the rescaled distribution function for the longitudinal velocity difference $\delta v_{||}(R)$. This follows from the relation $dR^2/dt \simeq 2R\,\delta v_{||}(R)$ and from the fact that the averages are taken for fixed separation R. The relation between their moments follows easily, as we shall see.

The Figure 2.2 shows the distribution function $P(dR^2/dt)$ for separations $R = 3$, 6, and 14 mm, all at control parameter $\epsilon = 0.24$. The distributions are normalized, horizontally translated by their mean value $\langle dR^2/dt \rangle$, and rescaled by their standard deviation

$$\sigma(R) = \left\langle \left[\frac{dR^2}{dt} - \left\langle \frac{dR^2}{dt} \right\rangle \right]^2 \right\rangle^{1/2} . \tag{2.8}$$

We find that the distributions consistently have their maximum to the left of the mean. This is in contrast to fully developed turbulence in three dimensions, for which the maximum is to the right of the mean (the third moment is negative). The mean value in our experiment is an order of magnitude smaller than the standard deviation, a fact that unfortunately make the statistical errors significant. The distribution function $P(dR^2/dt)$ changes with R, from being Gaussian-like

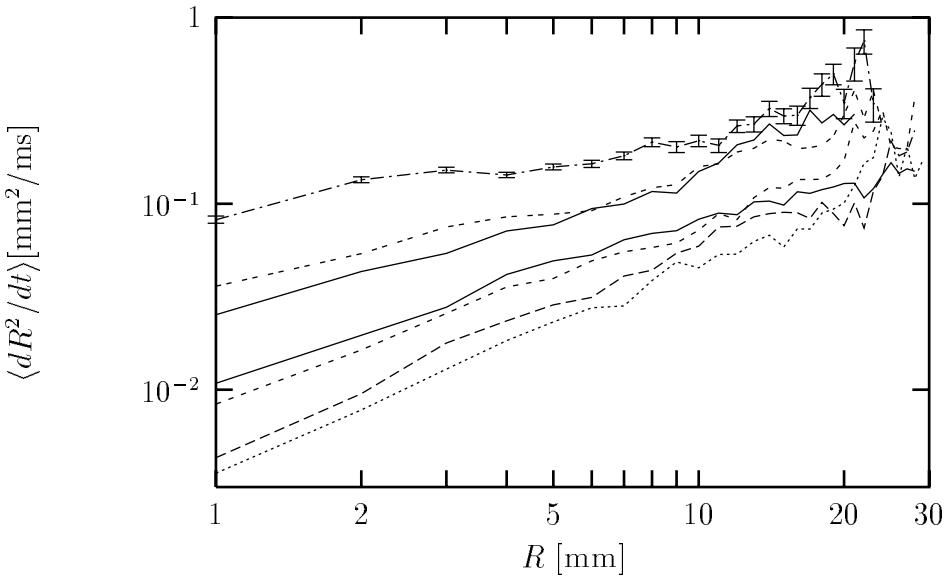

Figure 2.3: Relative diffusion. Mean value $\langle dR^2/dt \rangle$ versus R (double-logarithmic scale). From below, $\epsilon = 0.05$, 0.13, 0.24, 0.34, 0.65, 0.86, and 1.06.

(but skew) at large separations ($R = 14$ mm), to having significant tails at small separations ($R = 3$ mm), which also happens for three-dimensional turbulence [26]. These claims will be more evident below when the moments of $P(dR^2/dt)$ are considered.

The two first moments of $P(dR^2/dt)$ were discussed in Paper I, i.e. the mean value $\langle dR^2/dt \rangle$ and the variance $\sigma(R)^2 = \langle [R^2/dt - \langle R^2/dt \rangle]^2 \rangle$. In Figure 2.3, the mean value is shown as a function of R on a double-logarithmic scale for the seven values of ϵ ranging from 0.05 (lower line) to 1.06 (upper line). We find that the mean value increases with separation R. In other words, the rate at which the particles move apart increases with growing separation as Richardson predicted for atmospheric turbulence, although not at the same rate. As explained in Paper I, if we assume a power-law behavior $\langle dR^2/dt \rangle \propto R^\alpha$, we find that the exponent is $\alpha = 0.9 \pm 0.15$ (with a tendency to decrease with ϵ) for this spatio-temporal chaotic system. This is in contrast to the value $\alpha = 2$ expected for two-dimensional turbulent systems and in contrast to the atmospheric measurements by Morel and Larcheveque [21]. We also note that the exponent $\alpha = 0.9 \pm 0.15$ is in reasonable agreement with the exponent 1.1 that was found in the aforementioned dye-spreading measurements by Okubo [23]. However, the averaging process in Okubo's work is carried out for fixed time, not fixed separation as in our case.

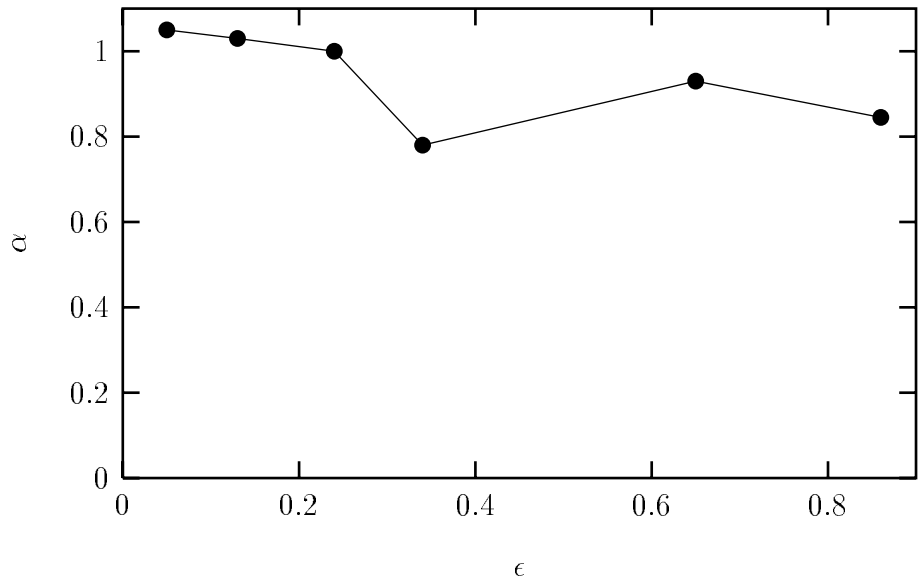

Figure 2.4: Relative diffusion. The exponent of $\langle dR^2/dt \rangle \propto R^\alpha$ versus the control parameter ϵ. No exponent is given for $\epsilon = 1.06$ because a slope cannot be defined for this value in Figure 2.3.

The measured values of the exponent α are shown in Fig. 2.4. For the largest control parameter $\epsilon = 1.06$ a slope cannot be defined from Fig. 2.3. The statistical errors of the mean $\langle dR^2/dt \rangle$ are estimated to be $\sigma(R)/\sqrt{N(R)}$, which are shown as error bars for $\epsilon = 1.06$ in Fig. 2.3, with similar error bars for the other ϵ values. For large values of R the size of the ensemble is small (see Fig. 2.1), and the data points have large error bars.

We also measured the absolute first moment $\langle |dR^2/dt| \rangle = 2R\langle |\delta v_{||} R| \rangle \propto R^{\zeta^{abs}+1}$ and found that ζ^{abs} is very close to zero and slightly positive. We see that this is close to the result $\zeta^{abs} = -0.2 \pm 0.1$ predicted by the theory of Constantin and Procaccia when using the dye spreading results of Ramshankar and Gollub; see the previous pages.

The second central moment of $P(dR^2/dt)$ is represented by the standard deviation $\sigma(R)$; see Fig. 2.5. For each value of ϵ the data are fitted rather well by a straight line, $\sigma(R) \propto R^{\alpha_2/2}$. For $\epsilon < 0.4$ we find $\alpha_2 = 2.26 \pm 0.06$, and for larger values of ϵ, α_2 approaches 2; see Fig. 2.6.

The values of the first and second moment exponents α and α_2 allow us to compare our results to the oceanographic measurements by Stommel. As noted in Paper I the relation to Stommel's result is $\alpha_2 - \alpha = 4/3$, which is in good

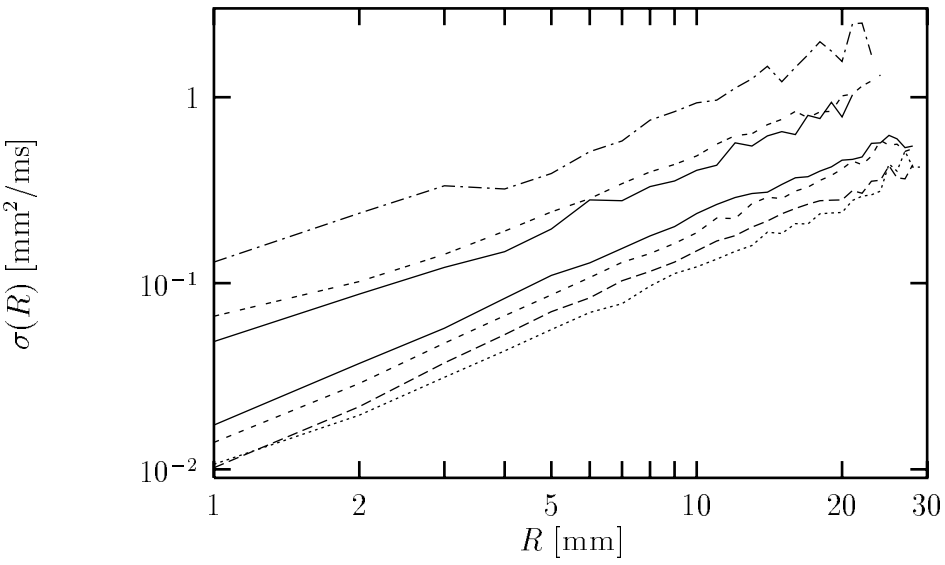

Figure 2.5: Relative diffusion. Standard deviation $\sigma(R)$ versus R (double-logarithmic scale). From below, $\epsilon = 0.05$, 0.13, 0.24, 0.34, 0.65, 0.86, and 1.06.

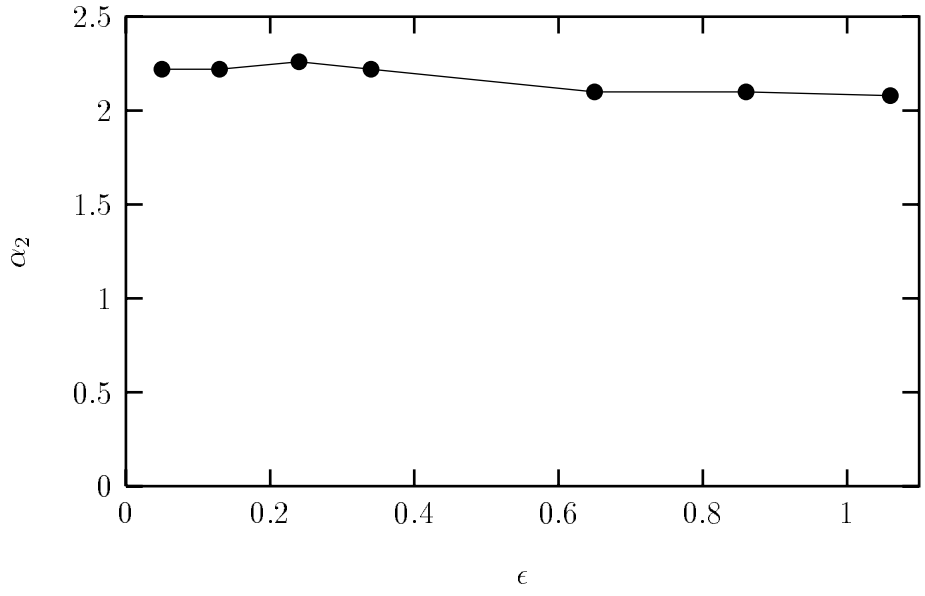

Figure 2.6: Relative diffusion. The exponent of $\sigma^2(R) \propto R^{\alpha_2}$ versus the control parameter ϵ.

agreement with our measurements; $\alpha_2 - \alpha = 1.25 \pm 0.1$.

The higher order moments of the relative diffusivity distribution

$$\mu_n(R) = \left\langle \left[\frac{dR^2}{dt} - \left\langle \frac{dR^2}{dt} \right\rangle \right]^n \right\rangle \tag{2.9}$$

were also examined, although not all the results were reported in Paper I. Here $\mu_2(R) = \sigma^2(R)$ is the variance. We also examined the third absolute central moment

$$\nu_3(R) = \left\langle \left| \frac{dR^2}{dt} - \left\langle \frac{dR^2}{dt} \right\rangle \right|^3 \right\rangle \tag{2.10}$$

which is plotted in Fig. 2.7 along with $\mu_n(R)$ for $n = 3$, 4, 5, 6, 7, and 8. Again assuming power-law behaviors $\mu_n(R) \propto R^{\alpha_n}$ and $\nu_3(R) \propto R^{\alpha_3^{abs}}$ we can find exponents for some of the moments, as we did in Paper I. We find $\alpha_3^{abs} = 3.37 \pm 0.06$, $\alpha_4 = 4.37 \pm 0.06$, and $\alpha_6 = 6.2 \pm 0.1$ for $\epsilon = 0.24$; see also Table 2.1. With the data we have available it is not possible to determine the exponents for moments higher than $\mu_6(R)$ by the usual moments-versus-R plots, and even the exponents that we did determine were difficult to obtain, due to the fluctuations at large separations. Finding higher order moments involves measuring the rare events that make up the tails of the probability distribution function, the higher order moments are therefore very sensitive to statistical errors.

A by-now standard "trick" to obtain more accurate values of the exponents of such moments is the method of extended self-similarity (ESS) [27, 28]. The idea is the following. In three-dimensional turbulent flow at low Reynolds number the spatial range in which one can determine the exponent ζ_n^{3D} of the velocity moment

$$\left\langle \left[\delta v_{||}^{3D} - \left\langle \delta v_{||}^{3D} \right\rangle \right]^n \right\rangle \propto R^{\zeta_n^{3D}} \tag{2.11}$$

is small. The dissipation scale in the small-R end and the integral range in the large-R end set the limits. In order to determine the exponents with more accuracy one plots the moments against a reference moment, usually the third moment. The third moment grows linearily with R above the dissipation scale, by a rigid theoretical prediction (K41) [18, 29]. Plotting the moments versus the reference moment has the effect of removing some of the arbitrary structure that shows up as e.g. humps in a particular set of measurements. This then yields lines that are more straight in a doubly logarithmic plot over a longer range and from these lines the ratios of the exponents to the reference exponent are found

$$\left\langle \left[\delta v_{||}^{3D} - \left\langle \delta v_{||}^{3D} \right\rangle \right]^n \right\rangle \propto R^{\zeta_n^{3D}} \propto \left\langle \left[\delta v_{||}^{3D} - \left\langle \delta v_{||}^{3D} \right\rangle \right]^3 \right\rangle^{\zeta_n^{3D}/\zeta_3^{3D}} \tag{2.12}$$

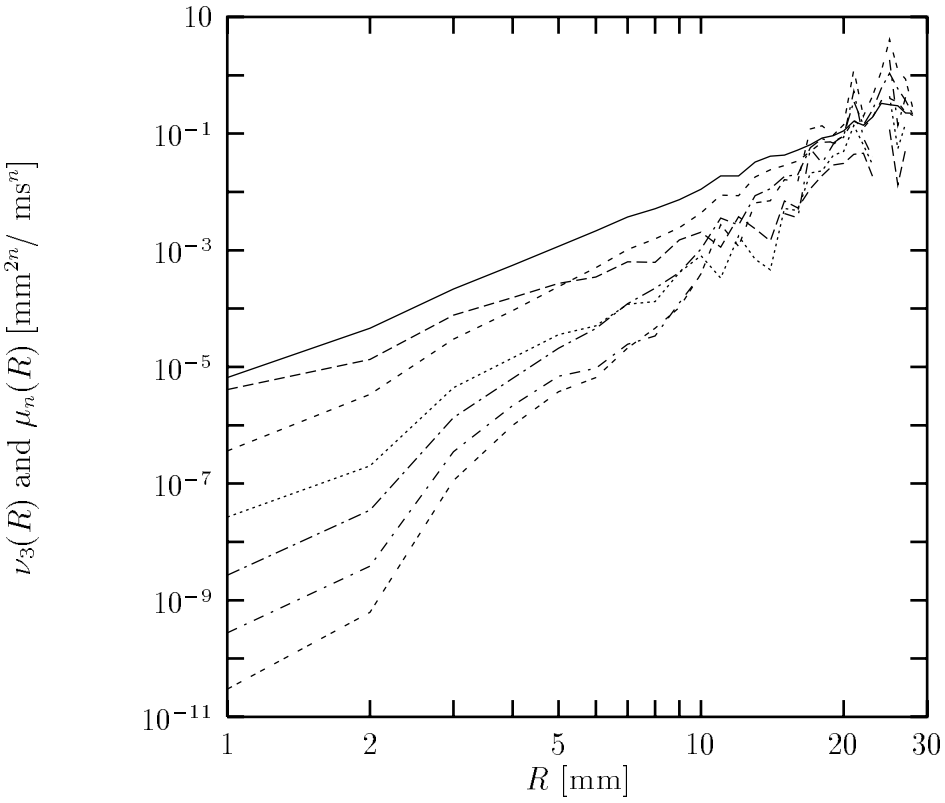

Figure 2.7: Relative diffusion. The higher order central moments. From the top: $\nu_3(R)$, and $\mu_n(R)$ for $n = 3$, 4, 5, 6, 7, 8, all at $\epsilon = 0.24$.

where $\zeta_3^{3D} = 1$. Plotting the moments versus the reference moment also removes the dependence of the measured exponents on the Reynolds number of the flow. Often the third *absolute* moment is substituted for the third moment because absolute moments are less affected by noise than their non-absolute counterparts, and because the third moment and the third absolute moment are very close to being linearly proportional in most measurements.

The method of ESS does not immediately apply to our system. We study a spatio-temporally chaotic system, not a fully developed turbulent system, and furthermore our system is not three-dimensional but (quasi-) two-dimensional. Still, we may hope to gain insight by employing the method of ESS to our data.

First, we would like to perhaps eliminate the humps that are clearly present in our data (see the small humps in Fig. 2.7 around $R = 11$ mm and at larger separations). This would make a more precise determination of ratios of exponents possible. We need to determine one moment as a reference moment by other

means, though, because no rigid theoretical predictions exist for any of the moments in our system[1]. Since the diffusivity is the primary quantity we measured we choose to carry through the analysis for the moments of diffusivity, not for the moments of velocity difference. We choose to use the third absolute moment $\nu_3(R)$ as a reference moment, with $\alpha_3^{abs} = 3.37 \pm 0.06$, because this reference moment turned out to give the best results. The results of plotting the moments $\mu_n(R)$ against $\nu_3(R)$ are described below.

Second, we would like to be able to think of our control parameter ϵ as a parameter similar to a Reynolds number, because varying ϵ determines how much the moving defects dominate the system, i.e. how "random" the system is. For ϵ to be useful as such a parameter, the plots of moments-versus-moments must conceal the effect of ϵ. In Figure 2.8 we plot $\sigma^2(R) = \mu_2(R)$ versus $\nu_3(R)$ for all available values of ϵ. We see that indeed the effect of varying ϵ does not appear in the plot, all points fall on the same straight line, except a few points of the $\epsilon = 0.65$ measurements. The plot therefore supports the idea of ϵ as a sort of 'Reynolds number' for the system.

In Figure 2.9 we plot the moments $\mu_n(R)$, for n even, as functions of the third absolute moment $\nu_3(R)$ in a double-logarithmic plot. We have

$$\mu_n(R) \propto R^{\alpha_n} \propto \nu_3(R)^{\alpha_n/\alpha_3^{abs}} \ . \tag{2.13}$$

We see that for all the moments shown the data can be fitted to power laws with exponents α_n/α_3^{abs}. We also fitted $\mu_n(R)$ versus $\nu_3(R)$ to power laws for $n = 12$ to 18, although those plots are not shown here. The exponents α_n/α_3^{abs} found by this ESS-like method are listed in Table 2.1. It is clear from comparing the usual $\mu_n(R)$-versus-R plot in Fig. 2.7 to the ESS-like plot in Fig. 2.9 that the latter removes some of the arbitrary structure in the data and makes it possible to determine power laws with more accuracy and for even higher moments than the usual plot does.

The moments of the relative diffusivity yield via the relation $dR^2/dt = 2R\,\delta v_{||}(R)$ the corresponding moments of the longitudinal velocity difference

$$\left\langle \left[\delta v_{||} - \left\langle \delta v_{||} \right\rangle \right]^n \right\rangle = 2^{-n} R^{-n} \mu_n(R) \propto R^{\zeta_n} \tag{2.14}$$

where $\zeta_n = \alpha_n - n$, and similar for $\nu_3(R)$.

For fully developed turbulence in three dimensions, K41 predicts that the exponents of the velocity moments are linearly proportional to n, $\zeta_n^{3D} = n/3$. By

[1] For strongly turbulent two-dimensional systems experimental and numerical evidence suggests that $\zeta_2 = 2$ ($\alpha_2 = 4$) [19], but our system is not strongly turbulent.

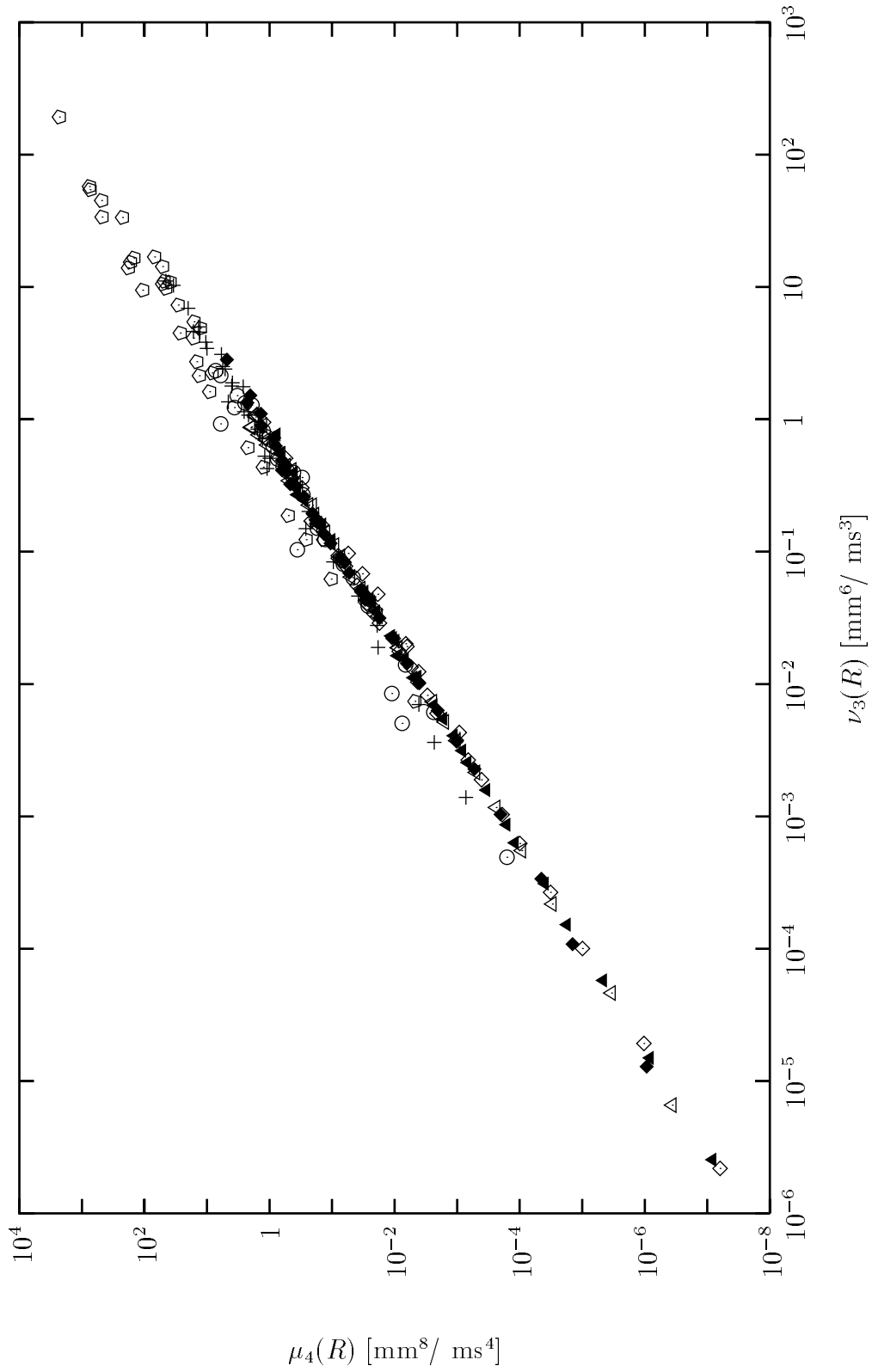

Figure 2.8: Relative diffusion. Double-logarithmic plot of the moment $\mu_4(R)$ versus the absolute moment $\nu_3(R)$ for all available values of ϵ. Filled triangles: $\epsilon = 0.05$; open diamonds: $\epsilon = 0.13$; open triangles: $\epsilon = 0.24$; filled diamonds: $\epsilon = 0.34$; circles: $\epsilon = 0.65$; crosses: $\epsilon = 0.86$; pentagons: $\epsilon = 1.06$.

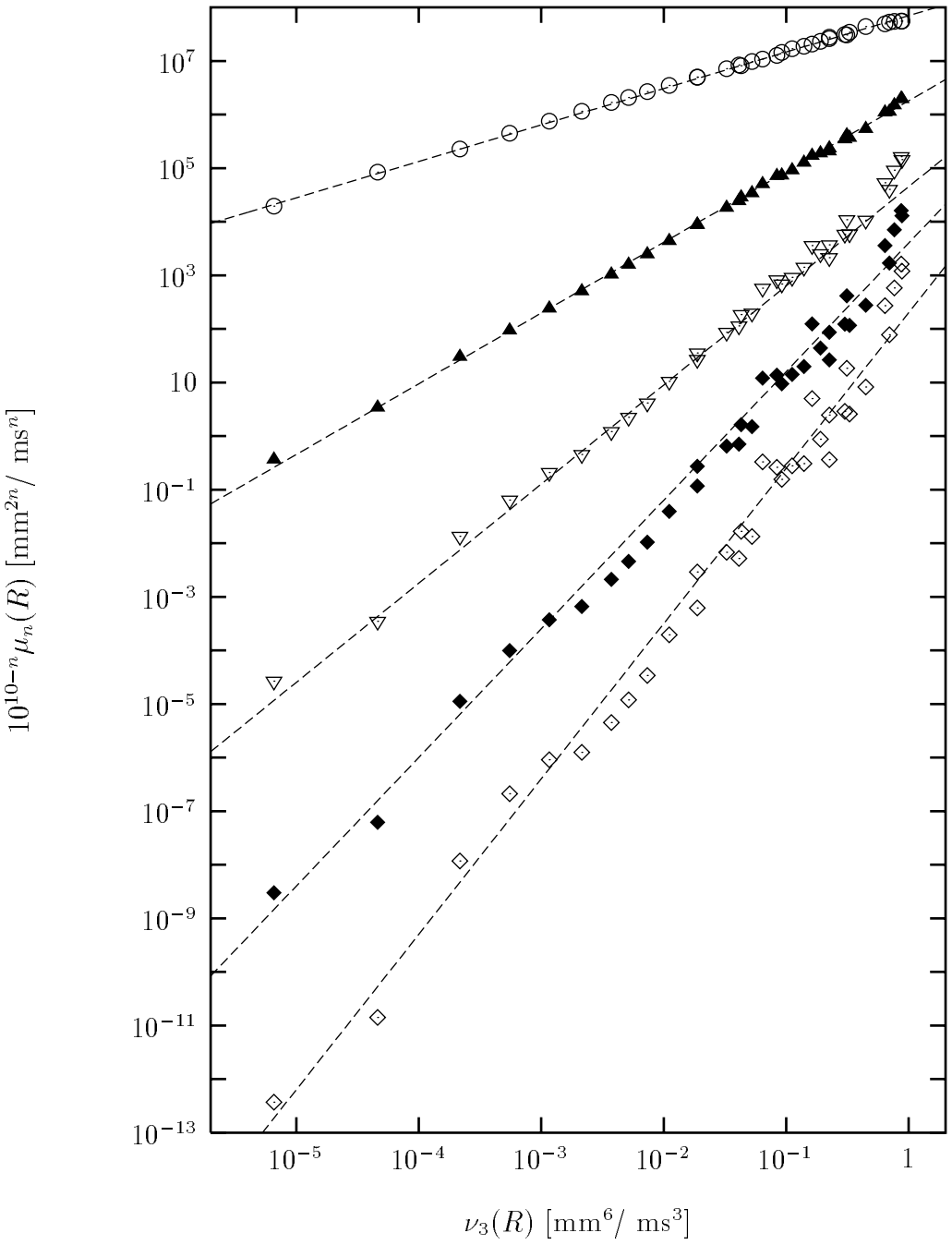

Figure 2.9: Relative diffusion. Double-logarithmic plot of the moments $\mu_2(R) = \sigma^2(R)$ (circles), $\mu_4(R)$ (filled triangles), $\mu_6(R)$ (open triangles), $\mu_8(R)$ (filled diamonds), and $\mu_{10}(R)$ (open diamonds), plotted versus $\nu_3(R)$. The graphs are shifted by 10^{10-n} in order to enhance visibility. The broken lines have slopes (from above) 0.68, 1.32, 1.85, 2.4, and 2.9 and the control parameter is $\epsilon = 0.24$.

n	α_n	$\zeta_n = \alpha_n - n$	α_n/α_3^{abs}
2	2.26 ± 0.06	0.26 ± 0.06	0.68 ± 0.01
3	2.8 ± 0.2	-0.2 ± 0.2	0.9 ± 0.1
3 (abs)	3.37 ± 0.06	0.37 ± 0.06	1
4	4.37 ± 0.06	0.37 ± 0.06	1.32 ± 0.02
6	6.2 ± 0.1	0.2 ± 0.1	1.85 ± 0.05
8	—	—	2.40 ± 0.05
10	—	—	2.9 ± 0.1
12	—	—	3.5 ± 0.1
14	—	—	4.0 ± 0.2
16	—	—	4.6 ± 0.3
18	—	—	4.9 ± 0.5

Table 2.1: Relative diffusion. Summary of the exponents found for the various moments of diffusivity at $\epsilon = 0.24$. The ratio α_n/α_3^{abs} is measured from an ESS-like plot similar to Fig. 2.9. A dash means 'not measured'.

taking intermittency effects into account ζ_n^{3D} deviates from the $= n/3$ behavior. With a parabola being the lowest correction to a linear dependence it is predicted that ζ_n^{3D} should lie on a parabola that passes through origo and $(3, 1)$. Experimentally it is found that for small values of n this is a reasonable fit, but since ζ_n^{3D} does not have a maximum the exponents must deviate from the parabola for high values of n. In Rayleigh-Bernard flow, where $\zeta_3^{RB} \neq 1$, it has been found [30] that the ratios $\zeta_n^{RB}/\zeta_3^{RB}$ follow the same parabola as for fully developed turbulence. However, these experiments are all rather different from ours, and a priori we do not expect our exponents to follow the same curve.

In Figure 2.10 we plot the diffusivity exponents α_n/α_3^{abs} as functions of the moment order n. We see that α_n is not linearly proportional to n, because if it were, we would have $\alpha_n/\alpha_3^{abs} = n/3$. This is clearly not the case in Fig. 2.10. With the parabola fit of fully developed turbulence in mind it is tempting to aim at a parabola fit for our $\alpha_n = \zeta_n + n$. We find that the exponents α_n/α_3^{abs} indeed fit reasonably well to a parabola. This means that $\zeta_n/\zeta_3^{abs} = (\alpha_n - n)/(\alpha_3^{abs} - 3)$ also fits to a parabola, but a very different parabola than for fully developed turbulence and Rayleigh-Bernard flow.

Finally, we study the R-dependence of the ratios $\nu_3(R)/\sigma(R)^3$ and $\mu_n(R)/\sigma(R)^n$ for $n = 3$, 4, and 6; see Fig. 2.11. These ratios are often used to characterize a distribution, in particular the skewness $S = \mu_3(R)/\sigma(R)^3$, the kurtosis $K = \mu_4(R)/\sigma(R)^4 - 3$, and the hyper-flatness $F = \mu_6(R)/\sigma(R)^6$. For a Gaussian dis-

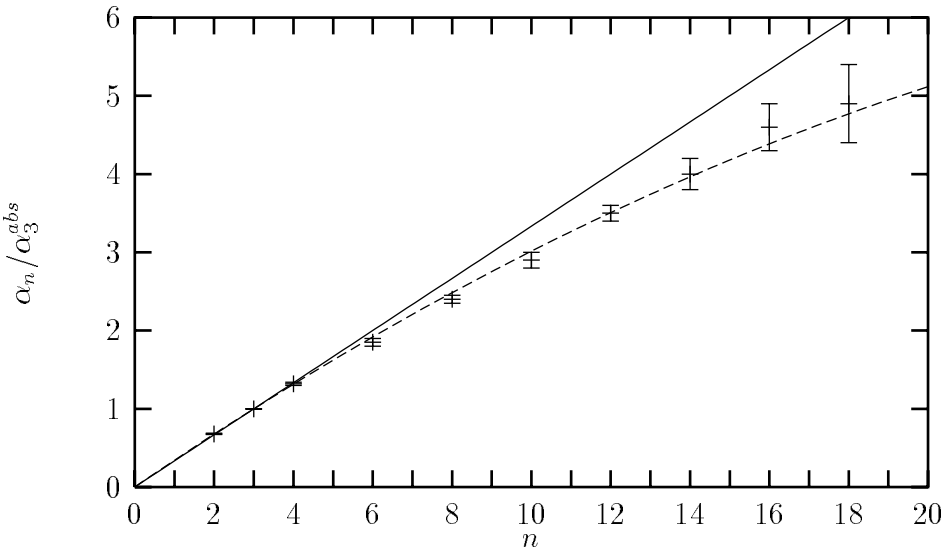

Figure 2.10: Plot of the values of α_n/α_3^{abs} from Table 2.1. The unbroken line is the linear line $n/3$, the broken line is a parabola fit that passes through origo and $(3, 1)$.

tribution S and K are both zero. The Gaussian values $\nu_3(R)/\sigma(R)^3 = 2\sqrt{2/\pi} \simeq 1.60$, $\mu_4(R)/\sigma(R)^4 = 3$, and $\mu_6(R)/\sigma(R)^6 = 15$ are shown as dotted lines in Fig. 2.11. For all values of ϵ we find that the ratios $\mu_n(R)/\sigma(R)^n$ and $\nu_3(R)/\sigma(R)^3$ decrease with R towards the Gaussian values. We attribute this decay to the presence of side humps on the distribution $P(dR^2/dt)$; see Fig. 2.2. These humps are positioned furthest out (in terms of standard deviations) at small distances R. The kurtosis K measures how 'peaked' the distribution is, compared to the Gaussian distribution. The positive K shows that the distribution in Fig. 2.2 is more peaked than a Gaussian distribution.

We see that due to the relation (2.14) the ratios in Fig. 2.11 are also the similar ratios for the velocity differences. In fully-developed three-dimensional turbulence the skewness of the velocity distribution is negative. We notice that the skewness of the velocity distribution in the Faraday experiment is positive. This is connected to the fact that the distribution function in Fig. 2.2 has its maximum to the left of the mean value.

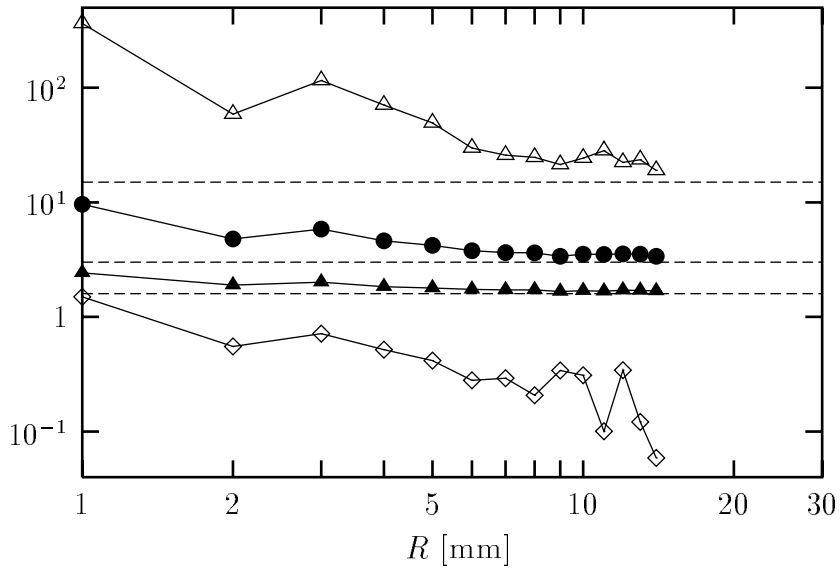

Figure 2.11: Relative diffusion. Moment ratios $\nu_3(R)/\sigma(R)^3$ (diamonds) and $\mu_n(R)/\sigma(R)^n$ for $n = 3$ (filled triangles), 4 (circles), and 6 (open triangles) at $\epsilon = 0.24$. The data is cut off at $R > 15$ at which the skewness $= \mu_3(R)/\sigma(R)^3$ becomes smaller than $3\sqrt{15/N(R)}$, which three times the standard deviation of the skewness in a Gaussian distribution. The dotted lines indicating the Gaussian values seem to be approached at large distances.

Chapter 3

Theory of Weak Turbulence

This chapter is devoted to a short review of the theory of *weak turbulence* (TWT), also called *weak wave turbulence*, and to a comparison between the predictions arising from TWT and the measurements that we performed on floating particles in the Faraday experiment. As will become clear towards the end of this chapter, the relevant quantity to study is the second moment $\langle|\delta\boldsymbol{v}(R)|^2\rangle$ of the velocity differences. When introducing the most relevant points of TWT, I shall be fairly general, making few assumptions on the type of waves involved. Eventually, though, I will concentrate on deep-water capillary waves.

The main reference used in this chapter is the book by Zakharov, L'vov, and Falkovich [31]. There are a number of confusing misprints in the first edition of Ref. [31], and I will point out the misprints when relevant. However, I cannot give any guarantee that I did not introduce other misprints!

This chapter is organized as follows. First, the Hamiltonian of the system and its expansion in small nonlinearities are introduced. This involves introducing rather general (from a capillary-waves point of view) canonical variables and a wave occupation number. Then follows a short discussion on the derivation of the kinetic equations for the wave occupation number, and the solutions of the kinetic equations. This is a short review of Ref. [31], although I keep more terms in my presentation than is done in Ref. [31]. At this point, the Hamiltonian formalism is re-formulated in terms of physical quantities of surface waves. The interaction coefficients that appear in the Hamiltonian are given for capillary and gravity waves. Then follows a derivation of the wave-number dependence of the wave density $n(k)$ for capillary waves, from which I obtain a prediction on the second moment $\langle|\delta\boldsymbol{v}(R)|^2\rangle$. Finally, the prediction is compared to our data.

3.1 Hamiltonian Formalism

Fully developed turbulence is also called "strong turbulence" to distinguish it from from "weak turbulence". The TWT describes turbulent systems that have a linear approximation of small-amplitude background waves and in which the level of nonlinearity is a small parameter. The coupling of interacting modes is expressed through the dispersion relation $\omega(\boldsymbol{k})$, which is assumed to be the only characteristic that distinguishes waves in different media, whether it be ferromagnets or fluids. In contrast to weak turbulence there exists no small parameter in fully developed turbulence around which to expand, and it is impossible to obtain a consistent linearization.

For the Hamiltonian formulation the (small) wave amplitudes may be represented by a set of (small) complex variables $a(\boldsymbol{r},t)$ and $a^*(\boldsymbol{r},t)$, which are related to the canonical variables of coordinate and momentum. The complex variables can be chosen such that when expanding the Hamiltonian $\mathcal{H}$ in a power series of their Fourier transforms [denoted $a(\boldsymbol{k})$ and $a^*(\boldsymbol{k})$]

$$\mathcal{H} = \mathcal{H}_2 + \mathcal{H}_{int}\,, \quad \mathcal{H}_{int} = \mathcal{H}_3 + \mathcal{H}_4 + \mathcal{H}_5 + \dots\,, \tag{3.1}$$

the dispersion relation is the coefficient of the second order term

$$\mathcal{H}_2 = \int \omega(\boldsymbol{k})\, a(\boldsymbol{k})\, a^*(\boldsymbol{k})\, d\boldsymbol{k} \tag{3.2}$$

and all information about the wave interactions is contained in the higher order terms $\mathcal{H}_{int}$. The third order term is given by the expression

$$\begin{aligned}\mathcal{H}_3 \;=\; & \frac{1}{2}\int [V(\boldsymbol{k}_1;\boldsymbol{k}_2,\boldsymbol{k}_3)\, a^*(\boldsymbol{k}_1)\, a(\boldsymbol{k}_2)\, a(\boldsymbol{k}_3) + \text{c.c.}] \\ & \qquad \times \delta(\boldsymbol{k}_1 - \boldsymbol{k}_2 - \boldsymbol{k}_3)\, d\boldsymbol{k}_1\, d\boldsymbol{k}_2\, d\boldsymbol{k}_3 \\ & + \frac{1}{6}\int [U(\boldsymbol{k}_1,\boldsymbol{k}_2,\boldsymbol{k}_3)\, a^*(\boldsymbol{k}_1)\, a^*(\boldsymbol{k}_2)\, a^*(\boldsymbol{k}_3) + \text{c.c.}] \\ & \qquad \times \delta(\boldsymbol{k}_1 + \boldsymbol{k}_2 + \boldsymbol{k}_3)\, d\boldsymbol{k}_1\, d\boldsymbol{k}_2\, d\boldsymbol{k}_3 \end{aligned} \tag{3.3}$$

(note the missing complex conjugation in the first term of Ref. [31, Eq. (1.1.24a)]). The interaction coefficients are symmetric with respect to interchange of arguments separated with a comma, e.g. $V(\boldsymbol{k}_1;\boldsymbol{k}_2,\boldsymbol{k}_3) = V(\boldsymbol{k}_1;\boldsymbol{k}_3,\boldsymbol{k}_2)$. The fourth order term is given by

$$\begin{aligned}\mathcal{H}_4 &= \frac{1}{4}\int W(\boldsymbol{k}_1,\boldsymbol{k}_2;\boldsymbol{k}_3,\boldsymbol{k}_4)\, a^*(\boldsymbol{k}_1)\, a^*(\boldsymbol{k}_2)\, a(\boldsymbol{k}_3)\, a(\boldsymbol{k}_4) \\ &\qquad \times \delta(\boldsymbol{k}_1+\boldsymbol{k}_2-\boldsymbol{k}_3-\boldsymbol{k}_4)\, d\boldsymbol{k}_1\, d\boldsymbol{k}_2\, d\boldsymbol{k}_3\, d\boldsymbol{k}_4 \\ &\quad + \int [G(\boldsymbol{k}_1;\boldsymbol{k}_2,\boldsymbol{k}_3,\boldsymbol{k}_4)\, a(\boldsymbol{k}_1)\, a^*(\boldsymbol{k}_2)\, a^*(\boldsymbol{k}_3)\, a^*(\boldsymbol{k}_4) + \text{c.c.}] \\ &\qquad \times \delta(\boldsymbol{k}_1-\boldsymbol{k}_2-\boldsymbol{k}_3-\boldsymbol{k}_4)\, d\boldsymbol{k}_1\, d\boldsymbol{k}_2\, d\boldsymbol{k}_3\, d\boldsymbol{k}_4 \\ &\quad + \int [R^*(\boldsymbol{k}_1,\boldsymbol{k}_2,\boldsymbol{k}_3,\boldsymbol{k}_4)\, a(\boldsymbol{k}_1)\, a(\boldsymbol{k}_2)\, a(\boldsymbol{k}_3)\, a(\boldsymbol{k}_4) + \text{c.c.}] \\ &\qquad \times \delta(\boldsymbol{k}_1+\boldsymbol{k}_2+\boldsymbol{k}_3+\boldsymbol{k}_4)\, d\boldsymbol{k}_1\, d\boldsymbol{k}_2\, d\boldsymbol{k}_3\, d\boldsymbol{k}_4\,. \end{aligned} \tag{3.4}$$

The third order term describes three-wave processes. The decomposing of one wave into two and the merging of two waves into one is described by the V-term, and the U-term describes the mutual creation (from vacuum) or annihilation of three waves. The fourth order term likewise describes the possible four-wave processes.

In general, the first term in the expansion of the interaction $\mathcal{H}_{int}$ will dominate the dynamics and all higher order terms can safely be ignored. However, if the three-waves processes do not allow for the decay process

$$\omega(\boldsymbol{k}_1+\boldsymbol{k}_2) = \omega(\boldsymbol{k}_1)+\omega(\boldsymbol{k}_2) \tag{3.5}$$

then the term $\mathcal{H}_4$ is large compared to $\mathcal{H}_3$ and must be retained. Four-wave processes are (almost [31, Chap. 1]) always permitted and thus an expansion up to at most the fourth order will (almost) always be sufficient. Dispersion relations that satisfy condition (3.5) are said to be of the decay type. The condition expresses momentum conservation $\boldsymbol{k}_1+\boldsymbol{k}_2=\boldsymbol{k}_3$ and energy conservation $\omega(\boldsymbol{k}_1)+\omega(\boldsymbol{k}_2)=\omega(\boldsymbol{k}_3)$ in (one wave)$\leftrightarrow$(two waves) processes. Energy-momentum conservation in processes of mutual annihilation and creation of three waves is expressed through the condition

$$\omega(\boldsymbol{k}_1)+\omega(\boldsymbol{k}_2)+\omega(-\boldsymbol{k}_1-\boldsymbol{k}_2)=0 \tag{3.6}$$

and it requires that negative-energy waves are permitted.

For isotropic media with a power-law dispersion-relation $\omega \propto k^\alpha$ the condition (3.5) has solutions for $\alpha > 1$. Thus capillary waves are of the decay type and gravity waves are of the nondecay type.

For nondecay dispersion relations the third order term $\mathcal{H}_3$ is unimportant, and it is convenient to perform a canonical transformation of the variables a and

a^* that eliminates the third order $\mathcal{H}_3$ and brings the fourth order on the form

$$\mathcal{H}_4 = \frac{1}{4}\int T(\boldsymbol{k}_1,\boldsymbol{k}_2;\boldsymbol{k}_3,\boldsymbol{k}_4)\, a^*(\boldsymbol{k}_1)\, a^*(\boldsymbol{k}_2)\, a(\boldsymbol{k}_3)\, a(\boldsymbol{k}_4) \times \delta(\boldsymbol{k}_1+\boldsymbol{k}_2-\boldsymbol{k}_3-\boldsymbol{k}_4)\, d\boldsymbol{k}_1\, d\boldsymbol{k}_2\, d\boldsymbol{k}_3\, d\boldsymbol{k}_4\,. \tag{3.7}$$

Here it has been assumed that only (two waves)$\leftrightarrow$(two waves) processes are allowed by the energy-momentum conservation, and terms corresponding to all other four-wave processes have been eliminated.

3.2 Kinetic Equations

Below, I introduce the wave occupation number $n(\boldsymbol{k},t)$ and show how the kinetic equations for the wave occupation number are derived. The kinetic equations for three-wave and for four-wave processes are the most important equations in TWT.

The canonical equation of motion in terms of the complex wave amplitudes is

$$i\frac{\partial a(\boldsymbol{k},t)}{\partial t} = \frac{\delta\mathcal{H}}{\delta a^*(\boldsymbol{k},t)}\,. \tag{3.8}$$

For small nonlinearities (i.e. for small wave amplitudes) the expansion of $\mathcal{H}$ is dominated by the first term $\mathcal{H}_2$ ($\gg \mathcal{H}_{int}$), which is the term describing the linear theory. Thus the linear-theory (the "free-field") canonical equation of motion yields

$$i\frac{\partial a(\boldsymbol{k},t)}{\partial t} = \frac{\delta\mathcal{H}_2}{\delta a^*(\boldsymbol{k},t)} = \omega(\boldsymbol{k})a(\boldsymbol{k},t) \tag{3.9}$$

which shows us that, for the case of free fields, the time evolution of the field $a(\boldsymbol{k},t) = |a(\boldsymbol{k},t)|\exp(-i\,\varphi(\boldsymbol{k},t))$ solely changes the phase of the field, leaving the amplitude constant in time,

$$a(\boldsymbol{k},t) = |a(\boldsymbol{k})|\exp(-i\,\omega(\boldsymbol{k})\,t)\,. \tag{3.10}$$

When weak nonlinearities are included in the description, an additional — slower — dynamics of both the amplitude and the phase of the fields is introduced. The fast part of the phase dynamics, which hardly affects the dynamics of the amplitudes, is assumed to be close to random. It can be removed by ensemble averaging, leaving only the slower dynamics stemming from the nonlinearities.

For a free field, the ensemble averaging thus removes any dynamics. The first two non-vanishing free-field correlators are

$$\begin{aligned}\langle a(\boldsymbol{k}_1,t)a^*(\boldsymbol{k}_2,t)\rangle &= \langle |a(\boldsymbol{k}_1)|\,|a(\boldsymbol{k}_2)|\exp(-i\{\omega(\boldsymbol{k}_1)-\omega(\boldsymbol{k}_2)\}\,t)\rangle \\ &= n(\boldsymbol{k}_1)\,\delta(\boldsymbol{k}_1-\boldsymbol{k}_2) \qquad (3.11)\end{aligned}$$

which defines the *wave occupation number* $n(\boldsymbol{k})$ for the free fields, and

$$\begin{aligned}&\langle a^*(\boldsymbol{k}_1,t)\,a^*(\boldsymbol{k}_2,t)\,a(\boldsymbol{k}_3,t)\,a(\boldsymbol{k}_4,t)\rangle \\ &\quad = n(\boldsymbol{k}_1)\,n(\boldsymbol{k}_2)\,[\delta(\boldsymbol{k}_1-\boldsymbol{k}_3)\delta(\boldsymbol{k}_2-\boldsymbol{k}_4)+\delta(\boldsymbol{k}_1-\boldsymbol{k}_4)\delta(\boldsymbol{k}_2-\boldsymbol{k}_3)]\ . \qquad (3.12)\end{aligned}$$

The free-field wave occupation number $n(\boldsymbol{k})$ has no time dependence. The wave occupation number for weak nonlinearities is defined equivalently, but it will in general have a (slow) time dependence and the correlators (e.g. $\langle a(\boldsymbol{k}_1,t)a(\boldsymbol{k}_2,t)\rangle$ and $\langle a(\boldsymbol{k}_1,t)a(\boldsymbol{k}_2,t)a^*(\boldsymbol{k}_3,t)\rangle$) do not necessarily vanish. The aim is to obtain an equation of motion for $n(\boldsymbol{k},t)$, and then afterwards to solve it for $n(\boldsymbol{k},t)$.

3.2.1 Derivation of Three-Wave Kinetic Equation

In decay systems the term $\mathcal{H}_3$ dominates the interaction Hamiltonian $\mathcal{H}_{int}$. For these systems the equation of motion becomes

$$\begin{aligned}&i\frac{\partial a(\boldsymbol{k},t)}{\partial t}-\omega(\boldsymbol{k})a(\boldsymbol{k},t) \\ &\quad = \frac{\delta\mathcal{H}_3}{\delta a^*(\boldsymbol{k},t)} \\ &\quad = \int\Big[\frac{1}{2}V(\boldsymbol{k};\boldsymbol{k}_1,\boldsymbol{k}_2)\,a(\boldsymbol{k}_1)\,a(\boldsymbol{k}_2)\,\delta(\boldsymbol{k}-\boldsymbol{k}_1-\boldsymbol{k}_2) \\ &\qquad + V^*(\boldsymbol{k}_1;\boldsymbol{k},\boldsymbol{k}_2)\,a(\boldsymbol{k}_1)\,a^*(\boldsymbol{k}_2)\,\delta(\boldsymbol{k}_1-\boldsymbol{k}-\boldsymbol{k}_2) \\ &\qquad + \frac{1}{2}U(\boldsymbol{k},\boldsymbol{k}_1,\boldsymbol{k}_2)\,a^*(\boldsymbol{k}_1)\,a^*(\boldsymbol{k}_2)\,\delta(\boldsymbol{k}_1+\boldsymbol{k}_2+\boldsymbol{k})\Big]\,d\boldsymbol{k}_1\,d\boldsymbol{k}_2\ . \qquad (3.13)\end{aligned}$$

Notice that I have retained the U-term, which was left out in Ref. [31, Chap. 2]. If ω does not satisfy the condition (3.6), but only the decay condition (3.5), the U-term can be eliminated by a canonical transformation. I will keep the U-term in the derivation of the three-wave kinetic equation below.

From the equation of motion above the time-derivative of $n(\boldsymbol{k},t)$ is derived to the lowest non-trivial order. For brevity, let $a_j = a(\boldsymbol{k}_j,t)$, $\omega_j = \omega(\boldsymbol{k}_j)$, $V_{k12} =$

$V(\boldsymbol{k};\boldsymbol{k}_1,\boldsymbol{k}_2)$ and similar for U. The idea is to express $\partial n/\partial t$ through correlators of more fields (I avoid the term "higher order correlators" since that may be confused with the expansion in terms of the nonlinearity), ideally by free-field correlators if they exist. It turns out, as we shall see, that $\partial n/\partial t$ is expressed via three-wave correlators; three-wave correlators vanish in the free-field approximation, so we need to find the three-wave correlators to the next non-trivial order. This means that we must find the equation of motion for the three-wave correlators. This is the path followed in Ref. [31], although they leave out the U term. I will here follow the same path, keeping track of the U-contributions.

First, to find the derivative $\partial n/\partial t$ we use the equation of motion (3.13) for $a_{k'}$ and a_k^*, multiplied by a_k^* resp. $a_{k'}$

$$\begin{aligned}
\frac{\partial}{\partial t}\langle a_k^* a_{k'}\rangle &= \left\langle \frac{\partial a_{k'}}{\partial t} a_k^* + \frac{\partial a_k^*}{\partial t} a_{k'} \right\rangle \\
&= -i(\omega_{k'} - \omega_k)\langle a_k^* a_{k'}\rangle \\
&\quad - i\left\langle \int \Big\{ \frac{1}{2} V_{k'12}\, a_1\, a_2\, a_k^*\, \delta(\boldsymbol{k}' - \boldsymbol{k}_1 - \boldsymbol{k}_2) \right. \\
&\qquad + V^*_{1k'2}\, a_1\, a_2^*\, a_k^*\, \delta(\boldsymbol{k}_1 - \boldsymbol{k}' - \boldsymbol{k}_2) \\
&\qquad \left. + \frac{1}{2} U_{k'12}\, a_1^*\, a_2^*\, a_k^*\, \delta(\boldsymbol{k}_1 + \boldsymbol{k}_2 + \boldsymbol{k}') \Big\}\, d\boldsymbol{k}_1\, d\boldsymbol{k}_2 \right\rangle \\
&\quad + i\left\langle \int \Big\{ \frac{1}{2} V^*_{k12}\, a_1^*\, a_2^*\, a_{k'}\, \delta(\boldsymbol{k} - \boldsymbol{k}_1 - \boldsymbol{k}_2) \right. \\
&\qquad + V_{1k2}\, a_1^*\, a_2\, a_{k'}\, \delta(\boldsymbol{k}_1 - \boldsymbol{k} - \boldsymbol{k}_2) \\
&\qquad \left. + \frac{1}{2} U^*_{k12}\, a_1\, a_2\, a_{k'}\, \delta(\boldsymbol{k}_1 + \boldsymbol{k}_2 + \boldsymbol{k}) \Big\}\, d\boldsymbol{k}_1\, d\boldsymbol{k}_2 \right\rangle \\
&= -i(\omega_{k'} - \omega_k)\langle a_k^* a_{k'}\rangle \\
&\quad - i\int \Big\{ \frac{1}{2}\left(V_{k'12} J_{k12} - V^*_{k12} J^*_{k'12}\right) \delta(\boldsymbol{k}' - \boldsymbol{k}_1 - \boldsymbol{k}_2)\delta(\boldsymbol{k} - \boldsymbol{k}_1 - \boldsymbol{k}_2) \\
&\qquad + \left(V^*_{1k'2} J^*_{12k} - V_{1k2} J_{12k'}\right) \delta(\boldsymbol{k}_1 - \boldsymbol{k}_2 - \boldsymbol{k})\delta(\boldsymbol{k}_1 - \boldsymbol{k}' - \boldsymbol{k}_2) \\
&\qquad + \frac{1}{2}\left(U_{1k'2} K_{12k} - U^*_{1k2} K^*_{12k'}\right) \\
&\qquad\qquad \times \delta(\boldsymbol{k}_1 + \boldsymbol{k}_2 + \boldsymbol{k})\delta(\boldsymbol{k}_1 + \boldsymbol{k}' + \boldsymbol{k}_2) \Big\}\, d\boldsymbol{k}_1 d\boldsymbol{k}_2
\end{aligned} \tag{3.14}$$

where the following correlators were introduced

$$J_{123}\,\delta(\boldsymbol{k}_1 - \boldsymbol{k}_2 - \boldsymbol{k}_3) = \langle a_1^*\, a_2\, a_3\rangle \tag{3.15}$$

and

$$K_{123}\,\delta(\boldsymbol{k}_1+\boldsymbol{k}_2+\boldsymbol{k}_3)=\langle a_1^*\,a_2^*\,a_3^*\rangle\,. \tag{3.16}$$

Thus the time derivative of $n(\boldsymbol{k},t)$ can be written

$$\begin{aligned}\frac{\partial}{\partial t}n(\boldsymbol{k},t) \;&=\; \mathrm{Im}\int\{V_{k12}J_{k12}\,\delta(\boldsymbol{k}-\boldsymbol{k}_1-\boldsymbol{k}_2)\\ &\quad -2V_{1k2}J_{1k2}\,\delta(\boldsymbol{k}_1-\boldsymbol{k}-\boldsymbol{k}_2)+U_{k12}K_{k12}\,\delta(\boldsymbol{k}+\boldsymbol{k}_1+\boldsymbol{k}_2)\}\,d\boldsymbol{k}_1\,d\boldsymbol{k}_2\end{aligned} \tag{3.17}$$

This constitutes the start of a hierarchy in which correlators are expressed in terms of more-field correlators. To close the hierarchy we must approximate the many-field correlators, in this case by the free-field approximation. As noted above, the correlation functions J and K vanish in the free-field approximation. To obtain a non-trivial result we must therefore go to next order to find non-vanishing J and K, i.e. we must determine J and K from their equations of motion. The equations of motion for J and K are found by almost identical methods. The expression for $\partial J/\partial t$ is found in Ref. [31] for a $\mathcal{H}_3$ that does not contain a U-term. It is easily confirmed that the expression does not change when the U-term is included in $\mathcal{H}_3$. Here below I will show how to derive the equation of motion for K and how to solve the equation. The result is expressed in terms of four-wave correlators, some of which are non-vanishing even for free fields. It is therefore sufficient to use the free-field approximation of the four-wave correlators. The non-vanishing four-wave correlators are of the form $\langle a^*a^*aa\rangle$, given by Eq. (3.12). Proceeding as for Eq. (3.14) we find

$$\begin{aligned}&-i\,\frac{\partial K_{123}}{\partial t}\,\delta(\boldsymbol{k}_1+\boldsymbol{k}_2+\boldsymbol{k}_3)\\ &=\; -i\left\langle\frac{\partial a_1^*}{\partial t}a_2^*a_3^*+\frac{\partial a_2^*}{\partial t}a_1^*a_3^*+\frac{\partial a_3^*}{\partial t}a_2^*a_1^*\right\rangle\\ &=\; (\omega_1+\omega_2+\omega_3)\langle a_1^*a_2^*a_3^*\rangle\\ &\quad+\frac{1}{2}\left\langle\int\{U_{145}^*a_4\,a_5\,a_2^*\,a_3^*\,\delta(\boldsymbol{k}_1+\boldsymbol{k}_4+\boldsymbol{k}_5)\right.\\ &\qquad+U_{245}^*a_4\,a_5\,a_1^*\,a_3^*\,\delta(\boldsymbol{k}_2+\boldsymbol{k}_4+\boldsymbol{k}_5)\\ &\qquad\left.+\;U_{345}^*a_4\,a_5\,a_1^*\,a_2^*\,\delta(\boldsymbol{k}_3+\boldsymbol{k}_4+\boldsymbol{k}_5)\}\,d\boldsymbol{k}_4\,d\boldsymbol{k}_5\right\rangle\\ &=\; (\omega_1+\omega_2+\omega_3)K_{123}\,\delta(\boldsymbol{k}_1+\boldsymbol{k}_2+\boldsymbol{k}_3)\end{aligned}$$

$$
\begin{aligned}
&+\frac{1}{2}\int \{U^*_{145} n_2 n_3[\delta(\boldsymbol{k}_2-\boldsymbol{k}_4)\delta(\boldsymbol{k}_3-\boldsymbol{k}_5)+\delta(\boldsymbol{k}_2-\boldsymbol{k}_5)\delta(\boldsymbol{k}_3-\boldsymbol{k}_4)]\delta(\boldsymbol{k}_1+\boldsymbol{k}_4+\boldsymbol{k}_5)\\
&+U^*_{245} n_1 n_3[\delta(\boldsymbol{k}_1-\boldsymbol{k}_4)\delta(\boldsymbol{k}_3-\boldsymbol{k}_5)+\delta(\boldsymbol{k}_1-\boldsymbol{k}_5)\delta(\boldsymbol{k}_3-\boldsymbol{k}_4)]\delta(\boldsymbol{k}_2+\boldsymbol{k}_4+\boldsymbol{k}_5)\\
&+U^*_{345} n_1 n_2[\delta(\boldsymbol{k}_1-\boldsymbol{k}_4)\delta(\boldsymbol{k}_2-\boldsymbol{k}_5)+\delta(\boldsymbol{k}_1-\boldsymbol{k}_5)\delta(\boldsymbol{k}_2-\boldsymbol{k}_4)]\delta(\boldsymbol{k}_3+\boldsymbol{k}_4+\boldsymbol{k}_5)\}\, d\boldsymbol{k}_4\, d\boldsymbol{k}_5\\
&= (\omega_1+\omega_2+\omega_3) K_{123}\,\delta(\boldsymbol{k}_1+\boldsymbol{k}_2+\boldsymbol{k}_3)\\
&\quad + U^*_{123}(n_2n_3+n_1n_3+n_1n_2)\delta(\boldsymbol{k}_1+\boldsymbol{k}_2+\boldsymbol{k}_3)\ . \qquad (3.18)
\end{aligned}
$$

The four-wave correlators that were used do not depend on time, but since it is merely an approximation to use the free fields even at this recursive step, the $n(\boldsymbol{k})$'s may have a slow time dependence. Ignoring this dependence for a moment, the equation to solve is

$$\{-i\frac{\partial}{\partial t}-(\omega_1+\omega_2+\omega_3)\}K_{123}(t)=U^*_{123}(n_2n_3+n_1n_3+n_1n_2)\equiv C \qquad (3.19)$$

where C is a constant. The equation has the solution

$$K_{123}(t)=-\frac{C\exp(i(\omega_1+\omega_2+\omega_3)t)}{\omega_1+\omega_2+\omega_3}+\frac{C}{\omega_1+\omega_2+\omega_3}\,. \qquad (3.20)$$

When this solution is inserted into the equation of motion for $n(\boldsymbol{k},t)$, Eq. (3.17), the first term may be neglected due to its oscillating character at $t>0$. For the second term we make use of the Cauchy formula [32, App. A-2]

$$\int\frac{f(x)}{x-x_0\mp i\varepsilon}dx=\mathrm{P}\int\frac{f(x)}{x-x_0}dx\pm i\pi\int\delta(x-x_0)f(x)dx \qquad (3.21)$$

with the pole at $x-x_0\equiv\omega_1+\omega_2+\omega_3$. This, and similar results for J_{123}, finally lead to the three-wave kinetic equation

$$
\begin{aligned}
\frac{\partial n(\boldsymbol{k},t)}{\partial t} &= \pi\int\Big[|V_{k12}|^2 f_{k12}\delta(\boldsymbol{k}-\boldsymbol{k}_1-\boldsymbol{k}_2)\delta(\omega_k-\omega_1-\omega_2)\\
&\quad -2|V_{1k2}|^2 f_{1k2}\delta(\boldsymbol{k}_1-\boldsymbol{k}-\boldsymbol{k}_2)\delta(\omega_1-\omega_k-\omega_2)\\
&\quad -|U_{k12}|^2 g_{k12}\delta(\boldsymbol{k}+\boldsymbol{k}_1+\boldsymbol{k}_2)\delta(\omega_k+\omega_1+\omega_2)\Big]\, d\boldsymbol{k}_1 d\boldsymbol{k}_2\\
&\equiv I(\boldsymbol{k},t) \qquad (3.22)
\end{aligned}
$$

with $f_{k12}\equiv n_1n_2-n_kn_1-n_kn_2$ and $g_{k12}\equiv n_1n_2+n_kn_1+n_kn_2$ (note: the second term has wrong sign in [31, Eq. (2.1.12a)]). $I(\boldsymbol{k},t)$ is called the collision integral. For capillary waves a canonical transformation can remove the U-term in $\mathcal{H}_3$ and the third term above vanishes, as in Ref. [31].

3.2.2 The Four-Wave Kinetic Equation

For four-wave interactions described by the Hamiltonian (3.7), the kinetic equation is derived similarly [31]

$$\frac{\partial n(\boldsymbol{k},t)}{\partial t} = \frac{\pi}{2}\int |T_{k123}|^2 f_{k123}\delta(\boldsymbol{k}+\boldsymbol{k}_1-\boldsymbol{k}_2-\boldsymbol{k}_3) \times \delta(\omega_k+\omega_1-\omega_2-\omega_3)d\boldsymbol{k}_1 d\boldsymbol{k}_2 d\boldsymbol{k}_3 \tag{3.23}$$

where $f_{k123} \equiv n_2 n_3(n_1+n_k) - n_1 n_k(n_2+n_3)$. The four-wave kinetic equation is relevant for gravity waves.

3.3 Application to Surface Waves

To connect the above rather formal formulations to the problem of the motion of surface waves, the starting point is the usual: The fluid is described by the Navier-Stokes equation and the continuity equation

$$\frac{\partial \boldsymbol{v}}{\partial t} + (\boldsymbol{v}\boldsymbol{\nabla})\boldsymbol{v} = -\frac{\boldsymbol{\nabla} p}{\rho} - \nu\boldsymbol{\nabla}\times(\boldsymbol{\nabla}\times\boldsymbol{v}) \tag{3.24}$$

$$\frac{\partial \rho}{\partial t} + \boldsymbol{\nabla}\cdot(\rho\boldsymbol{v}) = 0 \tag{3.25}$$

Here $\boldsymbol{v}(\boldsymbol{r},z,t)$ is the fluid velocity at position $(\boldsymbol{r},z)$, $p(\boldsymbol{r},z)$ is the pressure, $\rho(\boldsymbol{r},z)$ is the fluid density, and ν is the kinematic viscosity. The system is described in a laboratory frame coordinate system that has the horizontal coordinates $\boldsymbol{r}=(x,y)$ and the vertical coordinate z. The vertical coordinate is zero at the equilibrium position of the fluid surface, and the bottom of the fluid is at $z=-h$.

We assume that the fluid is incompressible, that it is inviscid on the length scales considered here, that it has a free surface, and that it is irrotational (vorticity free), thus allowing for a (three-dimensional) flow potential $\Phi(\boldsymbol{r},z,t)$ related to the (three-dimensional) flow velocity by $\boldsymbol{v}(\boldsymbol{r},z,t) = \boldsymbol{\nabla}\Phi(\boldsymbol{r},z,t)$. The deviation of the fluid surface from the equilibrium position $z=0$ is given by $\eta(\boldsymbol{r},t)$. Since we will be concerned with the surface motion, we introduce the restriction of Φ to the fluid surface $z=\eta(\boldsymbol{r},t)$ by $\Psi(\boldsymbol{r},t) \equiv \Phi(\boldsymbol{r},\eta(\boldsymbol{r},t),t)$. The fluid density is $\rho(\boldsymbol{r},z,t) = \rho_0\Theta(\eta-z)$, which expresses the obvious fact that the fluid density is zero above the surface $[z>\eta(\boldsymbol{r},t)]$ and constant (incompressible) below. It is known [9, 31] that under these assumptions the fluid is a Hamiltonian system in

which the surface elevation $\eta(\boldsymbol{r},t)$ and the (surface) flow potential $\Psi(\boldsymbol{r},t)$ act as canonical variables

$$\frac{\partial\eta(\boldsymbol{r},t)}{\partial t} = -\frac{\delta\mathcal{H}}{\delta\Psi(\boldsymbol{r},t)} \tag{3.26}$$

$$\frac{\partial\Psi(\boldsymbol{r},t)}{\partial t} = \frac{\delta\mathcal{H}}{\delta\eta(\boldsymbol{r},t)} \tag{3.27}$$

where the Hamiltonian is given by

$$\mathcal{H} = \frac{\rho_0}{2}\int\int_{-h}^{\eta} |\boldsymbol{\nabla}\Phi(\boldsymbol{r},z,t)|^2\, dz\, d\boldsymbol{r} + \sigma\int\left[\sqrt{1+|\boldsymbol{\nabla}_\perp\eta|^2}-1\right]d\boldsymbol{r} + \frac{g\rho_0}{2}\int|\eta|^2 d\boldsymbol{r}. \tag{3.28}$$

The subscript "$\perp$" denotes the horizontal components, and σ is the coefficient of surface tension.

We would like to have the continuity equation (3.25) expressed as a condition on the surface. Eq. (3.25) can be rewritten as

$$0 = \frac{\partial\rho}{\partial t} + \boldsymbol{\nabla}\cdot(\rho\boldsymbol{v}) = \rho_0\,\delta(\eta-z)\left[\frac{\partial\eta}{\partial t} + \boldsymbol{\nabla}_\perp\eta\cdot\boldsymbol{v}_\perp - v_z\right]. \tag{3.29}$$

At the surface, the condition reads

$$\frac{\partial\eta}{\partial t} + \boldsymbol{\nabla}_\perp\eta\cdot\boldsymbol{v}_\perp = v_z \qquad \text{or} \qquad \frac{\partial\eta}{\partial t} = \left(-\frac{\partial\eta}{\partial x}, -\frac{\partial\eta}{\partial y}, 1\right)\cdot\boldsymbol{v} \tag{3.30}$$

which simply states that the velocity of the surface along its normal is the same as the component of the fluid velocity along the same direction, at the same point, the normal vector being

$$\hat{N} = \frac{(-\nabla_\perp\eta, 1)}{\sqrt{1+|\nabla_\perp\eta|^2}} \tag{3.31}$$

given in the $(\boldsymbol{r},z)$ coordinates.

The Fourier transforms of $\eta(\boldsymbol{r},t)$ and $\Psi(\boldsymbol{r},t)$ are[1]

$$\Psi(\boldsymbol{k},t) = \frac{1}{2\pi}\int\Psi(\boldsymbol{r},t)\exp(-i\,\boldsymbol{k}\cdot\boldsymbol{r})d\boldsymbol{r} \tag{3.32}$$

and

$$\eta(\boldsymbol{k},t) = \frac{1}{2\pi}\int\eta(\boldsymbol{r},t)\exp(-i\,\boldsymbol{k}\cdot\boldsymbol{r})d\boldsymbol{r} \tag{3.33}$$

[1]In Ref. [31] the volume factor in front of the integral is defined differently.

and they are related to the previously introduced complex wave amplitudes $a(\boldsymbol{k},t)$ and $a^*(\boldsymbol{k},t)$ via

$$\eta(\boldsymbol{k},t) = \sqrt{\frac{\lambda(k)}{2\rho_0}}\,[a(\boldsymbol{k},t)+a^*(-\boldsymbol{k},t)] \tag{3.34}$$

$$\Psi(\boldsymbol{k},t) = -i\,\frac{1}{\sqrt{2\rho_0\lambda(k)}}\,[a(\boldsymbol{k},t)-a^*(-\boldsymbol{k},t)] \tag{3.35}$$

where $\lambda(k) = \omega(k)/(g+\sigma k^2/\rho_0)$ [not to be confused with the wavelength λ]. For deep-water capillary waves (decay-case) the interaction coefficients in the expansion of the Hamiltonian are [33, 34]

$$\begin{aligned} V(k;k_1,k_2) = {} & \left(\frac{\sigma}{\rho_0^3}\right)^{1/4}\left\{\left(\frac{kk_1}{k_2}\right)^{1/4}[(k-k_1)^2-k_2^2]\right. \\ & +\left(\frac{kk_2}{k_1}\right)^{1/4}[(k-k_2)^2-k_1^2] \\ & \left.-\left(\frac{k_1k_2}{k}\right)^{1/4}[(k_1-k_2)^2-k^2]\right\} \end{aligned} \tag{3.36}$$

and

$$\begin{aligned} U(k,k_1,k_2) = {} & \left(\frac{\sigma}{\rho_0^3}\right)^{1/4}\left\{\left(\frac{kk_1}{k_2}\right)^{1/4}[k_2^2-(k-k_1)^2]\right. \\ & +\left(\frac{kk_2}{k_1}\right)^{1/4}[k_1^2-(k-k_2)^2] \\ & \left.+\left(\frac{k_1k_2}{k}\right)^{1/4}[k^2-(k_1-k_2)^2]\right\} \end{aligned} \tag{3.37}$$

with suitable numerical factors in front (which depend on, among other elements, the coefficients used in front of Fourier transforms, normalizations, etc. There does not seem to be any convention on these matters in this field, not even in papers that have common authors). Notice that V is invariant with respect to the change $k_1 \leftrightarrow k_2$, and U is invariant with respect to any permutation of its arguments, as expected from the expression for $\mathcal{H}_3$ (Eq. (3.3)).

For deep-water gravity waves (non-decay case) the interaction coefficient has the behavior [31, Chap. 1]

$$T(k,k_1;k_2,k_3) = \frac{k^3}{\rho} f[\tilde{k}_1,\tilde{k}_2,\tilde{k}_3,\cos\theta_{k1},\cos\theta_{k2},\cos\theta_{k3}] \tag{3.38}$$

where $\tilde{k}_j \equiv k_j/k$. The full expression for T is lengthy. The expression can be found e.g. in Ref. [34] or as a number of factors and terms in Ref. [31, Chap. 1].

3.4 Solution to the Kinetic Equation

Having obtained the equation of motion for the wave occupation number $n(\boldsymbol{k},t)$ for three-wave and four-wave interactions in Eqs. (3.22) and (3.23), the next step is to solve for $n(\boldsymbol{k},t)$.

The interaction Hamiltonian $\mathcal{H}_{int}$ describes the interaction of the waves. External effects, like dissipation and forcing, must be added 'by hand' by modifying the kinetic equation

$$\frac{\partial n(\boldsymbol{k},t)}{\partial t} = I(\boldsymbol{k},t) + \Gamma(\boldsymbol{k})n(\boldsymbol{k},t) \tag{3.39}$$

where $\Gamma(\boldsymbol{k})$ describes all external effects. As an example, viscous damping of waves is described by $\Gamma(\boldsymbol{k}) = -2\nu k^2$ [33].

The wave occupation number $n(\boldsymbol{k},t)$ is related to the Fourier transform $\varepsilon_\Gamma(\boldsymbol{k},t)$ of the energy density $\mathcal{E}$ in the weakly nonlinear limit through the lowest order Hamiltonian $\mathcal{H}_2$

$$\mathcal{E} = \langle \mathcal{H}_2 \rangle = \int \omega(k) \langle a(\boldsymbol{k},t) a^*(\boldsymbol{k},t) \rangle d\boldsymbol{k} = \int \omega(k) n(\boldsymbol{k},t) d\boldsymbol{k} = \int \varepsilon_\Gamma(\boldsymbol{k},t) d\boldsymbol{k}\,. \tag{3.40}$$

Energy and momentum must be conserved in the wave interactions. The rate of change of the energy density $d\mathcal{E}/dt$ as a *result of the wave interaction*, is described via the term in the kinetic equation that refers to the elementary wave interactions — the collision integral $I(\boldsymbol{k},t)$ — by the equation

$$\frac{\partial}{\partial t} \int \varepsilon(\boldsymbol{k},t) d\boldsymbol{k} = \int \omega(k) I(\boldsymbol{k},t) d\boldsymbol{k} = 0 \tag{3.41}$$

where $\varepsilon(\boldsymbol{k},t)$ refers to the part of the energy density that is due to the wave interactions. This relation allows for a continuity equation for $\varepsilon(\boldsymbol{k},t)$

$$\nabla \cdot \boldsymbol{p}(\boldsymbol{k},t) + \frac{\partial \varepsilon(\boldsymbol{k},t)}{\partial t} = 0 \tag{3.42}$$

where the energy density flux in $\boldsymbol{k}$ space is $\nabla \cdot \boldsymbol{p}(\boldsymbol{k},t) = -\omega(k) I(\boldsymbol{k},t)$.

We are looking for stationary solutions to the kinetic equations. From the kinetic equation with external effects (3.39) we see that stationarity implies

$$I(\boldsymbol{k},t) + \Gamma(\boldsymbol{k}) n(\boldsymbol{k},t) = 0\,. \tag{3.43}$$

In regions where there are no external effects (when $\Gamma(\boldsymbol{k}) \approx 0$) this reduces to $I(\boldsymbol{k}, t) = 0$. Thus in the inertial range we are looking for solutions to $I(\boldsymbol{k}, t) = 0$ that match the sources and sinks at the ends of the inertial range.

The systems we consider (mainly capillary waves, but also gravity waves) are isotropic systems. For those, the integrals in the energy density are

$$\mathcal{E} = \int E(k)dk = \int (2k)^{d-1}\pi\varepsilon(k)dk = \int (2k)^{d-1}\pi\omega(k)n(k,t)dk \tag{3.44}$$

in d-dimensional space. We are looking for stationary solutions of the form

$$n(k) = Ak^{-s_0} \tag{3.45}$$

that have a constant flux of energy with respect to the wave numbers k, $P = P(k)$. Locality in the inertial range is the assumption that only eddies of similar spatial extensions interact strongly. This leads to a constant flux of energy in k-space in the inertial range, being the size of the rate of dissipation at large k-scales. The energy flux satisfies, in the isotropic case,

$$\frac{d}{dk}P(k) = -\frac{\partial}{\partial t}E(k) = -(2k)^{d-1}\pi\omega(k)\frac{\partial n(k,t)}{\partial t} = -(2k)^{d-1}\pi\omega(k)I(k,t)\,. \tag{3.46}$$

(Note the misprint in [31, Eq. above (2.2.19)]) and at the border to the dissipative range the energy flux satisfies, from Eq. (3.43),

$$\frac{d}{dk}P(k) = \Gamma(k)E(k) \tag{3.47}$$

(Note the misprint in [31, Eq. (2.2.19)]).

From here I concentrate on decay systems, i.e. systems that are described by the three-wave interaction (3.3). We assume that the dispersion law and the interaction coefficient are scale invariant

$$\omega(\mu k) = \mu^{\alpha}\omega(k) \tag{3.48}$$

$$V(\mu\boldsymbol{k}, \mu\boldsymbol{k}_1, \mu\boldsymbol{k}_2) = \mu^{m}V(\boldsymbol{k}, \boldsymbol{k}_1, \boldsymbol{k}_2)\,. \tag{3.49}$$

The interaction coefficient may be written in terms of a dimensionless function F

$$|V(\boldsymbol{k}, \boldsymbol{k}_1, \boldsymbol{k}_2)|^2 = V_0^2\, k^{2m} F\left(\frac{\boldsymbol{k}_1}{k}, \frac{\boldsymbol{k}_2}{k}\right) \tag{3.50}$$

From the scale invariance of the dispersion law, Eq. (3.48), it follows that the dispersion law is a power function $\omega(k) = \beta k^{\alpha}$. We see that this includes the

case of capillary deep-water waves, which have $\alpha = 3/2$, $\beta = \sqrt{\sigma/\rho}$, $m = 9/4$, and $V_0 = (\sigma/\rho^3)^{1/4}$.

By integrating Eq. (3.46) from zero to $\tilde{k}$ one finds

$$P(\tilde{k}) = -\pi \int_0^{\tilde{k}} (2k)^{d-1} \omega(k) I(k) dk \tag{3.51}$$

We take a closer look at the collision integral $I(k,t)$, given by (3.22). The integral involves the interaction coefficient V, the wave occupation numbers n, and δ-functions of the wave vectors and of the frequencies. The occupation numbers n that we are searching for are isotropic, and in an isotropic system the coefficient V is invariant with respect to rotations, so the only angular dependence in the collision integral is in the wave-vector δ-functions $\delta(\boldsymbol{k}-\boldsymbol{k}_1-\boldsymbol{k}_2)$ and $\delta(\boldsymbol{k}_1-\boldsymbol{k}-\boldsymbol{k}_2)$ (I assume that the U-term in (3.22) has been removed by a transformation). The angular part of the first term in the collision integral becomes

$$\int_0^{\pi} \delta(k - k_1\cos\theta_1 - k_2\cos\theta_2)\delta(k_1\sin\theta_1 + k_2\sin\theta_2) d\theta_1 d\theta_2 \tag{3.52}$$

where θ_1 (θ_2) is the angle between $\boldsymbol{k}$ and $\boldsymbol{k}_1$ ($\boldsymbol{k}$ and $\boldsymbol{k}_2$). The integral expresses the fact that the three vectors $\boldsymbol{k}$, $\boldsymbol{k}_1$, and $\boldsymbol{k}_2$ must form a triangle in order for the integral not to vanish. For the fixed values of k, k_1, and k_2 and with angles in the range $[0,\pi]$, only one set of angles $\tilde{\theta}_1$ and $\tilde{\theta}_2$ lets the three vectors form a triangle. The integral gives for two-dimensional systems $\Delta_2^{-1} \equiv |kk_1\sin\tilde{\theta}_1|^{-1} = [2(k^2k_1^2 + k^2k_2^2 + k_1^2k_2^2) - k^4 - k_1^4 - k_2^4]^{-1/2}$, which is the inverse area of the parallelogram spanned by the vectors $\boldsymbol{k}$ and $\boldsymbol{k}_1$ (not the inverse area of the triangle, as claimed in [31]; also note the absolute value). The generalization to d dimensions is $\Delta_d \sim k^d$.

Returning to the expression for the energy flux (3.51) we rewrite the k-integral as an integral in ω-space

$$\begin{aligned} P(\tilde{k}) &= -\pi \int_0^{\tilde{k}} (2k)^{d-1} \omega(k) I(k) dk \\ &= -\int_0^{\tilde{\omega}} \omega I(\omega) d\omega \end{aligned} \tag{3.53}$$

where $I(\omega)$ is defined as

$$\begin{aligned} I(\omega) &\equiv \pi(2k)^{d-1} I(k) \left(\frac{d\omega(k)}{dk}\right)^{-1} \\ &= \pi^2 2^{d-1} k^{d-1} \left(\frac{d\omega(k)}{dk}\right)^{-1} \int \Delta_d^{-1} k_1^{d-1} \left(\frac{d\omega(k_1)}{dk_1}\right)^{-1} k_2^{d-1} \left(\frac{d\omega(k_2)}{dk_2}\right)^{-1} \times \end{aligned}$$

$$\times \{|V_{k12}|^2 f_{k12}\delta(\omega-\omega_1-\omega_2) - 2|V_{1k2}|^2 f_{1k2}\delta(\omega_1-\omega-\omega_2)\}d\omega_1\, d\omega_2$$

$$= \pi^2 2^{d-1}\alpha^{-3}\beta^{-3d/\alpha}\int \Delta_d^{-1}(\omega\omega_1\omega_2)^{-1+d/\alpha}\times$$

$$\times \{|V_{k12}|^2 f_{k12}\delta(\omega-\omega_1-\omega_2) - 2|V_{1k2}|^2 f_{1k2}\delta(\omega_1-\omega-\omega_2)\}d\omega_1\, d\omega_2\ . \tag{3.54}$$

Here f_{k12} and V_{k12} are now to be considered as functions of ω_k, ω_1, and ω_2. By using the scale invariance of the interaction coefficient (3.50) and the fact that $\Delta_d \sim k^d$ we finally find an expression for the energy flux

$$\begin{aligned}
P(\tilde{k}) &= -\int_0^{\tilde{\omega}} \omega I(\omega) d\omega \\
&= -\pi^2 2^{d-1}\alpha^{-3}\beta^{(2s_0-2m-3d)/\alpha} A^2 V_0^2 \int_0^{\tilde{\omega}} \omega \int \Delta_d^{-1}(\omega\omega_1\omega_2)^{-1+d/\alpha}\times \\
&\quad \times \{\omega^{\frac{2m}{\alpha}} F\left(\frac{k_1}{k},\frac{k_2}{k}\right)[(\omega_1\omega_2)^{-\frac{s_0}{\alpha}} - (\omega\omega_1)^{-\frac{s_0}{\alpha}} - (\omega\omega_2)^{-\frac{s_0}{\alpha}}]\delta(\omega-\omega_1-\omega_2) \\
&\quad - 2\omega_1^{\frac{2m}{\alpha}} F\left(\frac{k}{k_1},\frac{k_2}{k_1}\right)[(\omega\omega_2)^{-\frac{s_0}{\alpha}} - (\omega\omega_1)^{-\frac{s_0}{\alpha}} - (\omega_1\omega_2)^{-\frac{s_0}{\alpha}}]\delta(\omega_1-\omega-\omega_2)\} d\omega_1\, d\omega_2 d\omega \\
&= a(d,\alpha,m,s_0)\beta^{-2(d+m-s_0)/\alpha} A^2 V_0^2\, \tilde{\omega}^{2(d+m-s_0)/\alpha} \\
&= a(d,\alpha,m,s_0) A^2 V_0^2\, \tilde{k}^{2(d+m-s_0)}
\end{aligned} \tag{3.55}$$

where $a(d,\alpha,m,s_0)$ is a non-dimensional constant. We are looking for solutions for which the energy flux P is constant in $\tilde{k}$-space. We must therefore require that the exponent of $\tilde{k}$ be zero, thus $s_0 = d+m$ and $P = aA^2V_0^2$. The wave occupation number (3.45) is then

$$n(k) = \left(\frac{P}{aV_0^2}\right)^{1/2} k^{-m-d}\ , \tag{3.56}$$

and for capillary waves ($m = 9/4$, $d = 2$, and $V_0 = (\sigma/\rho^3)^{1/4}$)

$$n(k) = \left(\frac{P^2\rho^3}{a^2\sigma}\right)^{1/4} k^{-17/4}\ . \tag{3.57}$$

A more careful derivation (see e.g. Ref. [31]) yields

$$n(k) = 8\pi\left(\frac{4P^2\rho^3}{\sigma a^2}\right)^{1/4} k^{-17/4} \tag{3.58}$$

3.5 Comparison to Faraday Experiment

The theory of weak turbulence enables us to calculate the second moment of the relative particle velocities $\langle|\delta\boldsymbol{v}(R)|^2\rangle$. Summing up from the previous sections, the (deep-water) capillary waves have the dispersion relation $\omega = \sqrt{\sigma/\rho}\, k^{3/2}$ and the wave occupation number

$$n(k) = 8\pi \left(\frac{4P^2\rho^3}{\sigma a^2}\right)^{1/4} k^{-17/4} \tag{3.59}$$

where a is a non-dimensional constant given by an integral that has not been computed. To avoid confusion between the particle velocities $\boldsymbol{v}$ already defined in previous chapters, and the fluid velocity and its components defined in this chapter, the fluid velocity is renamed to $\boldsymbol{u}$ for the remainder of this chapter. The fluid velocity at the fixed point $(\boldsymbol{r}, z)$ is $\boldsymbol{u} = (\boldsymbol{u}_\perp(\boldsymbol{r}, z), u_z(\boldsymbol{r}, z)) = \boldsymbol{\nabla}\Phi$, with Φ being the bulk velocity potential. With the particles acting as tracers of the fluid motion on the surface, the particle velocity that we measure in the experiment is the horizontal component of the fluid velocity $\boldsymbol{u}$ *at* the surface, i.e. at variable vertical position $z = \eta(\boldsymbol{r}, t)$ so that $\boldsymbol{v}(\boldsymbol{r}) = \boldsymbol{u}_\perp(\boldsymbol{r}, z = \eta)$. We would like to be able to express the particle velocity in terms of the surface potential $\Psi(\boldsymbol{r}) = \Phi(\boldsymbol{r}, z = \eta)$, and we assume that we can approximate the particle velocity by

$$\boldsymbol{v}(\boldsymbol{r}) = \boldsymbol{u}_\perp(\boldsymbol{r}, z = \eta) = (\boldsymbol{\nabla}_\perp\, \Phi(\boldsymbol{r}, z))|_{z=\eta} \approx \boldsymbol{\nabla}_\perp \Phi(\boldsymbol{r}, z = \eta) = \boldsymbol{\nabla}_\perp \Psi(\boldsymbol{r}) \tag{3.60}$$

thus neglecting the $\boldsymbol{r}$ dependence of $\eta(\boldsymbol{r}, t)$.

The second moment of the relative particle velocities can be written as

$$\begin{aligned} \langle|\delta\boldsymbol{v}(R)|^2\rangle &= \langle[\boldsymbol{v}(\boldsymbol{r}+\boldsymbol{R}) - \boldsymbol{v}(\boldsymbol{r})]^2\rangle \\ &= 2\left[\langle|\boldsymbol{v}(\boldsymbol{r})|^2\rangle - \langle\boldsymbol{v}(\boldsymbol{r}+\boldsymbol{R})\cdot\boldsymbol{v}(\boldsymbol{r})\rangle\right] \end{aligned} \tag{3.61}$$

where we have used ensemble averaging. To evaluate the second term, we make use of the connection (3.35) between the Fourier component $\Psi(\boldsymbol{k})$ and the complex Fourier components $a(\boldsymbol{k})$ and $a^*(\boldsymbol{k})$. We find the velocity scalar product

$$\begin{aligned} &\boldsymbol{v}(\boldsymbol{r}+\boldsymbol{R})\cdot\boldsymbol{v}(\boldsymbol{r}) \\ &\quad= \frac{1}{2\pi}\int \boldsymbol{v}(\boldsymbol{k})\cdot\boldsymbol{v}(-\boldsymbol{k})\exp(-i\boldsymbol{k}\cdot\boldsymbol{R})\,d\boldsymbol{k} \\ &\quad= \frac{1}{2\pi}\int (i\boldsymbol{k})(-i\boldsymbol{k})\Psi(\boldsymbol{k})\Psi(-\boldsymbol{k})\exp(-i\boldsymbol{k}\cdot\boldsymbol{R})\,d\boldsymbol{k} \end{aligned}$$

$$= \frac{1}{2\pi}\int \frac{(-k^2)}{2\lambda(k)}\{a(\boldsymbol{k})-a^*(-\boldsymbol{k})\}\{a(-\boldsymbol{k})-a^*(\boldsymbol{k})\}\exp(-i\boldsymbol{k}\cdot\boldsymbol{R})\,d\boldsymbol{k} \quad (3.62)$$

We need to ensemble average the scalar product (3.62). In our experiment we average over certain particles only, namely the particles that at some point in time are close to other particles. Even with this rather special ensemble we expect the random phase approximation, which is used to eliminate the fast phases of the fields a, to be valid.

Although correlators like $\langle a(\boldsymbol{k})a(-\boldsymbol{k})\rangle$ do not necessarily vanish when small nonlinearities are present, as they would for free fields, those correlators are small compared to the correlator $\langle a(\boldsymbol{k})a^*(\boldsymbol{k})\rangle = n(\boldsymbol{k})$, and their contribution can be neglected. The velocity correlator can then be calculated as

$$\begin{aligned}
&\langle \boldsymbol{v}(\boldsymbol{r}+\boldsymbol{R})\cdot\boldsymbol{v}(\boldsymbol{r})\rangle \\
&= -\frac{1}{4\pi}\int \frac{k^2}{\lambda(k)}\{-\langle a(\boldsymbol{k})a^*(\boldsymbol{k})\rangle - \langle a^*(-\boldsymbol{k})a(-\boldsymbol{k})\rangle\}\exp(-i\boldsymbol{k}\cdot\boldsymbol{R})\,d\boldsymbol{k} \\
&= \frac{1}{4\pi}\int \frac{k^2}{\lambda(k)}\{n(\boldsymbol{k})+n(-\boldsymbol{k})\}\exp(-i\boldsymbol{k}\cdot\boldsymbol{R})\,d\boldsymbol{k} \\
&= \frac{1}{2\pi}\int \frac{k^2}{\lambda(k)}n(k)\exp(-i\boldsymbol{k}\cdot\boldsymbol{R})\,d\boldsymbol{k} \qquad (3.63)
\end{aligned}$$

where I made use of the isotropy in capillary waves and in gravity waves, $n(\boldsymbol{k}) = n(k)$. For deep-water waves the factor $\lambda(k)$ is

$$\lambda(k) = \frac{\omega(k)}{g+\sigma k^2/\rho} = \frac{k}{\omega(k)} \quad (3.64)$$

and in the case of deep-water capillary waves ($k \gg \sqrt{g\rho/\sigma}$)

$$\lambda(k) = \sqrt{\frac{\rho}{\sigma}}\,k^{-1/2} \quad (3.65)$$

The second moment of the velocity differences, Eq. (3.61), then becomes

$$\begin{aligned}
\langle|\delta\boldsymbol{v}(R)|^2\rangle &= \frac{1}{\pi}\int_k\int_{\theta=0}^{2\pi}\frac{k^3 n(k)}{\lambda(k)}\left\{1-e^{-ikR\cos\theta}\right\}d\theta\,dk \\
&= 32\left(\frac{4P^2\rho\,\sigma}{a^2}\right)^{1/4}\int_k\int_{\theta=0}^{\frac{\pi}{2}}\frac{k^3k^{-17/4}}{k^{-1/2}}\{1-\cos(kR\cos\theta)\}\,d\theta\,dk \\
&= 32\left(\frac{4P^2\rho\,\sigma}{a^2}\right)^{1/4}R^{-1/4}\int_{s=s_l}^{s_u}\int_{\theta=0}^{\frac{\pi}{2}}s^{-3/4}\{1-\cos(s\cos\theta)\}\,d\theta\,ds \\
&\qquad (3.66)
\end{aligned}$$

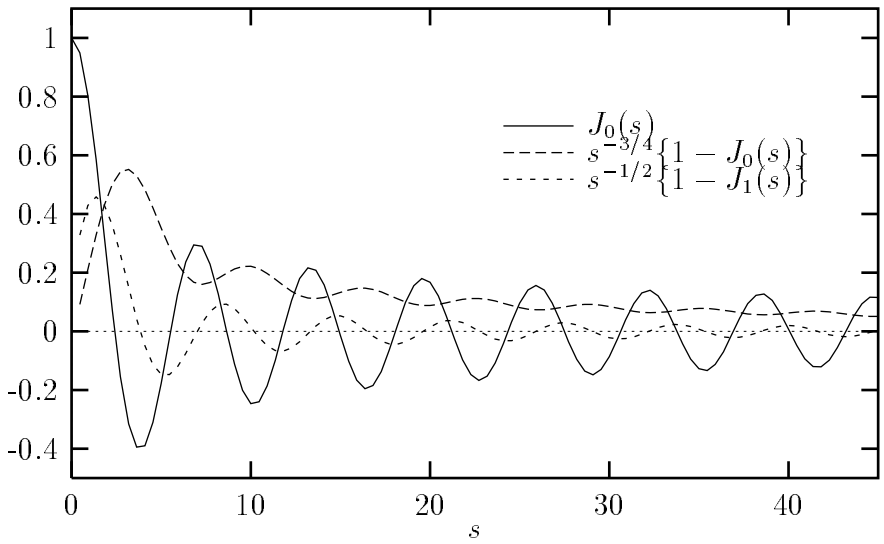

Figure 3.1: The Bessel functions $J_0(s)$ and $J_1(s)$, damped by inverse powers of s.

where the upper and lower bounds on s are $s_u \equiv Rk_{max} \approx 2\pi R/\lambda$ and $s_l \equiv Rk_{min} = 2\pi R/L \approx 0$, with L ($\gg R$) being the system size. The integrand is zero in the limit $s \to 0$ (see also Fig. 3.1 and Eq. (3.68) below).

The Bessel functions (of the first kind) have the integral representation

$$J_\nu(z) = \frac{2(z/2)^\nu}{\Gamma(\nu+\frac{1}{2})\Gamma(\frac{1}{2})} \int_0^{\frac{\pi}{2}} (\sin\theta)^{2\nu} \cos(z\cos\theta) d\theta \ , \tag{3.67}$$

and the θ-integration over the second term in the integrand may therefore be expressed by the zeroth Bessel function

$$\int_0^{\frac{\pi}{2}} \cos(s\cos\theta) d\theta = \frac{\pi}{2} J_0(s) \ . \tag{3.68}$$

Thus the second moment of the velocity differences can be written as

$$\langle |\delta \boldsymbol{v}(R)|^2 \rangle \ = \ 16\pi \left(\frac{4P^2 \rho\, \sigma}{a^2} \right)^{1/4} R^{-1/4} \int_0^{s_u} s^{-3/4} \{1 - J_0(s)\}\, ds \ . \tag{3.69}$$

For large s, the second term is small compared to the first term and can be neglected, illustrated in Fig. 3.1. Therefore, in the second term the upper limit of the integral can be replaced by infinity. Then the second moment of the velocity

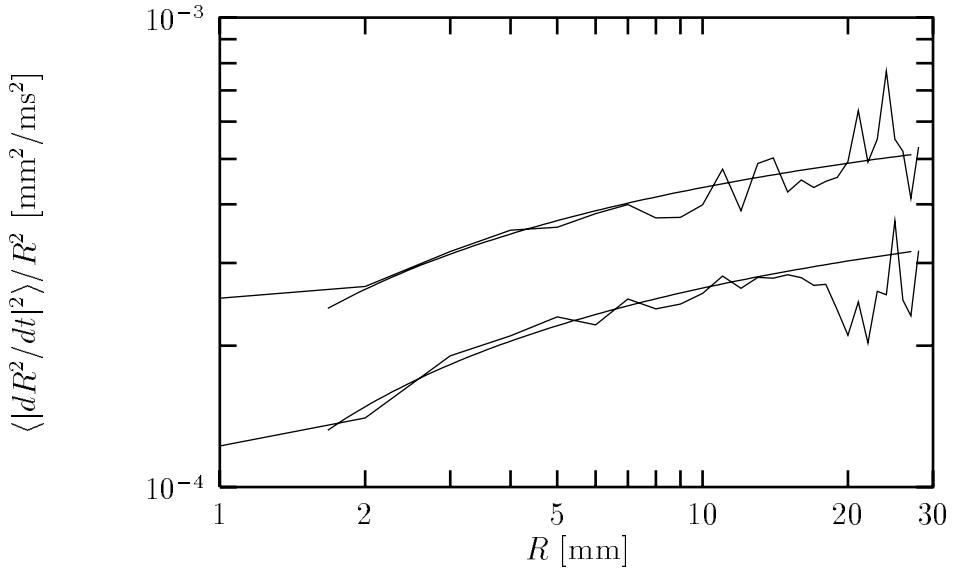

Figure 3.2: Fit of the theoretical prediction (3.70) to the Faraday relative diffusion experiment. Control parameters $\epsilon = 0.13$ (lower curve) and $\epsilon = 0.24$ (upper curve). In this fit we find $b(\epsilon = 0.13) = 0.66$ and $b(\epsilon = 0.24) = 0.62$.

differences becomes

$$\begin{aligned}
&\langle |\delta \boldsymbol{v}(R)|^2 \rangle \\
&\quad = 16\pi \left(\frac{4P^2 \rho \sigma}{a^2} \right)^{1/4} R^{-1/4} \left(\int_0^{s_u} s^{-3/4}\, ds - \int_0^{\infty} s^{-3/4} J_0(s)\, ds \right) \\
&\quad = 16\pi \left(\frac{4P^2 \rho \sigma}{a^2} \right)^{1/4} R^{-1/4} \left(4 s_u^{1/4} - 2^{-3/4} \frac{\Gamma(1/8)}{\Gamma(7/8)} \right) \\
&\quad = 64\pi \left(\frac{8\pi P^2 \rho \sigma}{a^2 \lambda} \right)^{1/4} \left(1 - \left(\frac{R}{\lambda} \right)^{-1/4} \frac{1}{8\pi^{1/4}} \frac{\Gamma(1/8)}{\Gamma(7/8)} \right) \\
&\quad = 64\pi \left(\frac{8\pi P^2 \rho \sigma}{a^2 \lambda} \right)^{1/4} \left(1 - b \left(\frac{R}{\lambda} \right)^{-1/4} \right)
\end{aligned} \tag{3.70}$$

with

$$b \equiv \frac{1}{8\pi^{1/4}} \frac{\Gamma(1/8)}{\Gamma(7/8)} \approx 0.649 \ . \tag{3.71}$$

There may be a ambiguity in the non-dimensional part of the factor in front of the expression, because it depends on e.g. how the volume factors in the Fourier

transformation are defined and whether or not the definitions are consistent in all results cited. The Bessel integral is found in e.g. Ref. [35, Eq. (6.561.14)].

Our measurements yield the longitudinal velocity differences $\delta v_{||}(R)$. Assuming that the longitudinal velocity differences behave as the vector velocity differences,

$$\langle |\delta \boldsymbol{v}(R)|^2 \rangle \sim \langle |\delta v_{||}(R)|^2 \rangle \,, \tag{3.72}$$

we can compare the prediction (3.70) to our data. In Figure 3.2 we plot the longitudinal velocity moment $\langle |dR^2/dt|^2 \rangle / R^2 = 4 \langle |\delta v_{||}(R)|^2 \rangle$ as a function of R, along with a fit to the form (3.70), for the two ϵ-values for which we have the most pair measurements.

Here we use the non-central moments, as opposed to Paper I where we used the central moments because they were more easily available to us at that time. Because the mean value is an order of magnitude smaller than the second moment, it essentially does not matter whether central moments are used, as can also be seen by comparing the figures here with the upper inset of Figure 3 in Paper I. In any case, we find that our observations are consistent with the prediction, with $b \approx 0.6$ fitted from the experiment. In Chapter 2 we found that the exponent characterizing a power-law behavior of $\langle |\delta v_{||}(R)|^2 \rangle$ was $\alpha_2 - 2 = 0.26$ (although this value was found for the central moment). We note that the TWT predicts an R-dependent exponent (in other words, it predicts that $\langle |\delta v_{||}(R)|^2 \rangle$ does not follow a power-law, as we see in Eq. (3.70)) that vanishes for very large separations R and has a small positive value in the range of R values studied in the experiment; see Figure 3.3. The TWT predicts the "exponent" 0.26 at separation $R \approx 7$ mm. It is difficult to distinguish whether the power laws of Chapter 2 or the TWT fit (3.70) is the right description of the experimental data. The TWT fit assumes that the energy flux P is constant in k-space, this does not take intermittency into account.

The only ϵ-dependent quantity in the prefactor of the fit (3.70) is P. From the fit in Fig. 3.2 we find $P(\epsilon = 0.24) \approx (2.4 \pm 0.4)\, P(\epsilon = 0.13)$; the energy flux grows with ϵ.

Finally, I consider the case of deep-water gravity waves. We cannot obtain gravity waves in our Faraday experiment with the present equipment, hence I cannot test the predictions obtained. However, new equipment may make it possible in the near future to create gravity waves, in which case the predictions should be tested.

For deep-water gravity waves the derivation of the second velocity moment

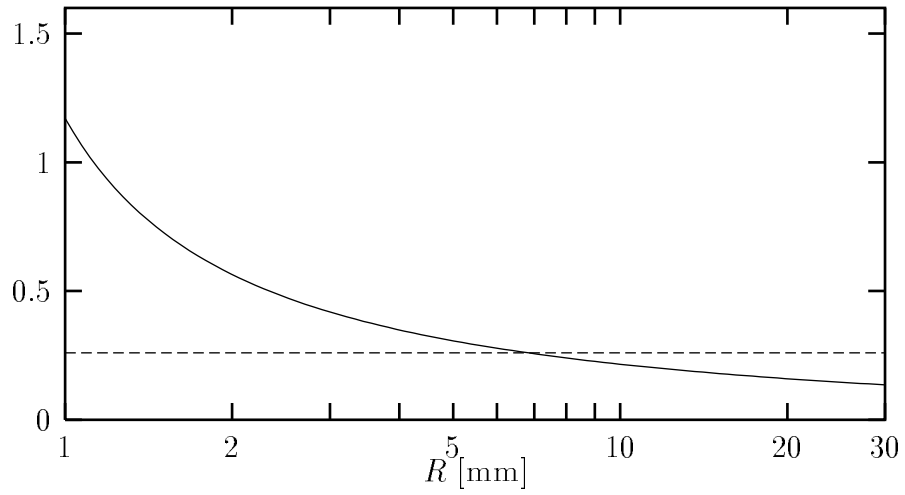

Figure 3.3: Weak wave turbulence predictions of the 'exponent' of $\langle|\delta v_{||}(R)|^2\rangle$. The dashed line at 0.26 is the exponent we found from the Faraday experiment in Chapter 2.

follows along the same lines as for capillary waves, although care must be taken to avoid divergencies. There are two isotropic solutions to the kinetic equation of the wave occupation number [31, 34]. The first solution corresponds to a constant flow P of energy to the short-wave region, like the capillary waves solution (3.59). The wave occupation number is

$$n(k) = B_1 k^{-4} = \left(\frac{P\rho^2}{a_1}\right)^{1/3} k^{-4} \tag{3.73}$$

where a_1 is a non-dimensional constant not yet computed. The second spectrum carries a constant flux Q of wave action towards the long-wave region

$$n(k) = B_2 k^{-23/6} = \left(\frac{Q^2 g\rho^4}{a_2^2}\right)^{1/6} k^{-23/6} \tag{3.74}$$

where the non-dimensional constant a_2 is not yet determined either. The integrals leading to a, a_1, and a_2 are found in Ref. [31]. Both spectra (3.73) and (3.74) agree with experiments, but the experiments do not allow to distinguish between the two [31]. The $\lambda(k)$-factor is in the case of gravity waves $\lambda(k) = k/\omega(k) = \sqrt{k/g}$.

First, I derive the second velocity moment for systems with the spectrum of constant energy flux (3.73). Starting from the expression found in the above

derivation for capillary waves one has

$$\begin{aligned}\langle|\delta\boldsymbol{v}(R)|^2\rangle &= 2\int \frac{k^3 n(k)}{\lambda(k)}\{1-J_0(kR)\}dk \\ &= 2R^{-1/2}B_1 g^{1/2}\int_0^{s_u} s^{-3/2}\{1-J_0(s)\}ds \\ &= 2R^{-1/2}B_1 g^{1/2}\left\{-2\left[s^{-1/2}\{1-J_0(s)\}\right]_0^{s_u}\right. \\ &\qquad \left.-(-2)\int_0^{s_u} s^{-1/2}J_1(s)\,ds\right\} \qquad (3.75)\end{aligned}$$

where I integrated by parts and took advantage of the relation $dJ_0(s)/ds = -J_1(s)$. The first term vanishes in the lower limit. In the second term the upper limit s_u may be replaced by infinity, due to the damped oscillatory character of $s^{-1/2}J_1(s)$. I find

$$\begin{aligned}\langle|\delta\boldsymbol{v}(R)|^2\rangle &= 2R^{-1/2}B_1 g^{1/2}\left\{-2s_u^{-1/2}+\sqrt{2}\frac{\Gamma(3/4)}{\Gamma(5/4)}\right\} \\ &= 2\left(\frac{8g^3\lambda^3P^2\rho^4}{\pi^3 a_1^2}\right)^{1/6}\left(-1+c_1\left(\frac{R}{\lambda}\right)^{1/2}\right) \qquad (3.76)\end{aligned}$$

where

$$c_1 = \sqrt{\pi}\,\frac{\Gamma(3/4)}{\Gamma(5/4)} \approx 2.396\ . \qquad (3.77)$$

This relation can be tested against gravity waves data the same way we tested the capillary result against data from the Faraday experiment.

By using the same method and the same considerations about the limits of the integrals, I find the velocity moment for systems with the spectrum of constant wave action flux (3.74)

$$\begin{aligned}\langle|\delta\boldsymbol{v}(R)|^2\rangle &= 6B_2 g^{1/2}R^{1/3}\left\{-s_u^{-1/3}+2^{-1/3}\frac{\Gamma(5/6)}{\Gamma(7/6)}\right\} \\ &= 3\left(\frac{4g^2Q\lambda\rho^2}{\pi a_2}\right)^{1/3}\left(-1+c_2\left(\frac{R}{\lambda}\right)^{1/3}\right) \qquad (3.78)\end{aligned}$$

where

$$c_2 = \pi^{1/3}\frac{\Gamma(5/6)}{\Gamma(7/6)} \approx 1.782\ . \qquad (3.79)$$

A simple plot of the two moments (3.76) and (3.78) shows that if the pre-factor in both cases is left to be fitted, an experimental test must provide separation data for two decades or more in order to see any significant difference in the two moments, thus distinguishing between the two spectra (3.73) and (3.74).

Chapter 4

Self-diffusion in Capillary Waves

The diffusion of particle pairs in the Faraday experiment was described in the previous chapters. This chapter describes the self-diffusion of particles, i.e. the single particle diffusion. First the data analysis is presented, with emphasis on the variance of the displacements projected onto one horizontal direction. Then I introduce the concept of fractional Brownian motion, a generalization of the ordinary Brownian motion, and I discuss the modeling of the particle motion by a convolution of two fractional Brownian motions. Finally the fractal dimension of the trajectories is measured.

4.1 Introduction

In measurements of the oceanic circulation the motion of drifters is considered to be a good approximation of the motion of the fluid elements [36]. The drifters can be buoys floating on the surface or submerged floats drifting at an approximately constant level below the surface. Often the drifters are tracked by position measurements from satellites.

Drifter motion has been studied in the North Atlantic by several groups, e.g. by the authors of Refs. [37, 38, 39]. They find that on time scales between roughly 1 day and 10 days, and on length scales between roughly 10 km and 100 km, the drifters move in a far from Brownian motion. They find that the variance of the motion in one of the horizontal directions x scales with time as a power law with an exponent 1.5, $\langle [x(t+\tau) - x(t)]^2 \rangle \propto \tau^{1.5}$, and not with the Brownian motion exponent 1. Other observations [36], at the Kuroshio extension off the coast of Japan, yield an exponent between 1.4 and 1.6. For scales larger than 100 km to 200 km [36] the dynamics is essentially governed by Rossby waves and zonal

flows [40], and the motion crosses over to Brownian motion. Also, the fractal dimension $\mathcal{D} \approx 1.3$ for the drifter trajectories has been determined [39, 41, 42] based on the 'yardstick method' [43].

We study the motion of drifters in a laboratory system. The basis of the present data analysis was the VCR tape that was also used for the analysis of relative diffusion, but naturally more particle tracks can be extracted when we do not impose the restriction that the particles must make up pairs ('pairs' are particles that at some point in time are 'close'), and the statistics is clearly better.

We find for the absolute motion that the character of the particle motion crucially depends on whether the length scale is larger or smaller than the wavelength λ. At length scales larger than λ the motion is close to being Brownian motion, but at length scales smaller than λ the motion changes character. Also, the character of the motion depends on the vibration amplitude $\mathcal{A}$, expressed through the control parameter $\epsilon = (\mathcal{A} - \mathcal{A}_c)/\mathcal{A}_c$. The motion is more Brownian-like the larger the vibration amplitudes are, i.e. for more disordered surfaces.

The analysis and the interpretation of the self-diffusion experiment are reported in Papers III and V. Below I give an introduction to the two Papers and summarize the main results. For details, please refer to Papers III and V.

More data is becoming available at the time of writing. Gaining access to more data may lead to new insights into the experiment. We plan to analyse the extended data set in the near future, this means that the interpretation of the experiment is ongoing work. The following data analysis is based on the old data set, as are Papers III and V.

4.2 Data Analysis

As discussed in Chapter 1, we measure the horizontal positions $\boldsymbol{r}(t) = (x(t), y(t))$ of the particles at time intervals $\Delta t = 20$ ms. The position is more accurately determined in the x-direction than in the y-direction, due to the smaller pixel size (≈ 1 mm in the x-direction and ≈ 3 mm in the y-direction). A major part of the following data analysis and discussion uses the projection of the motion onto one direction, as is common in the literature. It is thereby assumed that the motion in two arbitrary orthogonal directions can be considered to be independent. The better x-direction accuracy in our experiment suggests that we should concentrate on the motion in this direction, which indeed we do. We found only little difference in the behavior of the motion in the two directions, besides the

difference in accuracy.

A previous study by Ramshankar, Berlin, and Gollub (RBG) [10] reports measurements of diffusion of particles in the Faraday experiment. They found that the diffusivity D, as measured from the second moment (variance)

$$V(\tau) = \langle [x(t+\tau) - x(t)]^2 \rangle = 2D\tau \,, \tag{4.1}$$

was time dependent with $D(\tau) = A\tau^{2H-1}$, for time intervals exceeding 1 s. The exponent H decreased from $H \simeq 0.7$ right above the critical vibration amplitude $\mathcal{A}_c$, to $H = 0.5$ for larger vibration amplitudes corresponding to the control parameter $\epsilon \approx 0.4$. This is the same H-value as for ordinary Brownian motion (constant diffusivity D). A diffusivity that depends on the time-interval has the effect that the length traveled in one time interval depends on the length traveled in previous time intervals. This I shall return to in Section 4.3 below. RBG pointed out that motion with exponent $0 < H < 1$ can be modeled by a generalization of Brownian motion known as fractional Brownian motion (fBm).

We extended the studies by RBG to larger vibration amplitudes and smaller time scales. Like for the relative-diffusion measurements, we study the particles at vibration amplitudes corresponding to the control-parameter values $\epsilon = 0.05$, 0.13, 0.24, 0.34, 0.65, 0.86, and 1.06. It is worth noting that the size of the particles we used (50 μm) was less than that of the particles used by RBG (100-200 μm). Although ideally the particles can be considered as perfect tracers that follow the motion of the immediately neighboring fluid elements, the particle size may have an effect on how well the particles actually act as tracers. Typical particle tracks are shown in Figure 4.1 for three different vibration amplitudes.

From the measured particle tracks, we first studied the second moment $V(\tau) = \langle [\Delta x(\tau)]^2 \rangle$ of the displacements $\Delta x(\tau) = x(t+\tau) - x(t)$ for the seven different vibration amplitudes; see Figure 4.2. There is a slight mean drift of the particles, which we did not take into account in Fig. 4.2. However, the effect of the drift is small (it accounts for less than a few percent change in $\Delta x(\tau)$ in all cases) and it will be neglected. The mean drift appears because the particles are measured in a somewhat off-center area of the container; reflections of the light on the water surface prevent centered measurements.

The curves in Fig. 4.2 all have a cross-over between two different power-law behaviors at the ϵ-dependent time $\tau_c(\epsilon)$. The time $\tau_c(\epsilon)$ corresponds to a distance equal to the wavelength, $V(\tau_c) \simeq \lambda^2/2$ (recall that this refers to the displacement in one of the two independent directions, hence the one-half). The

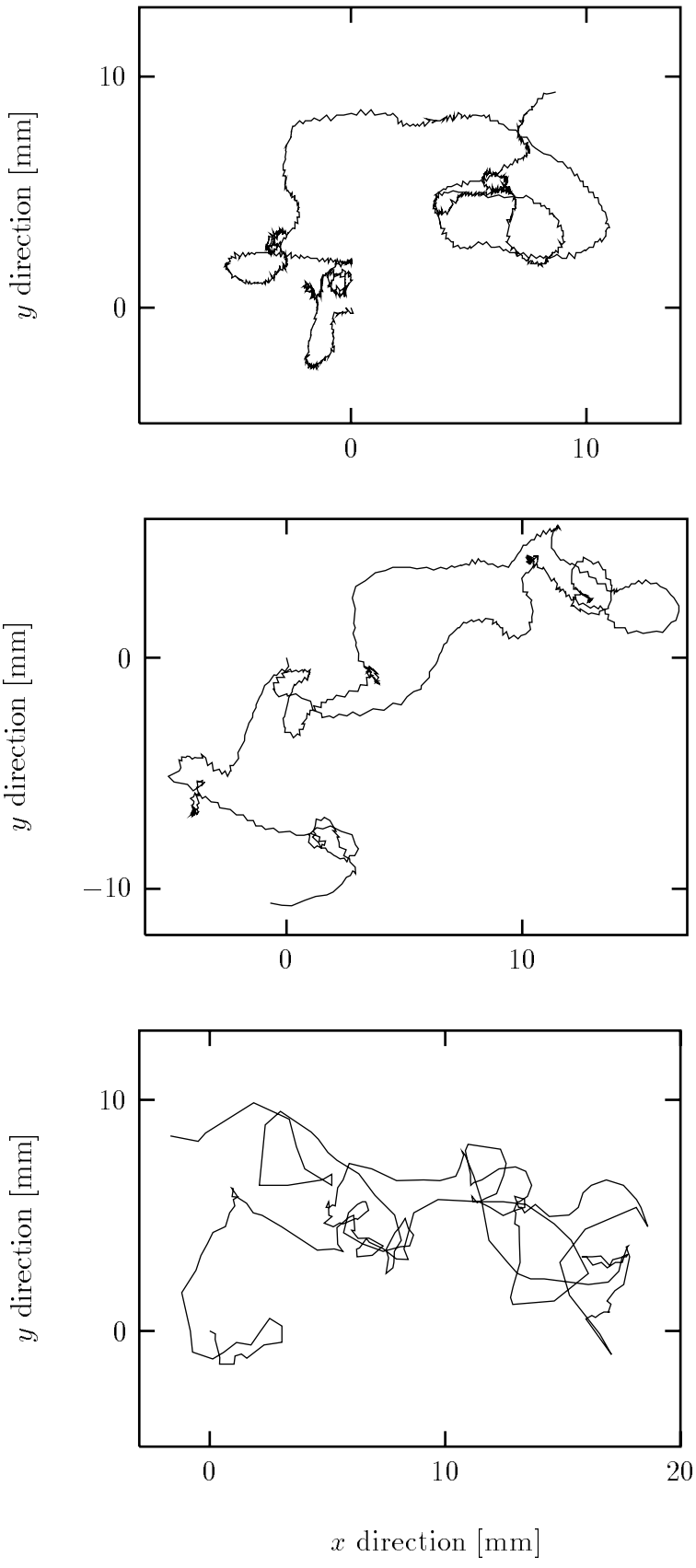
10
0
y direction [mm]
0
10
0
−10
y direction [mm]
0
10
10
0
y direction [mm]
0
10
20
x direction [mm]

Figure 4.1: (Previous page) Trajectories of particles for various values of the control parameter ϵ. *Top:* $\epsilon = 0.05$, the length of the track is 1106 time steps ($\approx$ 22 s). *Middle:* $\epsilon = 0.34$, the length of the track is 579 time steps ($\approx$ 12 s). *Bottom:* $\epsilon = 1.06$, the length of the track is 243 time steps ($\approx$ 5 s). The measured positions are connected by straight lines. The coordinate systems are all translated to have origo at the starting point of the particle trajectory, and the scale is the same in the three graphs.

change in behavior at scales corresponding to the wavelength λ is backed up by the preliminary analysis of the extended data set, which for the fourth (central) moment $\mathcal{M}_4(\tau)$ also shows a cross-over at the length scale λ, the value of $\mathcal{M}_4$ at the cross-over being the expected $\lambda^4/2$, see Fig. 4.3.

Returning to the variance $V(\tau)$ shown in Figs. 4.2, we see that the exponent $2H$ characterizing the change in the large time-scale variance $V(\tau > \tau_c) = 2A\tau^{2H}$ is smaller than the exponent $2H_\lambda$ for the short time-scale variance $V(\tau < \tau_c) = 2A_\lambda\tau^{2H_\lambda}$. For large ϵ, i.e. for very disordered surfaces ($\epsilon = 1.06$), the behavior at long time scales τ is Brownian-like with $2H = 1$. For less disordered surfaces (smaller ϵ) the diffusion is anomalous with values of $2H > 1$; see Table 4.1, and also Fig. 3 of Paper III. This is in accordance with the RBG results, except that in their experiment a Brownian-like motion is reached for smaller vibration amplitudes, $\epsilon \simeq 0.3$. The pre-factor $A(\epsilon)$ is approximately a factor of two larger than the pre-factor found by RBG. This difference is probably due to the larger particle size used in the experiments by RBG.

At small time scales, corresponding to length scales shorter than λ, we find that the exponent $2H_\lambda$ decreases from $2H_\lambda \simeq 1.9$ to 1.55 in the range of ϵ studied. For very short time scales the curves of $\epsilon = 0.05$ and 0.13 tend to bend towards a smaller slope. It happens at time scales τ less than $2\Delta t = 40$ ms, corresponding to x-direction displacements of less than $\sim$ 0.11 mm. Keeping in mind that the pixel size in the x-direction is $\approx$ 0.1 mm, we interpret the bending as a consequence of the uncertaincy in position caused by the pixel size. This is further verified by the fact that the short-times bending in the y-direction happens for times corresponding to distances that are larger, namely $\sim$ 0.17 mm, and the y-direction pixel size is $\approx$ 0.3 mm.

For a single power-law like $V(\tau) = 2A(\epsilon)\tau^{2H(\epsilon)}$ it is always possible to rescale the time scale τ of one curve (#2) to make it collapse with another curve (#1),

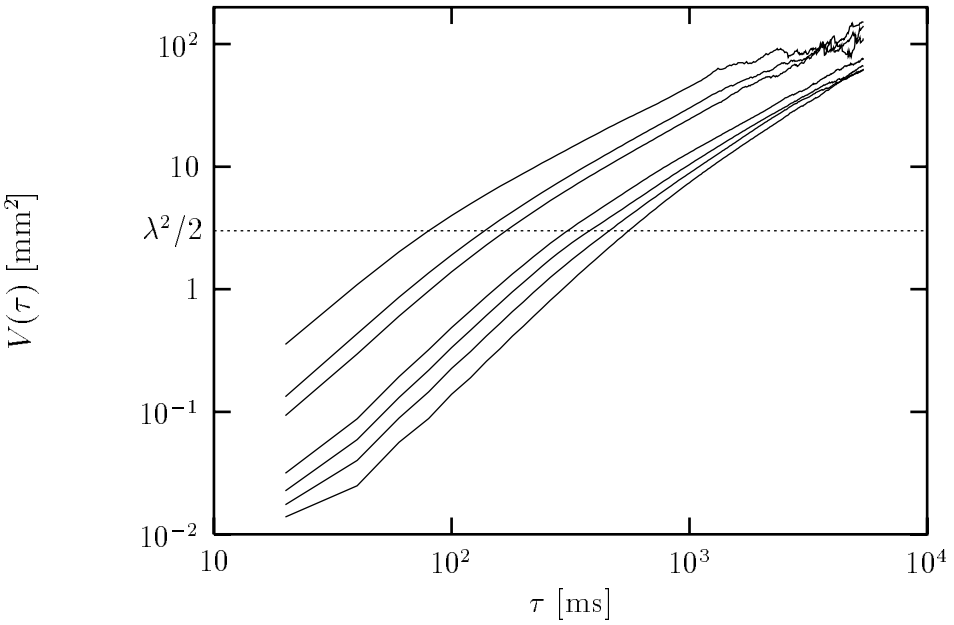

Figure 4.2: Self-diffusion. Variance along one coordinate axis as a function of the time interval τ. From below, $\epsilon = 0.05$, 0.13, 0.24, 0.34, 0.65, 0.86, and 1.06.

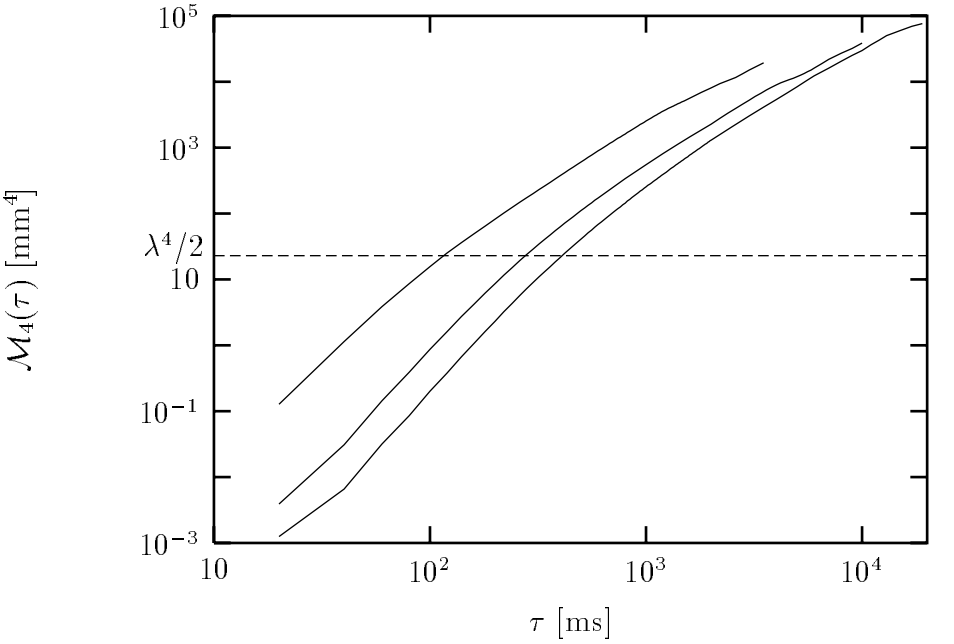

Figure 4.3: Self-diffusion. The fourth moment $\mathcal{M}_4(\tau) = \langle[\Delta x(\tau) - \langle\Delta x(\tau)\rangle]^4\rangle$ of the extended data set. From below $\epsilon = 0.13$, 0.34, and 0.86.

ϵ	$H(\epsilon)$	$1/H(\epsilon)$	$\mathcal{D}(\epsilon)$
0.05	0.63	1.59	1.65
0.13	0.59	1.69	1.72
0.24	0.57	1.77	1.76
0.34	0.55	1.82	1.81
0.65	0.54	1.87	1.89
0.86	0.53	1.87	1.95
1.06	0.50	2.00	2.00

Table 4.1: Self-diffusion. The values of the exponents $H(\epsilon)$, $1/H(\epsilon)$, and $\mathcal{D}(\epsilon)$ obtained by rescaling.

by rescaling the time variable in curve #2 as

$$\tau \to \left(\frac{A(\epsilon_2)}{A(\epsilon_1)}\right)^{1/(2H_1)} \tau^{H_2/H_1}. \tag{4.2}$$

This stems from the obvious fact that two linear curves can be made to collapse by a rescaling. It is, however, not clear a priori that curves made up of *two* power-laws can be rescaled to collapse above *and* below the cross-over point. This requires that the following four equations be fulfilled

$$A(\epsilon_1)\tau_1^{2H(\epsilon_1)} = A(\epsilon_2)\tau_2^{2H(\epsilon_2)} \quad \text{(Upper curve collapses)} \tag{4.3}$$

$$A_\lambda(\epsilon_1)\tau_1^{2H_\lambda(\epsilon_1)} = A_\lambda(\epsilon_2)\tau_2^{2H_\lambda(\epsilon_2)} \quad \text{(Lower curve collapses)} \tag{4.4}$$

$$A(\epsilon_1)\tau_c(\epsilon_1)^{2H(\epsilon_1)} = A(\epsilon_2)\tau_c(\epsilon_2)^{2H(\epsilon_2)} \quad \text{(Collapse at cross-over)} \tag{4.5}$$

$$A_\lambda(\epsilon_1)\tau_c(\epsilon_1)^{2H_\lambda(\epsilon_1)} = A_\lambda(\epsilon_2)\tau_c(\epsilon_2)^{2H_\lambda(\epsilon_2)} \quad \text{(Collapse at cross-over)} \tag{4.6}$$

Solving for τ_1 one finds

$$\frac{\tau_1}{\tau_c(\epsilon_1)} = \left(\frac{\tau_2}{\tau_c(\epsilon_2)}\right)^{\frac{H(\epsilon_2)}{H(\epsilon_1)}} = \left(\frac{\tau_2}{\tau_c(\epsilon_2)}\right)^{\frac{H_\lambda(\epsilon_2)}{H_\lambda(\epsilon_1)}} \tag{4.7}$$

which shows that the ratio $\gamma \equiv H_\lambda(\epsilon)/H(\epsilon)$ of the slopes of a curve must be independent of ϵ, i.e. constant across the range of curves. It also shows that if this is so, then plotting a curve using the rescaled time $\tilde{\tau} = (\tau/\tau_c)^{2H}$ will make the curve collapse with the curve having upper exponent $2H = 1$.

We found that for our data, the ratio γ is very close to being constant, with $\gamma = 1.55 \pm 0.05$. We plotted the variance by rescaling the time $\tau \to \tilde{\tau} =$

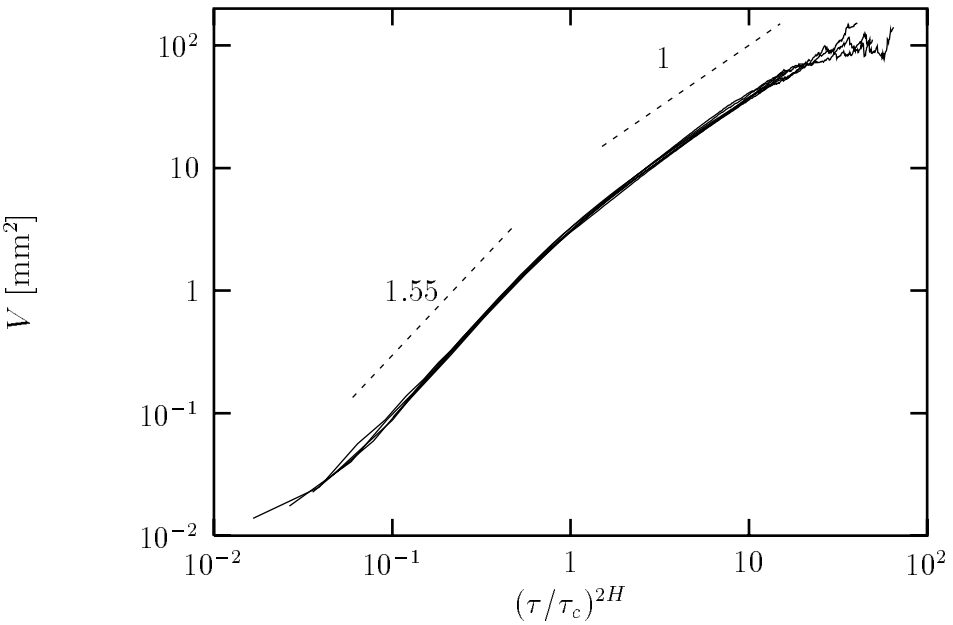

Figure 4.4: Self-diffusion. Collapse of the variance curves of Fig. 4.2 into one scaling function, by a rescaling of the time interval τ.

$(\tau/\tau_c(\epsilon))^{2H(\epsilon)}$, and thus removed the ϵ-dependence. The resulting excellent data collapse of the variance is shown in Fig. 4.4; it shows that the variance is an ϵ-independent function of the rescaled time $V = f(\tilde{\tau})$. The scaling function f reflects the cross-over in the dynamical behavior at $f(1) = \lambda^2/2$. We have $f(\tilde{\tau}) \sim \tilde{\tau}^{\gamma}$ below the cross over, and $f(\tilde{\tau}) \sim \tilde{\tau}$ above.

Next, we plot the variance V for various values of ϵ versus the variance for a particular ϵ value, using the reduced time $\tau/\tau_c(\epsilon)$ as the parameter. Note that this is *not* an 'extended self-similarity' plot in the sense of Chapter 2, because it is not a plot of higher order moments versus a lower order moment at a fixed value of ϵ. Rather it is a plot only of second order moments for various values of ϵ.

However, such a plot still serves to remove some common structure of the curves, in this case the cross-over, in order to study the nature of the curves separated from the mentioned structure. Here, we want to study the deviation from Brownian motion by attempting to remove the cross-over. We have chosen $\epsilon = 1.06$ as the reference; see Fig. 4.5. We see that there is no sign of the cross-over in each curve, all curves are straight lines with slope $2H(\epsilon)$ [because $2H(\epsilon = 1.06) = 1$].

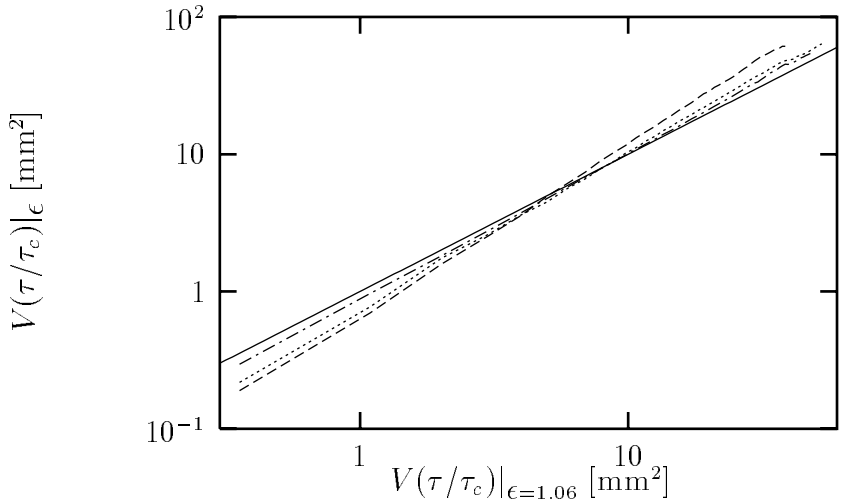

Figure 4.5: Self-diffusion. The variance V for $\epsilon = 0.05$ (dashed line), $\epsilon = 0.24$ (dotted line), and $\epsilon = 0.65$ (dash-dotted line), plotted versus the variance for $\epsilon = 1.06$, using the reduced time $\tau/\tau_c(\epsilon)$ as the parameter. For comparison, a line of slope 1 is shown (unbroken line).

We note that even though the ocean waves and the waves in our laboratory experiment are maintained by different mechanisms, we nevertheless see a similar behavior of the tracers in the two systems. Below a certain length scale, which is $\sim$ 100 km for oceanographic measurements and 2.6 mm for our capillary waves, the motion is far from Brownian and the variance of x grows with time with an exponent ≈ 1.5. Above that length scale, the motion is much closer to being Brownian.

4.3 Fractional Brownian Motion

For Brownian motion, the variance of the particle displacement grows linearly with time and defines a diffusion coefficient D from $V(\tau) = 2D\tau$. However, as we see in our experiment, the motion of the particles does not always follow Brownian motion. One defines a time-dependent diffusion coefficient $D(\tau) = A\tau^{2H-1}$ with $0 < H < 1$, to describe the particle self diffusion.

Such behavior may be described by *fractional Brownian motion* (fBm), a generalization of ordinary Brownian motion [44, 43, 45]. In ordinary Brownian motion (without mean drift) the displacement $\Delta x(\tau)$ has a Gaussian distribution, $P(\eta) \sim \exp(-\eta^2)$, with $\eta = \Delta x(\tau)/\tau^{1/2}$. For fractional Brownian motion,

the Gaussian-distributed quantity is $\eta' = \Delta x(\tau)/\tau^H$, where $H \neq 1/2$. This introduces correlations whose extensions in time are infinite, as we shall see below.

For ordinary Brownian motion, two successive displacements $x(t) - x(t-\tau_1)$ and $x(t+\tau_2) - x(t)$ are independent, but for fractional Brownian motion this is not so. The correlation between two successive displacements is

$$\begin{aligned} C(\tau_1,\tau_2) &= \frac{\langle [x(t)-x(t-\tau_1)]\,[x(t+\tau_2)-x(t)]\rangle}{\langle [\Delta x(\tau_1)]^2\rangle^{1/2}\,\langle [\Delta x(\tau_2)]^2\rangle^{1/2}} \\ &= \frac{\langle [x(t)-x(t-\tau_1)]\,[x(t+\tau_2)-x(t)]\rangle}{2A(\tau_1\tau_2)^H} \\ &= \frac{1}{4A(\tau_1\tau_2)^H}\Big\{\langle [x(t+\tau_2)-x(t-\tau_1)]^2\rangle \\ &\qquad - \langle [x(t+\tau_2)-x(t)]^2\rangle - \langle [x(t)-x(t-\tau_1)]^2\rangle\Big\} \\ &= \frac{(\tau_1+\tau_2)^{2H}-\tau_1^{2H}-\tau_2^{2H}}{2(\tau_1\tau_2)^H}\,. \end{aligned} \tag{4.8}$$

For $\tau_1 = \tau_2 = \Delta t$, we have $C(\tau_1,\tau_2) = 2^{2H-1} - 1$, which is non-zero for $H \neq 1/2$ and is independent of the size of the time interval Δt considered. The sign of $C(\Delta t, \Delta t)$ changes according to whether $H < 1/2$ (C negative) or $H > 1/2$ (C positive). Hence if $H < 1/2$, a positive displacement is likely to be followed by a negative displacement (this is called 'anti-persistence'), whereas $H > 1/2$ implies that a positive displacement is likely to be followed by another positive displacement ('persistence').

Using the correlator for successive separations, Eq. (4.8), we compute the correlation between two displacements that are separated in time by $T \gg \tau$,

$$\begin{aligned} C_T(\tau,\tau) &= \frac{\langle [x(t+\tau)-x(t)]\,[x(t+T+\tau)-x(t+T)]\rangle}{\langle \Delta x(\tau)^2\rangle} \\ &= \frac{1}{2A\tau^{2H}}\{-\langle [x(t+T)-x(t+\tau)][x(t+T+\tau)-x(t+T)]\rangle \\ &\qquad + \langle [x(t+T)-x(t)][x(t+T+\tau)-x(t+T)]\rangle\} \\ &= \frac{1}{2}\left(\frac{T}{\tau}\right)^{2H}\left\{-2+\left(1-\frac{\tau}{T}\right)^{2H}+\left(1+\frac{\tau}{T}\right)^{2H}\right\} \\ &\simeq H(2H-1)\left(\frac{T}{\tau}\right)^{2H-2} \end{aligned} \tag{4.9}$$

For $H = 1/2$ the correlation is zero for any separation in time $T > 0$. For other values of H (within $0 < H < 1$) the correlation is non-zero for finite T/τ and only vanishes as $T/\tau \to \infty$. Consequently, the size of one displacement depends on any previous displacement a time T away, except — of course — for ordinary Brownian motion. As found for successive displacements, the sign of the time separated correlator C_T changes according to whether $H < 1/2$ or $H > 1/2$ for displacements that are separated in time. Thus a positive displacement in the past will make it more likely that the present displacement will be negative, resp. positive, the likelihood being weighed by the factor $(T/\tau)^{2H-2}$. The factor $(T/\tau)^{2H-2}$ decreases with separation in time, making less recent displacements less important, but not unimportant.

Numerically implementing motion with correlations between time-separated displacements is problematic for large time separations. A simple scheme for modeling fractional Brownian motion is described in Ref. [45, Chap. 9]. In this scheme, a time step is associated with a Gaussian distributed variable, and a displacement is influenced by the previous M displacements via an average over the M Gaussian distributed variables, weighed by a factor that decreases with the time separation T, the factor being $(T/\Delta t)^{H-1/2} - (T/\Delta t - 1)^{H-1/2}$. For time separations T larger than $M\,\Delta t$ the displacements become uncorrelated. We utilize this scheme to model a fBm with a cut-off time at $T = M\,\Delta t$. On time scales smaller than $M\,\Delta t$ the motion is fractional Brownian, but on time scales larger than $M\,\Delta t$ the motion crosses over to ordinary Brownian. Figure 4.6 shows the variance for at numerically modeled fBm with exponent $H = 0.8$ and a 'memory' time limit of $T/\Delta t = 600$. As we would expect, the double-logarithmic curve crosses over from a fBm behavior with slope $2H = 1.6$ to the ordinary Brownian motion slope 1 at $T/\Delta t \simeq 600$.

This resembles the behavior of the scaling function $f(\tilde{\tau})$, compare Figures 4.4 and 4.6. It suggests that the diffusion may be modeled by a convolution of two fractional Brownian motions:

(i) An ϵ-independent motion that has a cut-off near the time scale $\tau(\epsilon)$ (which corresponds to the length scale λ, therefore the cut-off is also ϵ-independent). This fBm has exponent $H_\lambda = 1.55/2$, and is represented by the scaling function $f(\tilde{\tau})$.

(ii) An ϵ-dependent motion, featured in Fig. 4.5, that does not have any cut-off below the scale of the system size. This fBm has exponent H varying from 0.5 at $\epsilon = 1.06$ to 0.63 at $\epsilon = 0.05$, the exponents shown in Table 4.1.

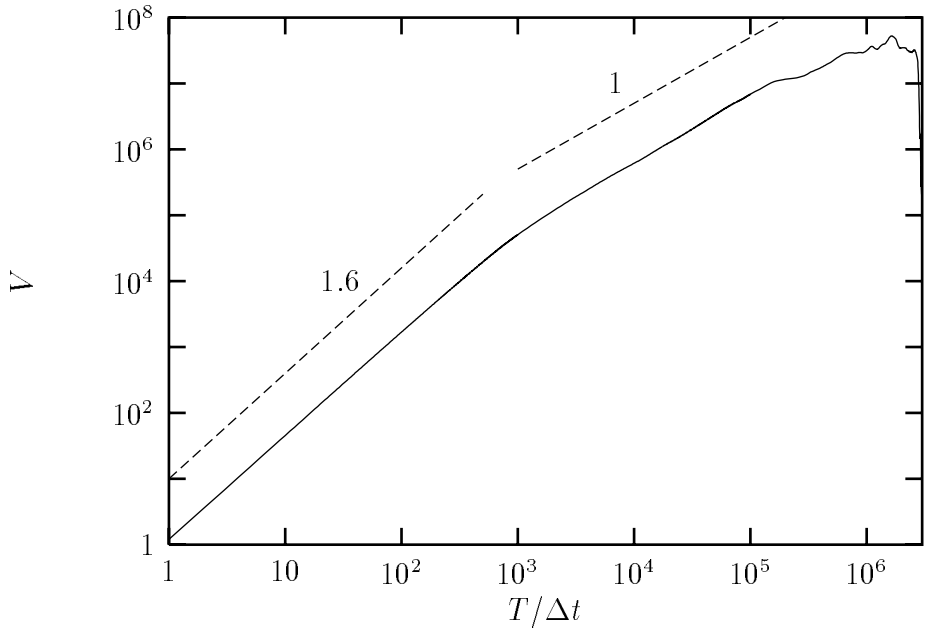

Figure 4.6: Simulation of a fractional Brownian motion with at cut-off time at $T/\Delta t = 600$.

In physical terms, the former may result from turbulent eddies of size less than the wavelength, while the latter results from turbulent eddies of all sizes less than the system size, here with the term 'eddy' used as in Chapter 1.

As a digression, I mention that another type of 'memory' cut-off for fBm has been introduced, see e.g. Ref. [46]. The fBm power spectrum $S(\omega) \sim \omega^{-(2H+1)}$, where ω is the frequency, is modified by adding a cut-off a such that

$$S(\omega) \sim (a^2 + \omega^2)^{-(H+1/2)} \ . \tag{4.10}$$

When Fourier transforming (4.10) back into t-space the correlations will decay as $\exp(-at)$ for large t. The cut-off preserves correlations at time scales $t \ll 1/a$ and removes correlations at time scales $t \gg 1/a$.

4.4 Fractal Dimension of Trajectories

As another way to analyse the particle trajectories we determined the fractal dimension of the particle trajectories using the 'yardstick' method [43]. The exponent H for fractional Brownian motion is related to the fractal dimension as

we shall see below. Here, however, we find the fractal dimension directly from the trajectories.

The trajectories were defined by a linear interpolation between successive data points, and all trajectories of each control parameter ϵ were translated such as to obtain one long trajectory.

The length of the trajectory was measured at different length scales ℓ, by counting the number $N(\ell)$ of sticks of length ℓ needed. The fractal dimension $\mathcal{D}$ is formally defined by [43]

$$\mathcal{D} = \lim_{\ell \to 0} \frac{\ln N(\ell)}{\ln(1/\ell)} \tag{4.11}$$

which implies that $N(\ell) \sim \ell^{-\mathcal{D}}$. For fractional Brownian motion the fractal dimension is $\mathcal{D} = \min\{1/H, d\}$ where d is the dimension in which the fBm takes place.

We note that for finding the fractal dimension we consider the trajectories in their full two-dimensional form, whereas in the previous sections, including the Section 4.3 on fBm, we considered the projection of the horizontal motion onto one direction. Assuming that the projections onto the two orthogonal directions x and y are independent, the fBm arguments carry through with the variance $\langle \Delta x(\tau)^2 + \Delta y(\tau)^2 \rangle = 4D(\tau)\tau$ and $D(\tau) = A\tau^{2H-1}$. For persistent ($0.5 < H < 1$) fBm we therefore expect $\mathcal{D} = 1/H$, and $\mathcal{D} = 2$ for ordinary Brownian motion.

Fig. 4.7 reports $N(\ell)$, normalized by the number of sticks used at length scale λ, versus the length scale ratio ℓ/λ. Like the variance curves, also the $N(\ell)$ curves can be collapsed by a rescaling $\ell \to \tilde{\ell} = \ell^{\mathcal{D}(\epsilon)/2}$ to obtain an ϵ-independent curve; see the inset of Fig. 2 in Paper V. The curve crosses over from a power $\mathcal{D}_\lambda = 1.30 \pm 0.05$ to $\mathcal{D} = 2$, ordinary Brownian motion behavior. The fractal dimension $\mathcal{D}(\epsilon)$ is obtained from the rescaling of the individual curves, and is given in Table 4.1. The $\mathcal{D}(\epsilon)$ found is in good agreement with the estimate $1/H(\epsilon)$, and so is $\mathcal{D}_\lambda = 1/H_\lambda$. We also note that for the oceanographic measurements cited in the introduction to this chapter the fractal dimension is also ~ 1.3, and the relation $\mathcal{D} = 1/H$ also holds for those measurements.

There are other tools for analyzing particle trajectories than those considered here. Several of these are employed in Ref. [10], e.g. the power spectra of the trajectories, the roughness of the trajectories, and the correlations (4.8) of past and future displacements. Also trapping times and flight times of the particles can be studied. Each of the tools highlights a certain aspect of the motion. We chose to concentrate on the mean square displacement and on the fractal

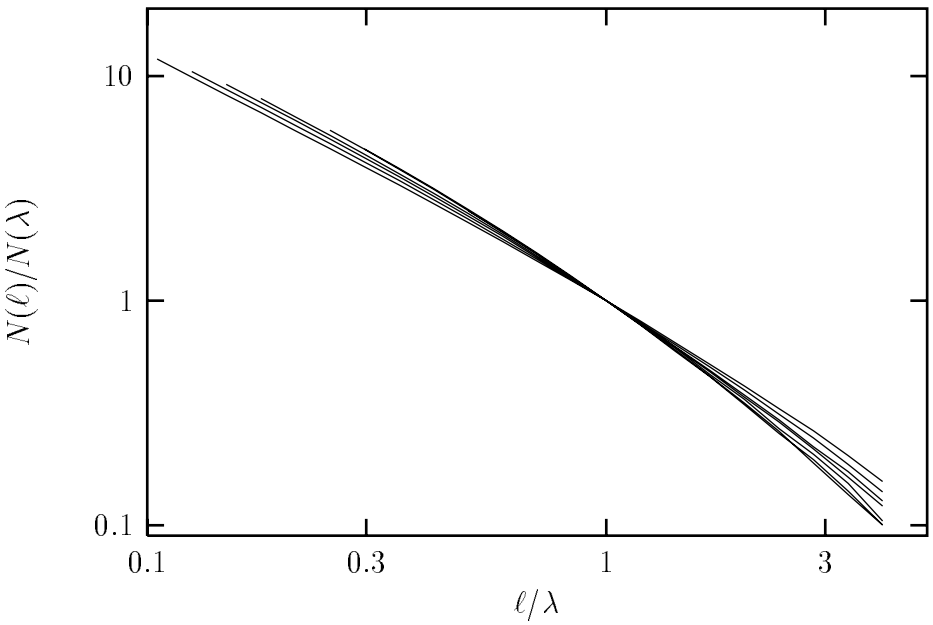

Figure 4.7: Self-diffusion. The number $N(\ell)$ of yardsticks needed to measure the particle trajectories on scale ℓ, normalized to the number used at $\ell = \lambda$, and with the scale ℓ measured in units of the wavelength λ. The curves show $N(\ell)$ for $\epsilon = 0.05$, 0.13, 0.24, 0.34, 0.65, 0.86, and 1.06 (steepest curve).

dimension of the trajectory.

On a final note, one may wonder why we did not notice any change in the behavior of the relative diffusion around the particle separation $R \approx \lambda$. But this is easily understandable — when computing the relative moments as functions of the separation R we collected the measurements in bins $[R - \eta, R + \eta[$ with $\eta = 0.5$ mm. We therefore only have two bins below the wavelength $\lambda = 2.6$ mm, at $R = 1 \pm 0.5$ mm and at 2 ± 0.5 mm. In combination with the relatively small number of measurements in each bin (~ 3000; see Fig. 2.1), this is hardly enough to see any change in behavior. A finer bin partition at small R scales would result in more points below the scale λ, but it would also increase the statistical error. Thus from our relative diffusion data we can neither confirm nor exclude the possibility that the behavior of the relative motion changes around the length scale λ.

Chapter 5

The Complex Ginzburg-Landau Equation

The theme of the following two chapters is the extensively studied [47, 48, 49, 50, 51, 52] Ginzburg-Landau equation with complex coefficients. It derives as an amplitude equation of a reaction-diffusion system at and right after a bifurcation from a steady state into a stable, periodic orbit (a Hopf bifurcation) [48]. It is also studied in its own right as a simple, yet very interesting spatially extended oscillatory system.

This chapter is a short introduction to the equation. The equation has become a field of study in itself, and here I will merely mention some of its main characteristics. Towards the end of the chapter I describe a numerical simulation of particles moving in a complex Ginzburg-Landau field. The results were reported in Paper II. The next chapter is concerned with the derivation of an equation of motion for vortices in two- and three-dimensional systems modeled by the complex Ginzburg-Landau equation. These results are reported in Paper IV.

5.1 Introduction

The Complex Ginzburg-Landau (CGL) equation is given by the following expression

$$\frac{d}{dt}A = P(A, A^*)A + b\nabla^2 A \tag{5.1}$$

where $A = |A|\exp(iS)$ is a complex field and the function P is given by $P(A, A^*) = \mu - a|A|^2$. The coefficients a, b, and μ are complex numbers. In two-dimensional systems the equation supports traveling plane wave solutions [48, 50]

$$A = F\exp(i\boldsymbol{k}\cdot\boldsymbol{r} - i\omega t) \tag{5.2}$$

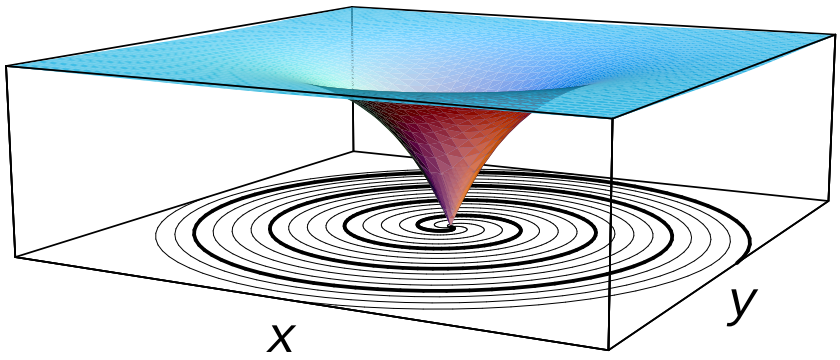

Figure 5.1: One-armed spiral vortex of the CGL field $A = |A|e^{iS}$ in a two-dimensional system. The height of the surface depicts the amplitude $|A|$. The spiraling curves are contour lines of the phase S (isophase lines). The phase change between two thin lines is $\pi/2$.

for which the squared amplitude is $F^2 = (\mu_R - b_R k^2)/a_R$ and the frequency

$$\omega = \frac{a_I}{a_R}(\mu_R - b_R k^2) + b_I k^2 - \mu_I \tag{5.3}$$

where $a_R \equiv \mathrm{Re}(a)$, $a_I \equiv \mathrm{Im}(a)$, etc. The permitted wave numbers satisfy the relation $\{\mu_R - b_R k^2\}/a_R > 0$. The homogeneous solution $A = F\exp(-i\omega t)$ is a special case of (5.2).

Equation (5.1) also permits solutions in which A has phase singularities (*defects*). In two space dimensions these are isolated points around which the phase S changes by multiples of 2π. At these points the amplitude $|A|$ vanishes, so that the complex field A remains single valued; see Figure 5.1. In the vicinity of an isolated defect the phase is of the form [53, 50, 48]

$$S = \psi(r) + n\varphi - \omega t \tag{5.4}$$

in polar coordinates (r, φ), where n is an integer. For a fixed phase S this is the equation for $|n|$-armed spirals rotating at an angular frequency ω/n where

$$\omega = \frac{a_I}{a_R}(\mu_R - b_R k_\infty^2) + b_I k_\infty^2 - \mu_I \tag{5.5}$$

provided that the coefficient of the real part of the nonlinearity a_R does not vanish. Far from the vortex center the spiral approaches the form of a plane wave with wave number $k_\infty \equiv \lim_{r\to\infty} \psi'(r)$ and $\lim_{r\to\infty} |A| = \sqrt{(\mu_R - b_R k_\infty^2)/a_R}$. The asymptotic wavenumber k_∞ of the spiral satisfies $\{\mu_R - b_R k_\infty^2\}/a_R > 0$. It is uniquely determined by the coefficients a, b, and μ but an analytic expression has not been found.

Close to the defect, the radial dependence of the phase field may be approximated by the expansion

$$\psi(r) = d_2 r^2 + d_4 r^4 + \ldots \tag{5.6}$$

and the radial dependence of the amplitude

$$|A(r)| = g_0 r^{|n|} + g_2 r^{|n|+2} + \ldots \tag{5.7}$$

By inserting these expansions into a polar coordinates version of (5.1) the coefficients of (5.6) may be found, the first of which is

$$d_2 = \frac{-(\omega + \mu_I) b_R + \mu_R b_I}{4(|n|+1)|b|^2} = \frac{(b_I - a_I/a_R)(\mu_R - b_R k_\infty^2)}{4(|n|+1)|b|^2} \tag{5.8}$$

where the last equality requires that $a_R \neq 0$.

In three spatial dimensions the defects become one-dimensional strings, or *filaments*, and the spirals generalize to scroll waves [54, 55] which look like sheets wound around a filament. The filaments may be closed or open (in which case they end on the system boundary) and of arbitrary shape. A filament is a connected string of zeros of the field A.

The integer n is the winding number (vorticity) of the vortex. In two space dimensions, the sum of the winding numbers of the vortices in the system (or more generally, the total phase gradient) is a constant, which depends on the genus g ('number of handles') of the two-dimensional surface as $2(1-g)$ (from the Gauss-Poincaré's theorem). The vortices are created and annihilated in pairs of opposite winding number, thereby conserving the total winding number. We use periodic boundaries in the numerical simulations, in that case obviously $g = 1$ and the total winding number is zero. Note that some authors use the term 'winding number' for the total winding number of the system [56].

Vortices of winding number $|n| > 1$ are unstable and break down into n vortices, each with a winding number $\mathrm{sign}(n)$ [53, 57]. The *core* of the vortex is the region where the amplitude $|A|$ deviates significantly from its asymptotic value; see Figure 5.1.

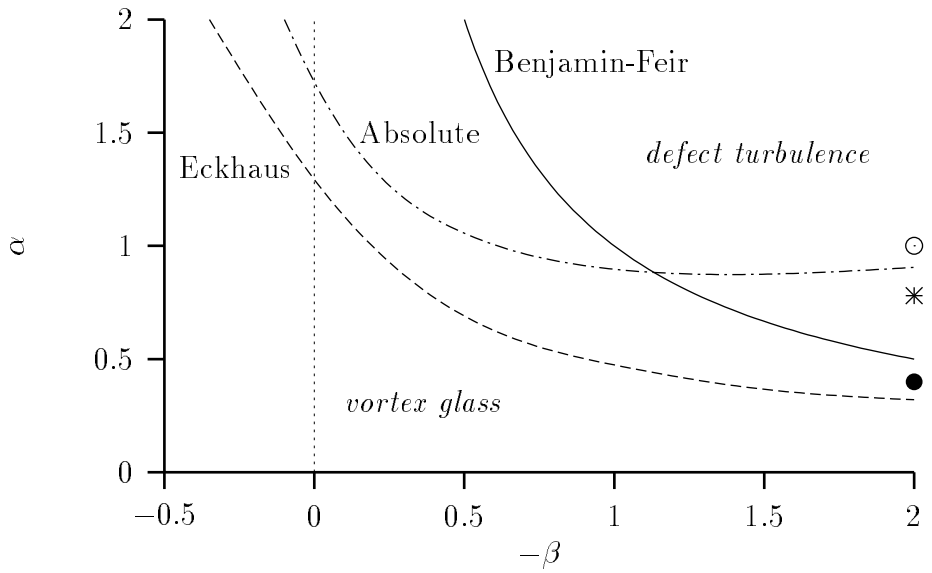

Figure 5.2: The phase diagram for the two-dimensional CGL equation for $\alpha > 0$. The vortices have a Benjamin-Feir (/Absolute/convective) instability above the Benjamin-Feir (/Absolute/Eckhaus) instability line. The filled and the open circle are the parameter values used in Fig. 5.3. The star is the set of parameters used for Fig. 5.9. The Eckhaus instability line and the absolute instability line are adapted from Ref. [50].

The CGL equation encompasses a number of interesting special cases. When a, b, and μ are purely imaginary, the CGL equation coincides with the nonlinear Schrödinger equation. The latter equation is a model for type-II superconductors when substituting the gradient in Eq. (5.1) by $\nabla + 2ie\boldsymbol{A}/(\hbar c)$ [58, 59]. There, $\boldsymbol{A}$ is the vector potential, $2e$ is the charge of a Cooper pair, and $|A|^2$ is the local density of the superconducting electrons.

The nonlinear Schrödinger equation also describes the quantum dynamics of superfluid ^{4}He and is known in that context as the Ginzburg-Pitaevskii-Gross equation (GPG) [60]. The vortex solution of the GPG equation describes the circulation of the superfluid around strings of normal-phase fluid. $|A|^2$ corresponds to the superfluid mass density and the phase gradient ∇S is proportional to the velocity of the superfluid.

Furthermore, by employing the Madelung transformation [61] the nonlinear Schrödinger equation transforms into the hydrodynamic equations for an inviscid and incompressible fluid (the Euler equations). To see this, consider the CGL

equation (5.1) with imaginary coefficients

$$\frac{d}{dt}A = i\tilde{P}(|A|^2)A + ib_I\nabla^2 A \tag{5.9}$$

where the function $\tilde{P}$ takes on real values, e.g. $\tilde{P}(|A|^2) = \mu_I - a_I|A|^2$. The real and imaginary parts of Eq. (5.9) lead to

$$\frac{d|A|^2}{dt} = -2b_I\nabla\cdot(|A|^2\nabla S) \tag{5.10}$$

$$\frac{dS}{dt} = \tilde{P}(|A|^2) + b_I\frac{\nabla^2|A|}{|A|} - b_I(\nabla S)^2 \ . \tag{5.11}$$

For fluids that are vorticity-free except at isolated points one may introduce a flow potential such that the fluid velocity is the gradient of the potential. When we choose the flow potential $2b_I S$, i.e. the fluid velocity $\boldsymbol{v} = 2b_I\nabla S$, and the mass density $\rho = |A|^2$ we find that Eq. (5.10) corresponds to the continuity equation for the flow

$$\frac{d\rho}{dt} = -\nabla(\rho\boldsymbol{v}) \ . \tag{5.12}$$

Note that the time derivative d/dt is taken at a fixed point in space, it is not the substantial derivative $D/Dt = d/dt + \boldsymbol{v}\cdot\nabla$ at a (material) point that moves along with the fluid at velocity $\boldsymbol{v}$. The Euler equation with an applied forcing $\boldsymbol{f}$ and a pressure p is

$$\frac{d\boldsymbol{v}}{dt} + \frac{1}{2}\nabla(v^2) = -\frac{\nabla p}{\rho} + \boldsymbol{f} \ . \tag{5.13}$$

For a conservative force $\boldsymbol{f} = -\nabla U$ the equation can be rewritten in terms of the flow potential $2b_I S$

$$2b_I\frac{dS}{dt} + \frac{1}{2}(2b_I\nabla S)^2 = -\int\frac{dp}{\rho} - U \ . \tag{5.14}$$

Taking

$$\int\frac{dp}{\rho} + U = -2b_I\tilde{P}(\rho) - 2b_I^2\frac{\nabla^2\sqrt{\rho}}{\sqrt{\rho}} \tag{5.15}$$

the fluid equations are thus connected to the nonlinear Schrödinger equation. However, there is one important difference between the nonlinear Schrödinger equation and fluids: the vorticity (winding number) of the vortices in the nonlinear Schrödinger equation is quantized (integer), whereas the vorticity of fluid vortices can take on any value.

For purely real coefficients a, b, and μ the CGL equation reduces to the nonlinear heat equation, and with a real field $A = A^*$ to the 'Landau-Ginzburg' equation of phase transitions.

It is easily confirmed that the number of real adjustable parameters in the coefficients of Eq. (5.1) may be brought down to two by the following rescaling of time t, space $\boldsymbol{r}$, and the complex field A

$$t \to \tilde{t} = \mu_R\, t \qquad \boldsymbol{r} \to \tilde{\boldsymbol{r}} = \sqrt{\frac{\mu_R}{b_R}}\,\boldsymbol{r} \qquad A \to \tilde{A} = \sqrt{\frac{a_R}{\mu_R}}\,\exp(-i\mu_I t)\,A \tag{5.16}$$

whereby Eq. (5.1) may be written

$$\frac{d}{d\tilde{t}}\,\tilde{A} = \tilde{A} - (1+i\alpha)|\tilde{A}|^2\tilde{A} + (1+i\beta)\nabla^2_{\tilde{r}}\tilde{A} \tag{5.17}$$

with the coefficients $\alpha = a_I/a_R$ and $\beta = b_I/b_R$. In the rescaled coordinates, the frequency of rotation is $\omega = \beta k_\infty^2 + \alpha(1-k_\infty^2)$ and the coefficient of the lowest order term in $\psi(r)$ is

$$d_2 = \frac{-\omega+\beta}{4(|n|+1)(1+\beta^2)} = \frac{(\beta-\alpha)(1-k_\infty^2)}{4(|n|+1)(1+\beta^2)}\ . \tag{5.18}$$

The asymptotic wavenumber is limited by $k_\infty^2 < 1$ and depends on α and β only. By a complex conjugation of Eq. (5.17) we see that studying the field A and parameters (α,β) corresponds to studying A^* and parameters $(-\alpha,-\beta)$. Due to this symmetry, it is therefore sufficient to study the Eq. (5.17) in e.g. the parameter range $\alpha > 0$.

5.1.1 Stability

The spiral vortices and the traveling plane-waves are not stable for all values of α and β. Discussions of the stability are given in e.g. Refs. [47, 50, 52]. Here only a short resume will be given.

To study the stability of the traveling plane waves, we add a perturbation σ to the traveling plane-wave solutions of Eq. (5.17) $A = (F+\sigma)\exp(i\boldsymbol{k}\cdot\boldsymbol{r} - i\omega t)$. We restrict the analysis to longitudinal perturbations

$$\sigma = \sigma_+(t)\,e^{i\boldsymbol{q}\cdot\boldsymbol{r}} + \sigma_-(t)\,e^{-i\boldsymbol{q}\cdot\boldsymbol{r}} \tag{5.19}$$

where $\boldsymbol{q}||\boldsymbol{k}$. By inserting the perturbed solution into the CGL equation (5.17) and keeping terms to linear order in σ, a linear system of differential equations is obtained

$$\partial_t \begin{pmatrix} \sigma_+ \\ \sigma_-^* \end{pmatrix} = L \begin{pmatrix} \sigma_+ \\ \sigma_-^* \end{pmatrix} \tag{5.20}$$

with the matrix

$$L = \begin{pmatrix} -(1+i\alpha)F^2 + (1+i\beta)(-2\boldsymbol{k}\cdot\boldsymbol{q} - q^2) & -(1+i\alpha)F^2 \\ -(1-i\alpha)F^2 & -(1-i\alpha)F^2 + (1-i\beta)(2\boldsymbol{k}\cdot\boldsymbol{q} - q^2) \end{pmatrix} \tag{5.21}$$

For small $q = |\boldsymbol{q}|$ the eigenvalue with the largest real part is

$$\lambda(q) = ivq - D_{||}\, q^2 + \mathcal{O}(q^3) \tag{5.22}$$

where $v = 2(\alpha - \beta)k$ and $D_{||} = 1 + \alpha\beta - 2(1+\alpha^2)k^2/(1-k^2)$. The linear analysis therefore predicts that the traveling plane waves may become unstable if their wavenumber k is such that $D_{||}(k) < 0$. We see that the homogeneous solution $A = F\exp(-i\omega t)$ thus is stable in the range of parameters (α, β) for which $D_{||}(0) = 1 + \alpha\beta > 0$. The line $1 + \alpha\beta$ is called the Benjamin-Feir line (see Figure 5.2).

The spiral vortices approach plane waves with wavenumber k_∞ far from their center, so this analysis should also apply reasonably well to the vortices. The wavenumber k_∞ is determined by the values of α and β. The analysis thus divides the $\alpha - \beta$ parameter plane by the lines $D_{||}[k_\infty(\alpha,\beta), \alpha, \beta] = 0$ into regions where vortices are (Eckhaus) unstable and a region where the vortices are (Eckhaus) stable; see Fig. 5.2 where only the upper half plane is shown. The vortices are Eckhaus unstable above the 'Eckhaus' line in Fig. 5.2, which is where $D_{||}[k_\infty(\alpha,\beta), \alpha, \beta] = 0$.

However, the spirals emit waves with the group velocity

$$\frac{\partial\omega}{\partial k_\infty} = \frac{\partial}{\partial k_\infty}(\alpha + (\beta - \alpha)k_\infty^2) = 2(\alpha - \beta)k_\infty = v(k_\infty)\ . \tag{5.23}$$

Thus the perturbation drifts away, and the vortex may be absolutely stable, even though it was found to be convectively (Eckhaus) unstable. The wavenumbers k'_∞ for which the drift v is not enough to transport the perturbation away are the wavenumbers at which the perturbations make the spiral vortices break down. Again taking notice of the fact that the values of α and β determine the asymptotic wavenumber $k_\infty(\alpha,\beta)$, this leads to a line in the $\alpha-\beta$ parameter half-plane below which spiral vortices are (absolutely) stable, and unstable above, see Fig. 5.2.

When the vortices are stable, i.e. below the line in Fig. 5.2 termed 'Absolute', they organize in a cell structure with the spiral vortices at the centers of the cells,

and with shock lines in the amplitude $|A|$ at the border to the neighboring spiral vortices; see the right panel in Fig. 5.3. There may also be vortices ($|A| = 0$) at the intersections of the shocks, so-called 'edge vortices'. Whereas the overall structure of the system is fixed, the edge vortices are not totally fixed. It is not clear whether the edge vortices are very slowly relaxing to a fixed state. For this reason this regime in the $\alpha - \beta$ plane is called a *vortex glass*. Above the line 'Absolute', the defects have little or no spiral structure in the phase S; see the left panel of Fig. 5.3. The defects move around and are created and annihilated pairwise. This region of the $\alpha - \beta$ plane is called *defect turbulence*. The density of defects is much larger in the defect turbulent regime than in the vortex glass regime even for close values of α and β.

5.2 Numerical Simulations

In order to study the Complex Ginzburg-Landau equation (5.17) numerically, we simulated the equation on a coupled map lattice [62]. This is an often used method for simulating the CGL equation, another being the pseudo-spectral Fourier method. We consider the equation in two space dimensions with discrete time variables on a two-dimensional square-lattice (i.e. the spatial variables are also discretized), and the field A is allowed to take on a continuum of values. The integration is split into two mappings, a nonlocal map that integrates the nonlocal part of the CGL equation (5.17)

$$\frac{dA}{dt} = (1 + i\beta)\nabla^2 A \tag{5.24}$$

(henceforth the tildes in Eq. (5.17) are omitted) and a local map

$$\frac{dA}{dt} = A - (1 + i\alpha)|A|^2 A \ . \tag{5.25}$$

The local and nonlocal parts are integrated separately and with different time steps [63]. Let τ_0 denote the nonlocal time steps, τ the local time steps, and their ratio $\nu \equiv \tau_0/\tau (< 1)$. Integrating the two parts with different time steps is equivalent [63] to rescaling $A \to \check{A} = \sqrt{\nu}\, A$ and changing the local part (5.25) to

$$\frac{d\check{A}}{dt} = \nu\check{A} - (1 + i\alpha)|\check{A}|^2\check{A} \tag{5.26}$$

which, by considering the real and imaginary part, can be written in terms of the amplitude $|\check{A}|$ and the phase S of $\check{A}$

$$\frac{d}{dt}|\check{A}| \ = \ \nu|\check{A}| - |\check{A}|^3 \tag{5.27}$$

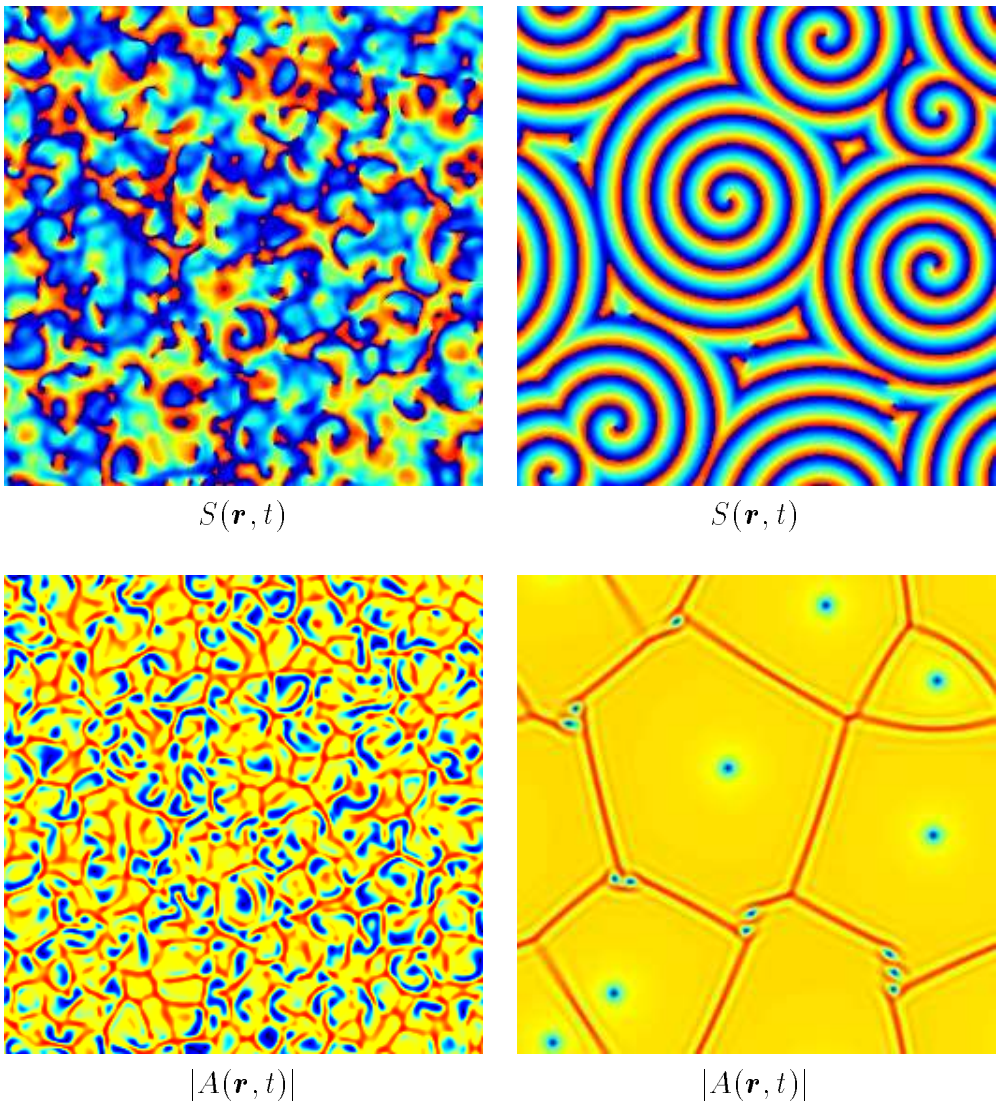

Figure 5.3: The CGL equation. The left panel shows a snapshot the phase $S(\boldsymbol{r},t)$ (top) and the amplitude $|A(\boldsymbol{r},t)|$ (bottom) at the parameter values $(\alpha,\beta) = (1,-2)$. The right panel shows the glassy regime at parameter values $(\alpha,\beta) = (0.4,-2)$. The color coding for $S(\boldsymbol{r},t)$ goes from red ($S \approx 0$) via green ($S \approx \pi$) to blue ($S \approx 2\pi$). For $|A(\boldsymbol{r},t)|$ the color coding goes from blue for $|A| = 0$ to red for $|A| = |A|_{max}$.

$$\frac{d}{dt}S = -\alpha|\check{A}|^2 \ . \tag{5.28}$$

In practice we usually choose the local time step τ to be five times the nonlocal time step τ_0; $\nu = 0.2$.

The solution to the non-local map (5.24)

$$\begin{aligned} \check{A}(\boldsymbol{r}, t+\tau_0) &= \exp\{\tau_0(1+i\beta)\nabla^2\}\check{A}(\boldsymbol{r}, t) \\ &\approx \left[1 + \frac{\tau_0}{m}(1+i\beta)\nabla^2\right]^m \check{A}(\boldsymbol{r}, t) \end{aligned} \tag{5.29}$$

is discretized by using a linear interpolation at the four nearest neighbor sites for the Laplacian [63]

$$\nabla^2\check{A}(\boldsymbol{r}, t) \approx \frac{1}{4}\sum_{\text{n.n.}}\{\check{A}(\boldsymbol{r}_{\text{n.n.}}, t) - \check{A}(\boldsymbol{r}, t)\} \tag{5.30}$$

where n.n. means 'nearest neighbor sites'. Taking $m = 5$ has proven sufficient. In some of the numerical simulations we improved the approximation (5.30) by including the four next-nearest neighbor sites, but it did not seem to influence the performance of the program.

We find the solution to the local part by straightforward integrations, first of Eq. (5.27), and then of Eq. (5.28) with the solution to (5.27) inserted. The result is

$$|\check{A}(\boldsymbol{r}, t+\tau)| = \frac{\sqrt{\nu}\,|\check{A}(\boldsymbol{r}, t)|}{\sqrt{\lambda(\tau)\nu + \{1-\lambda(\tau)\}|\check{A}(\boldsymbol{r}, t)|^2}} \tag{5.31}$$

$$S(\boldsymbol{r}, t+\tau) = S(\boldsymbol{r}, t) - \frac{\alpha}{2}\ln\left\{1 + \frac{1-\lambda(\tau)}{\nu\lambda(\tau)}|\check{A}(\boldsymbol{r}, t)|^2\right\} \tag{5.32}$$

where $\lambda(\tau) \equiv \exp(-2\nu\tau)$; see also Ref. [64]. By inserting the numerical values of the nonlocal solution (5.29) into the local solution (5.32) the system is advanced one (local-part) time step τ.

The simulations were performed on square lattices with 128×128 to 512×512 sites and with a fixed time step ratio $\nu = 0.2$. The boundary conditions are periodic. When defects are present in the system, we usually normalize the *output* numerical value of $|A|$ (not the value of $|A|$ within the program) such that the maximum value at the lattice, at a given time, is $|A| = 1$ (and the minimum value is zero). Hence it is not important to keep track of the various rescalings of A. In most cases we use random initial conditions with A chosen at random within the unit circle. The numerical simulations were performed at a Connection Machine-2 (Uni-C, Denmark) and at a workstation.

5.3 Diffusion in the CGL Equation

In Paper II we studied particle motion in the background of defect turbulence. Previous studies have considered the motion of a scalar field in the one- and two-dimensional Kuramoto-Sivashinsky equation [65, 66]. We studied the background defect turbulence described by the complex Ginzburg-Landau equation (5.17)

$$\frac{d}{dt}A = A - (1+i\alpha)|A|^2 A + (1+i\beta)\nabla^2 A \tag{5.33}$$

(where I again omitted the tildes). We defined the particle velocity as proportional to the gradient of the phase of A

$$\boldsymbol{v} = \frac{d\boldsymbol{r}}{dt} = \Gamma \nabla S(\boldsymbol{r}, t) \tag{5.34}$$

where $\boldsymbol{r}(t) = re^{i\varphi}$ is the particle position. The coefficient $\Gamma \in \boldsymbol{R}$ is an adjustable parameter. Γ can be interpreted as a mobility parameter because it is the coefficient relating the field ∇S to the 'drift' velocity $\boldsymbol{v}$. In the GPG (nonlinear Schrödinger) equation the velocity (5.34) with $\Gamma = 2b_I$ would be an approximation of the superfluid velocity *far* from the strings of normal fluid (the vortex cores) and the particles introduced via Eq. (5.34) would be tracers of the superfluid. Here, however, we allow the particle to move close to the vortex where the phase gradient diverges and the superfluid-velocity approximation is not valid. Also, the coefficients of the CGL equation are not purely imaginary. The physical interpretation of the particle velocity scheme (5.34) is therefore less obvious than for the superfluid case.

The particle with velocity (5.34) has no inertia in this scheme, the equation of motion being purely dissipative. We are interested in the trajectories and in the statistics of the particle motion when the underlying field is turbulent. However, for the sake of illustration, we first consider a particle that moves in a glassy state of the CGL system, where the influence of the defects is clearly discerned and understood.

For an isolated vortex, the phase gradient points towards the vortex center, except in the area close to the center. There, the gradient lines spiral around the center counterclockwise for vortices of positive winding number ($n = 1$), and clockwise for negative winding number ($n = -1$); see Fig. 5.4. Therefore, a particle with $\Gamma > 0$ is attracted to the vortex (no matter the sign of the winding number), and the particle will spiral towards the center. In contrast, a particle with $\Gamma < 0$ will be repelled by the vortex. In a vortex glass, such particles will

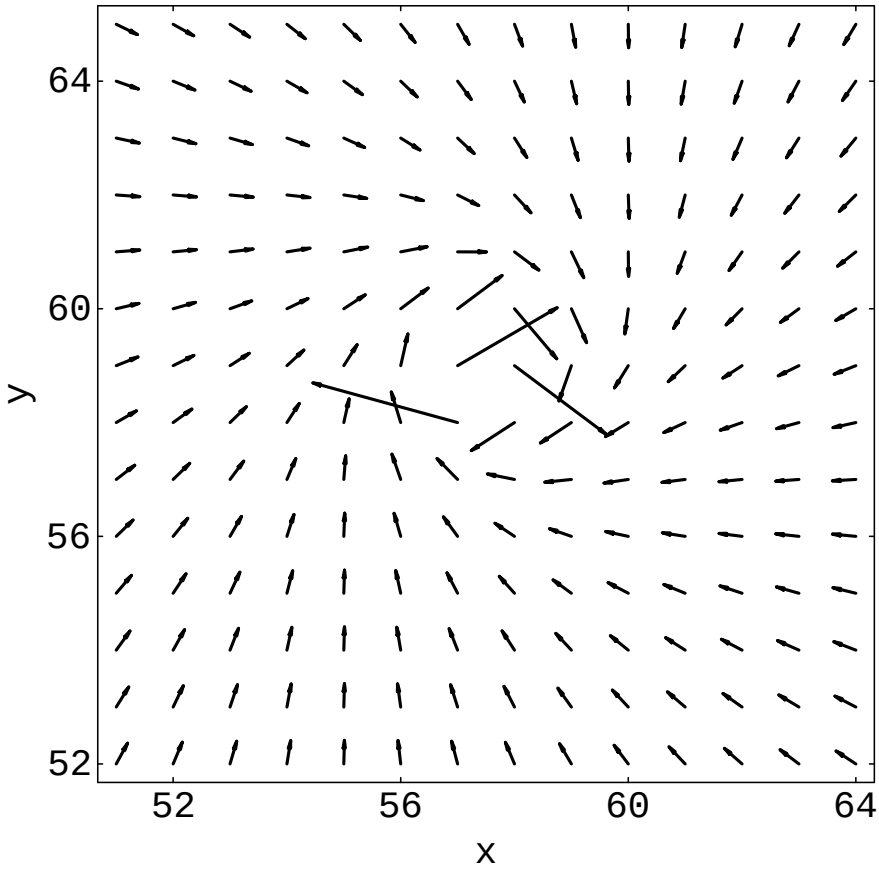

Figure 5.4: The CGL equation. The phase gradient $\nabla S(\boldsymbol{r})$ in the region around the center of a negative winding number vortex ($n = -1$). The x- and y-values are lattice site numbers.

move as far as possible from any vortex, which means that they will get trapped at the junction of three domain walls. This argument does not take edge vortices into account.

We now study the motion of the particles in the turbulent regime of the CGL equation. More specifically, we look at a system with 128×128 lattice sites with the parameter values $(\alpha, \beta) = (1, -2)$. The defect-turbulent regime is characterized by moving vortices and the creation and annihilation of vortex pairs. A particle with $\Gamma > 0$ is also in this regime attracted to the vortices and tries to move with them. However, if Γ is sufficiently small, the particle velocity is too small to follow the vortex motion. Even if Γ is large enough for the particle to follow the motion of a vortex, it will not follow the vortex forever. The vortex

will eventually get annihilated by a vortex of opposite winding number, and the particle will find another vortex and follow the motion of that vortex.

Close to the center of a vortex we can approximate the phase field $S(\boldsymbol{r})$ at small time scales in the turbulent regime (time scales small enough that the vortices hardly move) by the phase field of an isolated vortex (5.4), in polar coordinates (r,φ)

$$S(r,\varphi,t) = -\omega t + n\varphi + \psi(r) \tag{5.35}$$

where the r-dependence is (see Eq. (5.6))

$$\psi(r) = d_2 r^2 + d_4 r^4 + \ldots \tag{5.36}$$

Thus the particle velocity is, in polar coordinates

$$\begin{aligned} \boldsymbol{v} &= \Gamma \nabla S(\boldsymbol{r},t) \\ &= \Gamma\,(\hat{\boldsymbol{r}}\partial_r S + \frac{\hat{\boldsymbol{\varphi}}}{r}\partial_\varphi S) \\ &= (\hat{\boldsymbol{r}}\Gamma\,\partial_r\psi(r) + \hat{\boldsymbol{\varphi}}\frac{\Gamma n}{r}) \end{aligned} \tag{5.37}$$

which we integrate to lowest order in r to obtain the particle position $\boldsymbol{r}(t) = re^{i\varphi}$ as a function of time

$$r(t) = r_0 e^{2\Gamma d_2 t} \tag{5.38}$$

$$\varphi(t) = \varphi_0 - \frac{n}{4r_0^2 d_2}\left(e^{-4\Gamma d_2 t} - 1\right) \tag{5.39}$$

This confirms the spiraling motion of the particle close to the vortex center. In our numerical simulations, we interpolated the phase gradient at the off-lattice particle position from four first-order gradients at the four nearest lattice sites. The simulated particles spiral towards the vortex center, as we predicted from the gradient of the phase (Fig. 5.4) and from the particle motion at a fixed isolated vortex, but the spiraling motion is eventually replaced by a circulating motion around the center due to the finite lattice spacing. This is illustrated in Figs. 5.5 and 5.6, where we plot a particle trajectory for the parameter $\Gamma = 10$. With $\Gamma = 10$ the particle gets trapped at moving vortices, but once in a while the vortex disappears, and the particle finds and sticks to another vortex. For figures corresponding to other values of Γ, I refer to Figure 3 in Paper II.

As in the case of the experiment on self-diffusion of particles in surface waves (described in previous chapters) we studied the distribution of particle

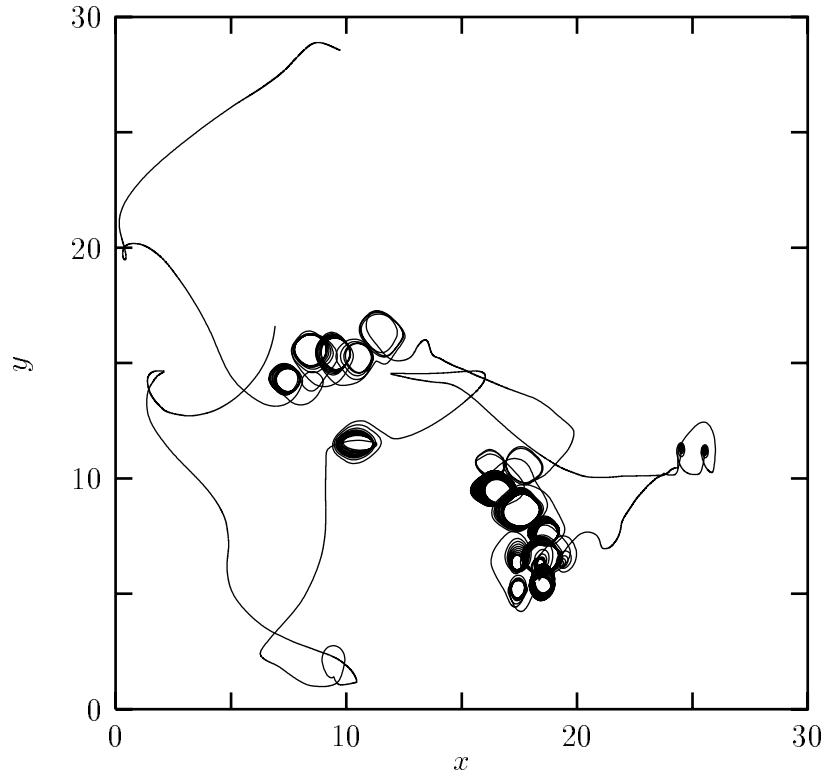

Figure 5.5: The CGL equation. Particle trajectory for $\Gamma = 10$ in the turbulent regime $(\alpha, \beta) = (1, -2)$. The trapping of the particle by the vortices is clearly seen as a circular motion. The duration of the trajectory is $t = 300$ (30000 time steps of size $\tau = 0.01$). We let the system achieve a steady-state vortex density before recording the trajectory.

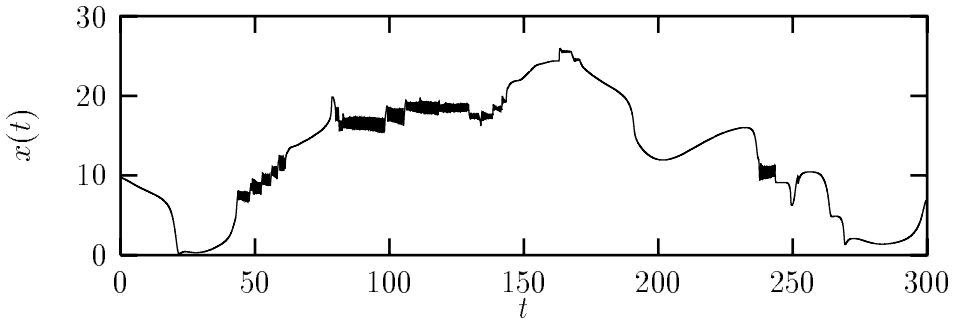

Figure 5.6: The CGL equation. Position in x-direction versus time t for the trajectory in Fig. 5.5.

displacements in the CGL equation. We found the second moment $\langle(\Delta r)^2\rangle = \langle[r(t+\Delta t)-r(t)]^2\rangle$ as a function of Δt for various values of Γ. Results for $\Gamma = 1$, 10, 100, and -1.2 are shown in Figure 5.7.

We find that at small, positive Γ, where the particle does not get trapped at vortices, the motion crosses over from ballistic motion [$\langle(\Delta r)^2\rangle \propto (\Delta t)^2$] at small time scales, to Brownian diffusion $\langle(\Delta r)^2\rangle = D\Delta t$ at large time scales. This defines a diffusion coefficient D, which does not depend on the time scales considered, unlike the diffusion coefficient for *fractional* Brownian motion (Chapter 4). Note that the diffusion coefficient D defined here is twice the diffusion coefficient defined in Chapter 4.

For larger values of positive Γ the particles spend a large fraction of the time being trapped at vortices. In that case, the motion is ballistic at very small time scales, but the change to Brownian motion at large time scales is more complicated than that for small Γ. The $\langle(\Delta r)^2\rangle$ – Δt curves show a local maximum (a 'hump') at a time scale that corresponds to approximately half a period in the motion around a vortex (Fig. 5.7). Thus, our interpretation is that the local maximum of the curve arises because the distance of half a circulation is the furthest the particle gets on short time scales. The local minimum is at the time scale that corresponds to one full circulation. The diffusion on long time scales mainly describes the particle motion *between* the vortices. We find that the diffusion is suppressed because the particles spend time being trapped at the vortices, and the trapping limits the diffusion to that of the vortex motion.

Particles with negative Γ do not circulate the vortices. Instead, they aim at positioning themselves furthest from the neighboring vortices[1]. At small $|\Gamma|$ they do not quite succeed in getting there before the configuration of vortices has changed, and their motion resembles that of particles with small positive Γ. For larger, negative Γ the particles do succeed in following their optimal position between the vortices most of the time. Their motion therefore traces the dynamics of the phase field, without the small time scale circulation.

This is further emphasized in Fig. 5.8. The figure shows the diffusion coefficient D as a function of Γ. For small $|\Gamma|$ we find that $D \propto \Gamma^2$. The appropriate physical picture in this case is that of a particle being kicked about by an underlying random vector field. In this picture, the diffusion coefficient is the squared drift velocity $\langle \boldsymbol{v}^2\rangle = \Gamma^2\langle|\nabla S|^2\rangle$ times the typical collision time, which

[1]Strictly speaking, the particles follow the downward slope of the phase gradient, and the 'optimal' (stable, if the vortex configuration were frozen instantaneously) position of a particle may not be exactly the position furthest in space from the vortices.

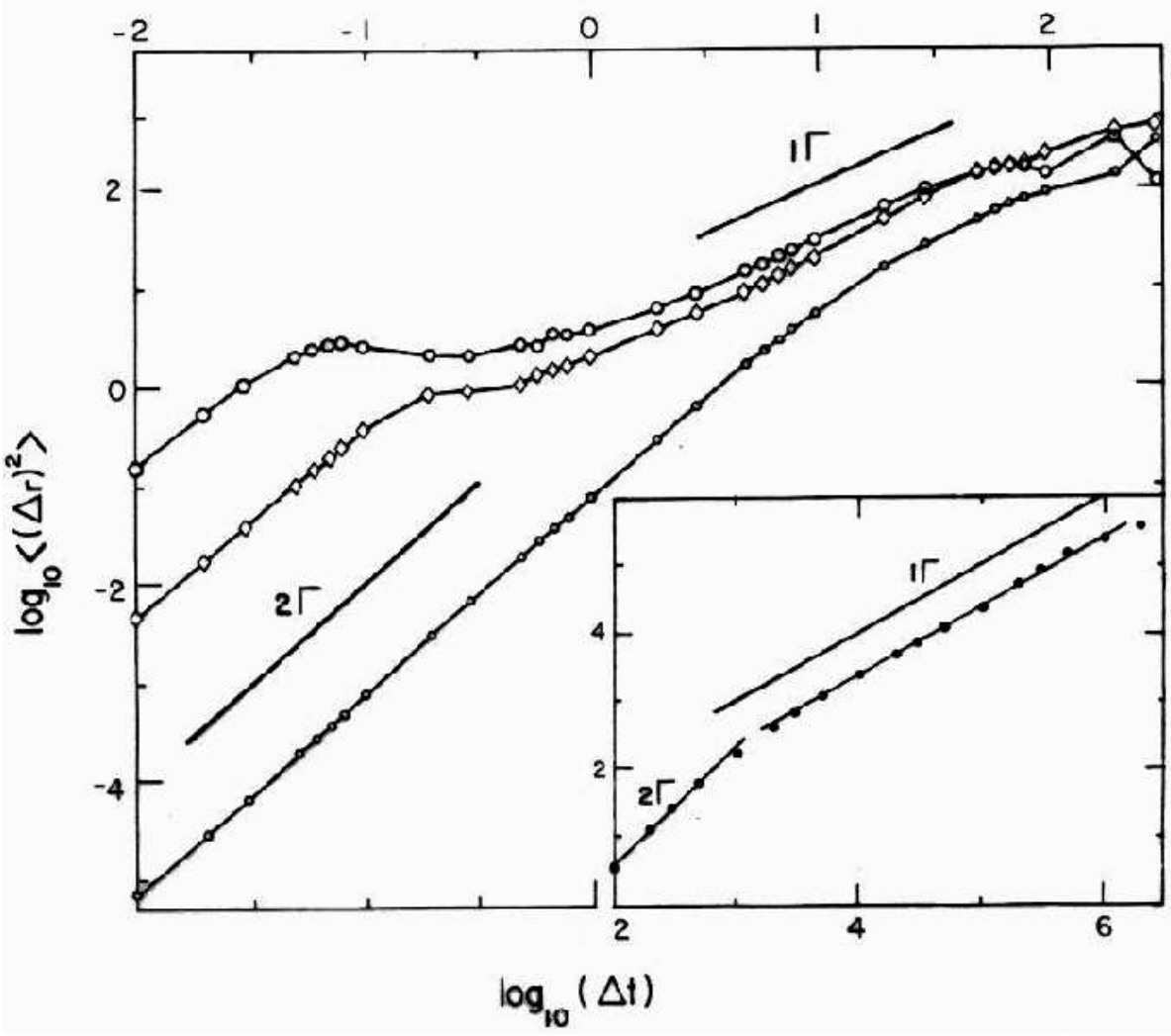

Figure 5.7: The CGL equation. The second moment of the particle displacements $\langle(\Delta r)^2\rangle$ versus the time interval Δt for $\Gamma = 1$ (small circles), $\Gamma = 10$ (diamonds), and $\Gamma = 100$ (big circles). *Inset:* $\langle(\Delta r)^2\rangle$ versus Δt for $\Gamma = -1.2$.

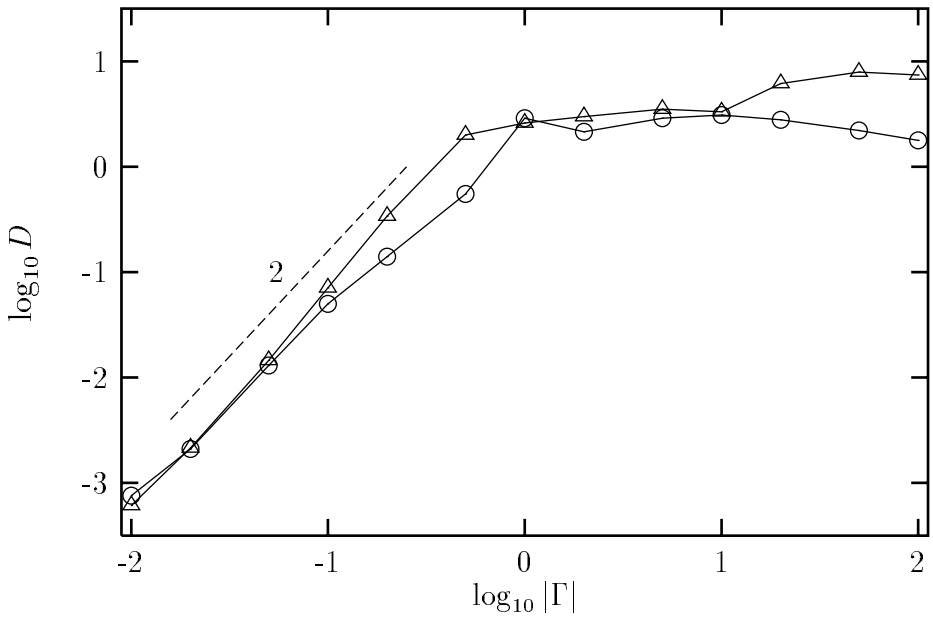

Figure 5.8: The CGL equation. The self-diffusion coefficient D as a function of the parameter $|\Gamma|$. $\Gamma < 0$: triangles, $\Gamma > 0$: circles.

gives $D \propto \Gamma^2$.

At large $|\Gamma|$, the particle diffusion is limited to that of the underlying field, as already discussed. But the underlying field is not affected by the presence of the particle, thus $D = D_{field}$ is independent of Γ, as seen in Fig. 5.8.

We also measured the relative motion of pairs of particles, in a manner similar to the measurements in the Faraday experiment. We measured the relative diffusion $\Delta(R^2)/\Delta t$, where R is the separation of the two particles. We found that the probability density function of the relative diffusion, shown in Figure 6(a) of Paper II, falls off exponentially. The probability density function is certainly not a Gaussian distribution. A similar result was found for the Faraday relative motion, Chapter 2. For a further discussion of the relative motion in the CGL equation, along with consequences of adding a scalar field to the CGL equation, I refer to Paper II.

5.4 Phase turbulence

Up until here I have concentrated on the solutions to the CGL equation that contain defects. Another set of interesting solutions are those that are perturbations

of the homogeneous solution $A = F\exp(-i\omega t)$. The homogeneous solution is unstable for $1+\alpha\beta < 0$, i.e. above the Benjamin-Feir line in Fig. 5.2. Close above the Benjamin-Feir line a perturbative analysis in the small parameter $1 + \alpha\beta$ yields an equation for the modified phase ϕ to third order in $1 + \alpha\beta$ [48, 67, 68, 69]

$$\partial_t\phi = \Omega_2^{(1)}\nabla^2\phi + \Omega_2^{(2)}(\nabla\phi)^2 + \Omega_4^{(1)}\nabla^4\phi \tag{5.40}$$

where the coefficients are given by

$$\Omega_2^{(1)} = 1 + \alpha\beta \qquad \Omega_2^{(2)} = \alpha - \beta \qquad \Omega_4^{(1)} = -\frac{\beta^2}{2}(1 + \alpha^2)\ . \tag{5.41}$$

Eq. (5.40) is the Kuramoto-Sivashinsky equation, which has chaotic solutions. The corresponding behavior of the CGL systems is named 'phase turbulence'. Note, though, that Eq. (5.40) is obtained as a perturbation in the small parameter $1 + \alpha\beta$, and it is therefore only valid close to the Benjamin-Feir line. The start of creation of defects will destroy the phase turbulence. One therefore expects phase turbulence to be limited approximately to the region between the Benjamin-Feir line and the line of absolute instability; see Fig. 5.2. Phase turbulence has previously been investigated in the one-dimensional CGL equation [67, 70, 71, 68], and only recently in two dimensions [72].

We simulated the CGL equation without initial defects for a limited number of values (α, β) both within and outside of the regions in the $\alpha - \beta$ plane in which there is reason to believe [72] that phase turbulence exists in finite systems. At small values of $|\beta|$ (around $\beta \approx -2$) we did not see any phase turbulence that did not either break down into defect turbulence (see Fig. 5.9) or relax to the homogeneous state. At a larger value of $|\beta|$ [at $(\alpha, \beta) = (0.5, -3.5)$] we saw a phase-turbulent state that did not break down or relax within the period of time that we studied the state ($1.17 \cdot 10^6$ time steps of size $\tau = 0.1$). However, we did not pursue a very systematic investigation of these states at values of $|\beta| > 2$, and it is difficult to say anything very conclusive from these simulations at high $|\beta|$.

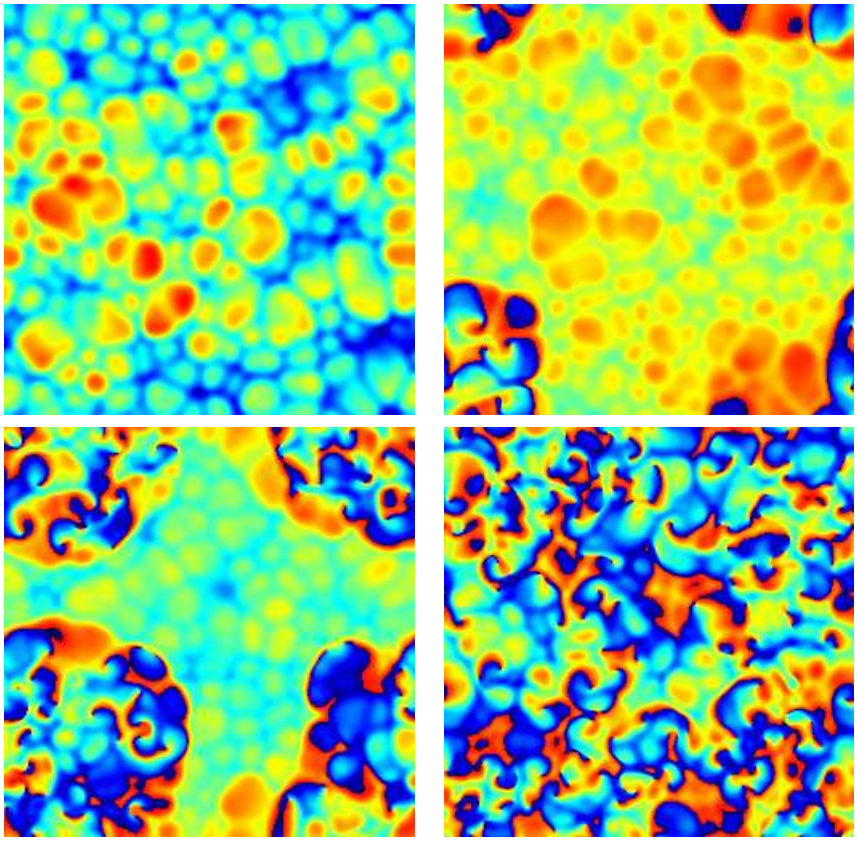

Figure 5.9: Break down of phase turbulence. Snapshots of the phase $S(\boldsymbol{r}, t)$ in the two-dimensional CGL equation at parameters $(\alpha, \beta) = (0.78, -2)$. The color scale goes from red at the minimum via green to blue at the maximum value of S. For all pictures except the top left picture this means that red is $S \approx 0$, green is $S \approx \pi$, and blue is $S \approx 2\pi$. *Top left:* Phase turbulence. *Top right:* Vortices (defect turbulence) have appeared in the lower left corner of the system and have started to spread. This is 1200 time steps after the first picture. *Bottom left:* Defect turbulence has spread further. 4200 time steps after the first picture. *Bottom right:* 7000 time steps after the first picture. The whole system is defect turbulent except a small fraction close to the middle of the picture. This small area will become defect turbulent after a few more steps. The system size is 256×256 lattice sites, and the size of one time step is $\tau = 0.1$. The system was started from a state with A chosen randomly within the ring $0.5 < |A| < 1$ in the complex plane, and with periodic boundary conditions.

Chapter 6

Vortex Motion in the Complex Ginzburg-Landau Equation

In this chapter we study the motion of defects, or filaments, in the complex Ginzburg-Landau equation for the complex field $A = |A| \exp(iS)$. The evolution of a system with vortices may be described in terms of the motion of the defects (located at points where $|A| = 0$), along with values of the fields $|A|$ and S at positions away from the defects or filaments. There appears to be two very different approaches to this problem. In one approach the aim is to find an exact expression for the velocity of the defects given by the unknown global fields. In the other approach the defect velocity is found in an approximation, but expressed through known fields. Here we take the first approach, whereas a number of other people [73, 74] have taken the second approach.

Below, we describe a few of the previous derivations of the vortex motion in the complex Ginzburg-Landau equation and in related equations. Following this, the local coordinate system at the vortex is introduced, and finally the vortex velocity expressed through the field A is derived. This chapter is an extension of the Paper IV.

6.1 Introduction

We study the defects of the complex Ginzburg-Landau equation (5.1)

$$\frac{d}{dt} A = P(A, A^*)A + b\nabla^2 A \tag{6.1}$$

where $A = |A| \exp(iS)$ is a complex field, the function P is given by $P(A, A^*) = \mu - a|A|^2$, and a, b, μ are complex coefficients. We note that only defects with

winding numbers $n = \pm 1$ are stable [53, 57]. However, for the sake of generality we keep n as an unknown integer throughout our derivation.

The evolution of a system with vortices may be described in terms of the motion of the defects, or filaments, along with values of the fields $|A|$ and S at positions away from the defects or filaments. These fields include the effect of any boundaries and other defects. Such a separation into collective coordinates and field variables is non-trivial, and the work described here comprises the first exact treatment of this kind for a dissipative system.

The motion of a vortex is affected by modifications in the field A due to the presence of other vortices or system boundaries. If the vortices are assumed to form a dilute system, i.e. one where the defects are well separated, the influence of variations in the amplitude $|A|$ of the complex field may be neglected, since $|A|$ will assume its asymptotic value at distances much smaller than the inter-defect distance. In the Ginzburg-Pitaevskii-Gross equation (GPG, see Chapter 5 and Ref. [60]) for superfluids this corresponds to the incompressible approximation. Under this assumption, the interaction between vortices can be described entirely by the phase S.

In this approximation Rica and Tirapegui [75] (and in a slightly different form also Ref. [76]) have derived the equation of motion in two space dimensions for the position of the kth defect $\boldsymbol{X}_k(t)$ in terms of the portion of the phase S due to other defects, $\theta^{(k)}(\boldsymbol{x}) \equiv S - n_k\varphi_k$, where $\tan\varphi_k = (y - Y_k)/(x - X_k)$. Their result (for $|n_k| = 1$ and $b_R = 1$, but here generalized to any value of n_k and b_R) is

$$\dot{\boldsymbol{X}}_k \equiv \frac{d\boldsymbol{X}_k}{dt} = 2b_I \nabla\theta^{(k)} - 2b_R \frac{n_k}{|n_k|}\hat{\boldsymbol{z}} \times \nabla\theta^{(k)} \ , \tag{6.2}$$

where $\hat{\boldsymbol{z}} = \hat{\boldsymbol{x}} \times \hat{\boldsymbol{y}}$ is normal to the plane. The first term, proportional to the gradient, is that found by Fetter [77] in the GPG limit corresponding to $b_R = 0$, $b_I = \hbar/(2m)$ and states that the vortex moves with the local superfluid velocity. The second term is the perpendicular Peach-Koehler term [78] first found in this context by Kawasaki [79]. When the system of spiral vortices cannot be approximated by a dilute system the expression (6.2) for the defect velocity is no longer valid but will acquire additional terms.

We shall take a completely general approach in which the amplitude $|A|$ is allowed to vary. This will enable us to determine the exact motion of a defect also when another defect is located an arbitrarily small distance away, i.e. even when the vortex cores overlap. It will also provide the exact motion of a defect which is arbitrarily near a system boundary. For filaments in a three-dimensional

system our treatment will furthermore correctly incorporate interactions with other segments of the same filament.

The corresponding problem for a relativistic scalar field theory was solved by Ben-Ya'acov [80]. His derivation was based strictly on a covariant world-sheet formalism that cannot be applied to a non-relativistic theory. In the GPG case the system is conservative and the motion of the defects can be derived from a Lagrangian. The CGL equation, on the other hand, describes a dissipative system, and one is compelled to pursue a direct derivation of the defect equation of motion, as we do here.

6.2 Derivation of the Vortex Velocity

We may generalize the CGL equation (6.1) by admitting any continuous function $P(A, A^*)$ for which the equation has vortex solutions. The details of P do not enter the following derivation of the vortex velocity. We consider the Eq. (6.1) in three spatial dimensions. The motion in a two-dimensional system can be found from the three-dimensional problem as the special case of straight, aligned vortices.

Let the position of the filament Γ of a vortex be given at time t by $\boldsymbol{X}(s,t)$, where s is the arclength coordinate along Γ. We define a local coordinate system along the string as follows [81]. At each point along the string the unit tangent vector $\boldsymbol{T} = \partial \boldsymbol{X}/\partial s$, the unit normal vector $\boldsymbol{N}$, and the binormal vector $\boldsymbol{B} = \boldsymbol{T} \times \boldsymbol{N}$ form an orthonormal frame so that any position $\boldsymbol{x}$ in a neighborhood of the string can be expressed as $\boldsymbol{x} = \boldsymbol{X}(s,t) + x\boldsymbol{N}(s,t) + y\boldsymbol{B}(s,t)$; see Fig. 6.1. The coordinate representation (s,x,y) is unique for $x < 1/\kappa$ but becomes singular when x reaches or exceeds the radius of curvature $1/\kappa$.

Along the string, the transport of the unit vectors is given by the Frenet-Serret equations [81]

$$\frac{\partial \boldsymbol{T}}{\partial s} = \kappa \boldsymbol{N}, \quad \frac{\partial \boldsymbol{N}}{\partial s} = -\kappa \boldsymbol{T} + \tau \boldsymbol{B}, \quad \frac{\partial \boldsymbol{B}}{\partial s} = -\tau \boldsymbol{N}, \tag{6.3}$$

where κ is the curvature and τ is the torsion of the string. Let us further introduce the local polar coordinates r, φ defined by $x = r\cos\varphi$, $y = r\sin\varphi$. In terms of these coordinates, the gradient and Laplacian take the forms

$$\nabla \;=\; \boldsymbol{T}H + \hat{\boldsymbol{r}}\frac{\partial}{\partial r} + \hat{\boldsymbol{\varphi}}\frac{1}{r}\frac{\partial}{\partial \varphi} \tag{6.4}$$

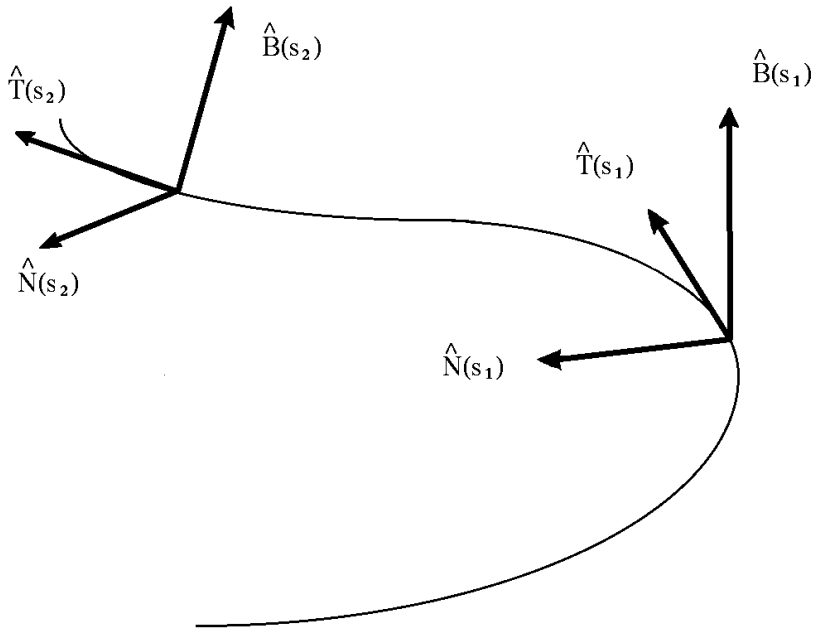

Figure 6.1: The local coordinate systems that follow the filament. The torsion $\tau(s,t)$ is the change of the binormal $\boldsymbol{B}$ along the curve, $|\tau(s,t)| = |\partial \boldsymbol{B}/\partial s|$.

$$\nabla^2 = H^2 + \frac{\partial^2}{\partial r^2} + \frac{1}{r}\frac{\partial}{\partial r} + \frac{1}{r^2}\frac{\partial^2}{\partial \varphi^2} - \frac{\kappa}{1-\kappa r\cos\varphi}\left(\cos\varphi\frac{\partial}{\partial r} - \sin\varphi\frac{1}{r}\frac{\partial}{\partial\varphi}\right) \tag{6.5}$$

with the operator

$$H = \frac{1}{1-\kappa r\cos\varphi}\left(\frac{\partial}{\partial s} - \tau\frac{\partial}{\partial\varphi}\right) . \tag{6.6}$$

We now proceed to find the velocity $\dot{\boldsymbol{X}}(s,t)$ of the filament Γ. Because this string of zeros of the function A has no transverse extension and is a feature of a solution of an underlying local field theory, its motion should be determined from the behavior of the fields $|A|$ and S in an infinitesimal neighborhood of the filament. It will be sufficient to study the fields within a distance $\varepsilon \ll \min(d, 1/\kappa)$, where d is the shortest distance to another string segment[1]. This condition ensures uniqueness of the coordinate representation.

The phase field S is multi-valued and satisfies $S(s,r,\varphi+2\pi;t) - S(s,r,\varphi;t) = n\,2\pi$ for $0 < r < \varepsilon$. Let us therefore split $S = \chi + \theta$ in such a way that χ contains all multi-valued contributions to the phase and depends on time only through the position of the filament Γ. For a straight (or two-dimensional) isolated vortex one may choose $\chi = n\varphi$. A consistent description of the multi-valued phase of an arbitrarily shaped vortex filament requires, however, a global realization such as the Biot-Savart integral,

$$\nabla\chi = \frac{n}{2}\int_\Gamma d\boldsymbol{X} \times \frac{\boldsymbol{x}-\boldsymbol{X}}{|\boldsymbol{x}-\boldsymbol{X}|^3} \sim n\left(\frac{1}{r} + \frac{\kappa}{2}\cos\varphi\right)\hat{\boldsymbol{\varphi}} - \frac{n\kappa}{2}\ln\kappa r\,\boldsymbol{B} + \text{regular.} \tag{6.7}$$

This expression contains logarithmic divergencies as $r \to 0$, as well as functions of the azimuthal angle φ that are multi-valued at $r = 0$ [82]. We therefore absorb in χ any part of S that is non-differentiable at $r = 0$.

Similarly, we may write $|A| = Rw$, where $\ln R$ depends on the filament position and contains all contributions to $\ln|A|$ that are non-differentiable at $r = 0$. For a straight isolated vortex one may choose $R = r^{|n|}$. Thus θ and $\ln w$ are differentiable and it follows that the time derivatives $\dot{\theta}$ and $\dot{w}$ are finite for $r < \varepsilon$.

[1]The shortest distance from a fixed string segment at $\mathbf{X}_k(s,t)$ on the kth vortex to another string segment at $\mathbf{X}_l(s',t)$ is defined as the smallest non-zero value of $|\mathbf{X}_k(s,t) - \mathbf{X}_l(s',t)|$, as l and s' are varied, that corresponds to a local minimum with respect to s'.

We remark that the choice of χ and R is not unique, since S and $|A|$ are invariant under two independent local symmetries

$$\chi \to \chi + \delta,\ \theta \to \theta - \delta \quad ; \quad R \to Rf,\ w \to wf^{-1}\ , \tag{6.8}$$

where δ and $\ln f$ are differentiable.

With these definitions the real and imaginary parts of Eq. (6.1) lead to the two equations

$$\frac{d}{dt}\left(\ln R + \ln w\right) = \mathrm{Re}(P) + b_R Q_1 - b_I Q_2\ , \tag{6.9}$$

$$\frac{d}{dt}\left(\theta + \chi\right) = \mathrm{Im}(P) + b_I Q_1 + b_R Q_2\ , \tag{6.10}$$

where

$$Q_1 = \nabla^2 \ln R + \nabla^2 \ln w + (\nabla \ln R + \nabla \ln w)^2 - (\nabla\chi + \nabla\theta)^2 \tag{6.11}$$

$$Q_2 = \nabla^2\chi + \nabla^2\theta + 2(\nabla \ln R + \nabla \ln w)\cdot(\nabla\chi + \nabla\theta). \tag{6.12}$$

The time derivative d/dt in Eqs. (6.9) and (6.10) is to be evaluated in the lab frame. It is related to the time derivative $\partial/\partial t$ in a frame following the local segment of the filament in such a way that s, x and y are constant by

$$\frac{d}{dt} = -(\dot{\boldsymbol{X}} + x\dot{\boldsymbol{N}} + y\dot{\boldsymbol{B}})\cdot\nabla + \frac{\partial}{\partial t} \tag{6.13}$$

In general, global expressions for $\nabla\chi$ and $\nabla \ln R$ will include singularities at $r = 0$ of the type demonstrated by Eq. (6.7). We therefore write

$$\nabla\chi = f_1\hat{\boldsymbol{r}} + \left(\frac{n}{r} + f_2\right)\hat{\boldsymbol{\varphi}} + \lambda_1\boldsymbol{T} \tag{6.14}$$

and

$$\nabla \ln R = \left(\frac{|n|}{r} + f_3\right)\hat{\boldsymbol{r}} + f_4\hat{\boldsymbol{\varphi}} + \lambda_2\boldsymbol{T}\ , \tag{6.15}$$

where

$$f_i(r,\varphi,s,t) = g_i(\varphi,s,t) + h_i(\varphi,s,t)\ln\kappa r + \mathcal{O}(r) \tag{6.16}$$

and $\mathcal{O}(r)$ denotes any terms that vanish as $r \to 0$. It can be easily confirmed from these equations that $\partial\chi/\partial t$, $\partial\chi/\partial s$, $\partial(\ln R)/\partial t$, $\partial(\ln R)/\partial s$, λ_1 and λ_2 have well-defined finite limits as $r \to 0$ by looking at the form of the gradient in the

local coordinate system (6.4). We require that $\nabla\chi$ and $\nabla \ln R$ be integrable (for $0 < r < \varepsilon$), and that they satisfy the following condition near the filament:

$$\nabla\chi - \frac{n}{|n|}\boldsymbol{T} \times \nabla \ln R = \boldsymbol{C}(s,t) + \mathcal{O}(r) \ . \tag{6.17}$$

The arbitrary vector $\boldsymbol{C}$ corresponds to a choice of gauge in Eq. (6.8). In the *symmetric gauge* $R = r^{|n|}$, $\chi = n\varphi$ for a straight (or two-dimensional) isolated vortex we have $\boldsymbol{C} = \boldsymbol{0}$. A more general derivation allows for powers of the logarithm $\ln \kappa r$ and factors of r in $\nabla\chi$, $\nabla \ln R$ and on the right-hand side of Eq. (6.17). However, this does not affect the expression for the vortex velocity, so here we use Eqs. (6.16) and (6.17) for clarity.

Since θ and $\ln w$ are differentiable, the singularities of $\nabla\chi$ and $\nabla \ln R$ at $r = 0$ must satisfy Eqs. (6.9) and (6.10) order by order with

$$\begin{aligned} Q_1 &= \nabla^2 \ln R + (\nabla \ln R)^2 + 2\nabla \ln R \cdot \nabla \ln w \\ &\quad - (\nabla\chi)^2 - 2\nabla\chi \cdot \nabla\theta + \text{regular} \qquad (6.18) \\ Q_2 &= \nabla^2\chi + 2\nabla \ln R \cdot \nabla\chi \qquad (6.19) \\ &\quad + 2\nabla \ln R \cdot \nabla\theta + 2\nabla \ln w \cdot \nabla\chi + \text{regular.} \qquad (6.20) \end{aligned}$$

This last condition together with Eq. (6.17), leads to the coupled nonlinear system

$$\begin{aligned} \nabla \ln R \cdot \boldsymbol{u} + b_R q_1 - b_I q_2 &= \text{regular} \qquad (6.21) \\ \nabla\chi \cdot \boldsymbol{u} + b_I q_1 + b_R q_2 &= \text{regular} \ , \qquad (6.22) \end{aligned}$$

where

$$\begin{aligned} q_1 &= \nabla^2 \ln R + (\nabla \ln R)^2 - (\nabla\chi)^2 \ , \qquad (6.23) \\ q_2 &= \nabla^2\chi + 2\nabla \ln R \cdot \nabla\chi \qquad (6.24) \end{aligned}$$

and

$$\boldsymbol{u} = \dot{\boldsymbol{X}} + 2b_R\left(\nabla \ln w + \frac{n}{|n|}\boldsymbol{T} \times \nabla\theta\right) - 2b_I\left(\nabla\theta - \frac{n}{|n|}\boldsymbol{T} \times \nabla \ln w\right) \tag{6.25}$$

and where we used the general vector formula $\mathcal{A}\cdot(\mathcal{B}\times\mathcal{C}) = -\mathcal{C}\cdot(\mathcal{B}\times\mathcal{A})$. We note that the following terms in the expressions for the time derivatives are regular:

$$\begin{aligned} (x\dot{\boldsymbol{N}} + y\dot{\boldsymbol{B}}) \cdot \nabla \ln R &= (g_4(\varphi,s,t)r + h_4(\varphi,s,t)r \ln \kappa r)\boldsymbol{B} \cdot \dot{\boldsymbol{N}} \\ &\quad + r\lambda_2(\cos\varphi\dot{\boldsymbol{N}} + \sin\varphi\dot{\boldsymbol{B}}) \cdot \boldsymbol{T} + \mathcal{O}(r^2) \qquad (6.26) \end{aligned}$$

and

$$(x\dot{\boldsymbol{N}} + y\dot{\boldsymbol{B}}) \cdot \nabla\chi = (n + g_2(\varphi,s,t)r + h_2(\varphi,s,t)r\ln\kappa r)\boldsymbol{B}\cdot\dot{\boldsymbol{N}} + r\lambda_1(\cos\varphi\dot{\boldsymbol{N}} + \sin\varphi\dot{\boldsymbol{B}})\cdot\boldsymbol{T} + \mathcal{O}(r^2) \tag{6.27}$$

where we used the fact that $\dot{\mathcal{A}}\cdot\mathcal{B} = -\dot{\mathcal{B}}\cdot\mathcal{A}$ for orthogonal unit vectors $\mathcal{A}$ and $\mathcal{B}$.

We see that $\boldsymbol{u}$ is regular, and the singularities of Eqs. (6.21) and (6.21) are found in q_1, q_2, $\nabla\ln R$ and $\nabla\chi$. Inserting the expressions (6.14–6.16) into these equations gives

$$\begin{aligned} q_1 &= \partial_r f_3 + \frac{1}{r}\partial_\varphi f_4 - \left(\frac{|n|}{r} + f_3\right)\frac{\kappa\cos\varphi}{1-\kappa r\cos\varphi} + f_4\frac{\kappa\sin\varphi}{1-\kappa r\cos\varphi} \\ &\quad + f_3^2 + \frac{2|n|+1}{r}f_3 + f_4^2 - f_1^2 - \frac{2n}{r}f_2 - f_2^2 + \lambda_2^2 - \lambda_1^2 + H\lambda_2 \\ &= \{-\kappa|n|\cos\varphi + h_3 + g_4' + (2|n|+1)g_3 - 2ng_2\}\,r^{-1} \\ &\quad + \{h_4' + (2|n|+1)h_3 - 2nh_2\}\,r^{-1}\ln\kappa r + \left\{h_3^2 + h_4^2 - h_1^2 - h_2^2\right\}(\ln\kappa r)^2 \\ &\quad + \{\kappa h_4\sin\varphi - \kappa h_3\cos\varphi + 2g_3h_3 + 2g_4h_4 - 2g_1h_1 - 2g_2h_2\}\ln\kappa r \\ &\quad + \text{regular} \end{aligned} \tag{6.28}$$

$$\begin{aligned} q_2 &= \partial_r f_1 + \frac{1}{r}\partial_\varphi f_2 - f_1\frac{\kappa\cos\varphi}{1-\kappa r\cos\varphi} + \left(\frac{n}{r} + f_2\right)\frac{\kappa\sin\varphi}{1-\kappa r\cos\varphi} \\ &\quad + \frac{2|n|+1}{r}f_1 + 2f_1f_3 + \frac{2n}{r}f_4 + 2f_2f_4 + 2\lambda_1\lambda_2 + H\lambda_1 \\ &= \{\kappa n\sin\varphi + h_1 + g_2' + (2|n|+1)g_1 + 2ng_4\}\,r^{-1} \\ &\quad + \{h_2' + (2|n|+1)h_1 + 2nh_4\}\,r^{-1}\ln\kappa r + 2\{h_1h_3 + h_2h_4\}(\ln\kappa r)^2 \\ &\quad + \{\kappa h_2\sin\varphi - \kappa h_1\cos\varphi + 2g_1h_3 + 2g_3h_1 + 2g_2h_4 + 2g_4h_2\}\ln\kappa r \\ &\quad + \text{regular} \end{aligned} \tag{6.29}$$

where the time, arclength, and angular dependence of the coefficients g_i and h_i is not explicitly shown.

The integrability condition on χ and $\ln R$

$$\partial_\varphi\partial_r\chi = \partial_r\partial_\varphi\chi \qquad \text{and} \qquad \partial_\varphi\partial_r\ln R = \partial_r\partial_\varphi\ln R \tag{6.30}$$

provides four first-order differential equations that relate the functions g_i and h_i

$$\begin{aligned} g_2 + h_2 &= g_1' \quad ; \quad h_2 = h_1' \\ g_4 + h_4 &= g_3' \quad ; \quad h_4 = h_3' \end{aligned} \tag{6.31}$$

The condition (6.17) furthermore provides four algebraic relations, with $\boldsymbol{C} = C_1\boldsymbol{N} + C_2\boldsymbol{B} + C_3\boldsymbol{T}$,

$$\begin{aligned} g_1 + \frac{n}{|n|}g_4 &= C_1\cos\varphi + C_2\sin\varphi \\ g_2 - \frac{n}{|n|}g_3 &= -C_1\sin\varphi + C_2\cos\varphi \\ h_1 + \frac{n}{|n|}h_4 &= 0; \qquad h_2 - \frac{n}{|n|}h_3 = 0 \end{aligned} \tag{6.32}$$

We now return to the coupled system (6.21) and (6.22). Cancellation of terms of order r^{-1} leads to two equations for the perpendicular components of $\boldsymbol{u}$, with $\boldsymbol{u}_\perp = u_1\boldsymbol{N} + u_2\boldsymbol{B}$,

$$0 = |n|u_1\cos\varphi + |n|u_2\sin\varphi + b_R\varpi_1 - b_I\varpi_2 \tag{6.33}$$

$$0 = -nu_1\sin\varphi + nu_2\cos\varphi + b_I\varpi_1 + b_R\varpi_2 \tag{6.34}$$

where ϖ_1 and ϖ_2 are expressed in terms of g_i and h_i as

$$\varpi_1 = -\kappa|n|\cos\varphi - 2ng_2 + g_4' + (2|n|+1)g_3 + h_3 \tag{6.35}$$

$$\varpi_2 = \kappa n\sin\varphi + (2|n|+1)g_1 + h_1 + g_2' + 2ng_4\ . \tag{6.36}$$

By using the relations (6.31) and (6.32) the coefficients g_i and h_i can be eliminated from the expressions for ϖ_1 and ϖ_2, e.g.

$$\begin{aligned} g_2' &= \frac{n}{|n|}g_3' - C_1\cos\varphi - C_2\sin\varphi \\ &= \frac{n}{|n|}g_4 + \frac{n}{|n|}h_4 - C_1\cos\varphi - C_2\sin\varphi \\ &= -g_1 - h_1 \end{aligned} \tag{6.37}$$

and

$$2ng_4 + 2|n|g_1 = 2|n|(C_1\cos\varphi + C_2\sin\varphi) \tag{6.38}$$

which brings ϖ_2 on the form

$$\varpi_2 = \kappa n\sin\varphi + 2|n|(C_1\cos\varphi + C_2\sin\varphi) \tag{6.39}$$

and similarly

$$\varpi_1 = -\kappa|n|\cos\varphi + 2n(C_1\sin\varphi - C_2\cos\varphi)\ . \tag{6.40}$$

The perpendicular components of $\boldsymbol{u}$ are then uniquely determined in terms of $\boldsymbol{C}$

$$\begin{aligned}\boldsymbol{u}_\perp &= b_I[2C_1\boldsymbol{N} + (\kappa\frac{n}{|n|} + 2C_2)\boldsymbol{B}] + b_R[(\kappa + 2\frac{n}{|n|}C_2)\boldsymbol{N} - 2\frac{n}{|n|}C_1\boldsymbol{B}] \\ &= b_I[\kappa\frac{n}{|n|}\boldsymbol{B} + 2\boldsymbol{C}_\perp] + b_R[\kappa\boldsymbol{N} - 2\frac{n}{|n|}\boldsymbol{T}\times\boldsymbol{C}]\end{aligned} \tag{6.41}$$

It is always possible to set the tangential velocity, which is void of physical meaning, to zero by a time-dependent reparametrization $s \to s(t)$. The exact result for the velocity of the vortex filament is then, by use of the definition of $\boldsymbol{u}$ in Eq. (6.25),

$$\begin{aligned}\dot{\boldsymbol{X}} &= b_I\left(\kappa\frac{n}{|n|}\boldsymbol{B} + 2(\nabla_\perp\theta + \boldsymbol{C}_\perp) - 2\frac{n}{|n|}\boldsymbol{T}\times\nabla\ln w\right) \\ &\quad + b_R\left(\kappa\boldsymbol{N} - 2\nabla_\perp\ln w - 2\frac{n}{|n|}\boldsymbol{T}\times(\nabla\theta + \boldsymbol{C})\right)\ ,\end{aligned} \tag{6.42}$$

where $(\ )_\perp = -\boldsymbol{T}\times[\boldsymbol{T}\times(\ )]$ and the fields on the right-hand side are to be evaluated at the filament position $\boldsymbol{X}(s,t)$. The exact two-dimensional result is obtained as $\kappa \to 0$.

The value of $\dot{\boldsymbol{X}}$ is independent of the choice of gauge for R and χ. Indeed, substituting $\boldsymbol{C}$ from Eq. (6.17) into Eq. (6.42) we obtain the manifestly invariant expression

$$\begin{aligned}\dot{\boldsymbol{X}} &= \lim_{r\to 0}\left[b_I\left(\kappa\frac{n}{|n|}\boldsymbol{B} + 2\nabla_\perp S - 2\frac{n}{|n|}\boldsymbol{T}\times\nabla\ln|A|\right)\right. \\ &\quad \left. + b_R\left(\kappa\boldsymbol{N} - 2\nabla_\perp\ln|A| - 2\frac{n}{|n|}\boldsymbol{T}\times\nabla S\right)\right]\ .\end{aligned} \tag{6.43}$$

in which the filament velocity is written in terms of gradients of the amplitude and phase of the original complex field A. The function $P(A, A^*)$ does not enter explicitly in the expressions (6.42)–(6.43) for the velocity. However, since A near the filament is determined by the differential equation (6.1), the velocity nevertheless depends indirectly on P.

In the coupled system (6.21) and (6.22) the coefficients of the $r^{-1}\ln\kappa r$ and $(\ln\kappa r)^2$ terms vanish by virtue of Eqs. (6.31) and (6.32). In the general derivation, where we allow for powers of logarithms in $\nabla\chi$, $\nabla\ln R$ and on the right-hand side

of Eq. (6.17), the cancellation of the coefficients of $r^{-1}\ln\kappa r$ and $(\ln\kappa r)^m$, $m \geq 1$, implies that the right-hand side of Eq. (6.17) must be regular, and the vortex velocity is unchanged.

The velocity of the central filament of a vortex gets contributions from the curvature κ of the filament and from local gradients of the amplitude $|A|$ and phase S of the complex field. A cylindrically symmetric solution $A = \rho(r)\exp[i(\psi(r) + n\varphi - \omega t)]$, for which $\rho = |A| \sim r^{|n|}$ and $\psi'(0) = 0$, contributes nothing to the velocity and corresponds to a straight (or two-dimensional) isolated vortex at rest with respect to the lab frame. Non-zero gradient contributions appear as a result of deviations from cylindrical symmetry in $|A|$ and S. In a symmetric gauge with $\boldsymbol{C} = \boldsymbol{0}$, these deviations are represented by w and θ. The asymmetries arise from the presence of other vortices, system boundaries, or (in three dimensions) other segments of the same filament, causing the vortex to move.

In the $\boldsymbol{C} = \boldsymbol{0}$ gauge the expression (6.42) reproduces a variety of results obtained previously for special cases. For $\kappa = 0$ and $\nabla \ln w \approx 0$ it reduces to Eq. (6.2) that corresponds to a two-dimensional dilute system [75]. In the GPG limit $b_R = 0$ the expression (6.42) coincides with that derived by Lee [83], who used a different method to find the velocity. For $b_I = 0$, Eq. (6.1) describes the nonlinear diffusion of two fluid components with identical diffusion constants. In this limit the contribution to $\dot{\boldsymbol{X}}$ from curvature, $b_R\kappa\boldsymbol{N}$, agrees with the result of Ref. [55].

The expressions (6.42)–(6.43) for the velocity are exact also for an arbitrarily small distance between filaments. This makes the formulation well suited for theoretical or numerical investigations of local vortex interactions, such as crossing, merging and intercommutation, in which the vortex cores overlap [84, 85]. We caution that the GPG equation does not provide a realistic model for the core of a superfluid vortex, since there the core width is comparable to interatomic distances. For magnetic flux vortices in a superconductor, however, the core width is much larger and a classical description is justified. Such vortices are solutions of Eq. (6.1) with the substitution $\nabla \to \nabla + 2ie\boldsymbol{A}/(\hbar c)$, where $\boldsymbol{A}$ is the vector potential and $2e$ is the charge of a Cooper pair. The corresponding filament velocity is easily obtained by adding $2e\boldsymbol{A}/(\hbar c)$ to $\nabla\theta$ in Eq. (6.42) or to ∇S in Eq. (6.43) [83].

Bibliography

[1] L. F. Richardson, *Atmospheric Diffusion shown on a Distance-Neighbour Graph*, Proc. R. Soc. (London) A **110**, 709 (1926).

[2] M. Faraday, *On a peculiar class of acoustical Figures; and on certain forms assumed by groups of particles upon vibrating elastic surfaces*, Phil. Trans. R. Soc. London **52**, 299 (1831).

[3] Lord Rayleigh, *On the crispations of fluid resting upon a vibrating support*, Phil. Mag. **16**, 50 (1883).

[4] B. J. Gluckman, P. Marc, J. Bridger, and J. P. Gollub, *Time averaging of chaotic spatiotemporal wave patterns*, Phys. Rev. Lett. **71**, 2034 (1993); B. J. Gluckman, C. B. Arnold, and J. P. Gollub, *Statistical studies of chaotic wave patterns*, Phys. Rev. E **51** 1128, (1995).

[5] B. Christiansen, P. Alstrøm, and M. T. Levinsen, *Ordered Capillary-Wave States: Quasicrystals, Hexagons, and Radial Waves*, Phys. Rev. Lett. **68**, 2157 (1992).

[6] B. Christiansen, P. Alstrøm, and M. T. Levinsen, *Dissipation and ordering in capillary waves at high aspect ratios*, J. Fluid Mech. **291**, 323 (1995).

[7] S. T. Milner, *Square patterns and secondary instabilities in driven capillary waves*, J. Fluid Mech. **225**, 81 (1991).

[8] J. W. Miles, *On Faraday waves*, J. Fluid Mech. **248**, 671 (1993).

[9] P. L. Hansen and P. Alstrøm, *Perturbation theory of parametrically driven capillary waves at low viscosity*, preprint.

[10] R. Ramshankar, D. Berlin, and J. P. Gollub, *Transport by capillary waves. Part I: Particle trajectories*, Phys. of Fluids A **2**, 1955 (1990).

[11] R. Ramshankar and J. P. Gollub, *Transport by capillary waves. Part II: Scalar dispersion and structure of the concentration field*, Phys. Fluids A **3**, 1344 (1991).

[12] P. Alstrøm, J. S. Andersen, W. I. Goldburg, and M. T. Levinsen, *Relative Diffusion in a Chaotic System: Capillary Waves in the Faraday Experiment*, Chaos, Solitons & Fractals **5**, 1455 (1995).

[13] L. D. Landau and E. M. Lifshitz, *Fluid Mechanics* (Pergamon, New York, 1959).

[14] J. Lighthill, *Waves in fluids* (Cambridge University Press, Cambridge, 1978).

[15] G. K. Batchelor, *Diffusion in a field of homogeneous turbulence. II. The relative motion of particles*, Proc. Cambr. Phil. Soc. **48**, 345 (1952).

[16] H. Stommel, *Horizontal diffusion due to oceanic turbulence*, J. Marine Research **8**, 199 (1949).

[17] J. O. Hinze, *Turbulence*, 2nd ed. (McGraw-Hill, 1975).

[18] A. N. Kolmogorov, *Energy dissipation in locally isotropic turbulence*, Dokl. Akad. Nauk SSSR **32**, 19 (1941).

[19] M. Lesieur, *Turbulence in Fluids* (Kluwer Academic Publishers, 2nd revised ed., Dordrecht, 1990) Ch. IX; R. H. Kraichnan and D. Montgomery, *Two-dimensional turbulence*, Rep. Prog. Phys. **43**, 547 (1980).

[20] S. Grossmann, *Diffusion by Turbulence*, Ann. Phys. **47**, 577 (1990).

[21] P. Morel and M. Larcheveque, *Relative Dispersion of Constant-Level Balloons in the 200-mb General Circulation*, J. Atmos. Sci. **31**, 2189 (1974).

[22] H. G. E. Hentschel and I. Procaccia, *Fractal nature of turbulence as manifested in turbulent diffusion*, Phys. Rev. A **27**, 1266 (1983).

[23] A. Okubo, *Oceanic diffusion diagrams*, Deep-Sea Res. **18**, 789 (1971).

[24] R. E. Davis, *Lagrangian ocean studies*, Ann. Rev. Fluid Mech. **23**, 43 (1991).

[25] I. Procaccia and P. Constantin, *The Fractal Geometry of the Level Sets of a Contaminant Dispersed by Chaotic Surface Waves*, Europhys. Lett. **22**, 689

(1993); P. Constantin and I. Procaccia, *The geometry of turbulent advection: sharp estimates for the dimension of level sets*, Nonlinearity **7**, 1045 (1994).

[26] See e.g. F. Belin, J. Maurer, P. Tabeling, and H. Willaime, *New Measurements on Small Scale Intermittency in Fully Developed Turbulence*, Physica Scripta **T67**, 101 (1996).

[27] R. Benzi, S. Ciliberto, C. Baudet, G. R. Chavarria, and R. Tripiccione, *Extended self-similarity in the dissipation range of fully developed turbulence*, Europhys. Lett. **24**, 275 (1993).

[28] R. Benzi, S. Ciliberto, R. Tripiccione, C. Baudet, F. Massaioli, and S. Succi, *Extended self-similarity in turbulent flows*, Phys. Rev. E **48**, R29 (1993).

[29] A. S. Monin and A. M. Yaglom, *Statistical Fluid Mechanics II* (The MIT Press, Cambridge, Massachusetts, 1987).

[30] Private communication, P. Alstrøm and R. Benzi.

[31] V. E. Zakharov, V. S. L'vov, and G. Falkovich, *Kolmogorov Spectra of Turbulence I* (Springer-Verlag, Berlin, 1992).

[32] J. Mathews and R. L. Walker, *Mathematical Methods of Physics* (Addison-Wesley Publishing Company, Inc., Redwood City, California, 1970).

[33] V. E. Zakharov and N. N. Filonenko, Zh. Prikl. Mekh. Tekh. Fiz. **no. 5, volume 8**, 62 (1967) [*Weak Turbulence of Capillary Waves*, J. Appl. Mech. Tech. Phys. p. 37 (it has not been possible to find volume number and year, it is not printed on the pages concerned)].

[34] A. V. Kats and V. M. Kontorovich, Zh. Prikl. Mekh. Tekh. Fiz. **no. 6, volume?**, 97 (1974) [*Theory of Weak Turbulence of Waves on a Fluid Surface*, J. Appl. Mech. Tech. Phys. p. 810 (1976) (it has not been possible to find volume number, it is not printed on the pages concerned)].

[35] I. S. Gradshteyn and I. M. Ryzhik, *Table of Integrals, Series, and Products* (Academic Press, London, 1979).

[36] A. Provenzale, A. R. Osborne, A. D. Kirwan Jr., and L. Bergamasco, *The Study of Fluid Parcel Trajectories in Large-Scale Ocean Flows*, in: *Nonlinear Topics in Ocean Physics*, A. R. Osborne ed. (North-Holland, Amsterdam, 1991) p. 367.

[37] A. C. de Verdiere, *Lagrangian Eddy Statistics from Surface Drifters in the Eastern North Atlantic*, J. Mar. Res. **41**, 375 (1983).

[38] D. A. Booth, *Horizontal dispersion in the northeast Atlantic*, Deep-sea Res. **35**, 1937 (1988).

[39] B. G. Sanderson and D. Booth, *The fractal dimension of drifter trajectories and estimates of horizontal eddy-diffusivity*, Tellus **43**A, 334 (1991).

[40] D. J. Tritton, *Physical Fluid Dynamics* (Clarendon Press, Oxford 1988).

[41] B. de Young and B. Sanderson, *The Circulation and Hydrography of Conception Bay, Newfoundland*, Atmosphere-Ocean **33**, 135 (1995).

[42] A. R. Osborne, A. D. Kirwan Jr., A. Provenzale, and L. Bergamasco, *Fractal drifter trajectories in the Kuroshio extension*, Tellus **41**A, 416 (1989).

[43] B. B. Mandelbrot, *The Fractal Geometry of Nature* (Freeman, San Francisco, 1982).

[44] N. Wiener, *Nonlinear Problems in Random Theory* (John Wiley & Sons Inc., New York, 1958).

[45] J. Feder, *Fractals* (Plenum, New York, 1988).

[46] K. B. Lauritsen, M. Sahimi, and H. J. Herrmann, *Effect of quenched and correlated disorder on growth phenomena*, Phys. Rev. E **48**, 1272 (1993).

[47] M. C. Cross and P. C. Hohenberg, *Pattern formation outside of equilibrium*, Rev. Mod. Phys. **65**, 851 (1993).

[48] Y. Kuramoto *Chemical Oscillations, Waves, and Turbulence* (Springer-Verlag, Berlin, 1984).

[49] P. Coullet, L. Gil, and J. Lega, *Defect-Mediated Turbulence*, Phys. Rev. Lett. **62**, 1619 (1989); L. Gil, J. Lega, and J. L. Meunier, *Statistical properties of defect-mediated turbulence*, Phys. Rev. A **41**, 1138 (1990); T. Bohr, A. W. Pedersen, and M. H. Jensen, *Transition to turbulence in a discrete Ginzburg-Landau model*, Phys. Rev. A **42**, 3626 (1990).

[50] I. S. Aranson, L. Aranson, L. Kramer, and A. Weber, *Stability limits of spirals and traveling waves in nonequilibrium media*, Phys. Rev. A **46**, R2992 (1992).

[51] G. Huber, P. Alstrøm and T. Bohr, *Nucleation and transients at the onset of vortex turbulence*, Phys. Rev. Lett. **69**, 2380 (1992).

[52] H. Chaté and P. Manneville, *Phase Diagram of the Two-Dimensional Complex Ginzburg-Landau Equation*, Physica A **224**, 348 (1996).

[53] P. S. Hagan, *Spiral waves in reaction-diffusion equations*, SIAM J. Appl. Math. **42**, 762 (1982).

[54] A. T. Winfree and S. H. Strogatz, *Singular filaments organize chemical waves in three dimensions*, Physica D **8**, 35 (1983).

[55] J. P. Keener, *The dynamics of three-dimensional scroll waves in excitable media*, Physica D **31**, 269 (1988); J. P. Keener and J. J. Tyson, *Helical and circular scroll wave filaments*, Physica D **44**, 191 (1990).

[56] See e.g. R. Montagne, E. Hernández-García, and M. San Miguel, *Winding Number Instability in the Phase-Turbulence Regime of the Complex Ginzburg-Landau Equation*, Phys. Rev. Lett. **77**, 267 (1996).

[57] For relativistic vortices this is shown in M. Goodband and M. Hindsmarsh, *Bound States and Instabilities of Vortices*, Phys. Rev. D **52**, 4621 (1995).

[58] A. T. Dorsey, *Vortex motion and the Hall effect in type-II superconductors: A time-dependent Ginzburg-Landau theory approach*, Phys. Rev. B **46**, 8376 (1992).

[59] M. Tinkham, *Introduction to Superconductivity*, (McGraw-Hill, New York, 1975).

[60] V. T. Ginzburg and P. Pitaevskii, Zh. Eksp. Teor. Fiz. **34**, 1240 (1958) [*On the theory of superfluidity*, Sov. Phys. JETP **7**, 858 (1958)]; E. P. Gross, *Structure of a Quantized Vortex in Boson Systems*, Nuovo Cimento **20**, 454 (1961).

[61] E. Madelung, *Quantentheorie in hydrodynamischer Form*, Z. Phys. **40**, 322 (1927).

[62] Y. Oono and S. Puri, *Computationally Efficient Modeling of Ordering of Quenched Phases*, Phys. Rev. Lett. **58**, 836 (1987).

[63] G. Huber, *The Onset of Vortex Turbulence*, Ph.D. dissertation, Boston University (1993).

[64] X.-G. Wu and R. Kapral, *Chemical turbulence and phase resetting dynamics*, J. Chem. Phys. **94**, 1411 (1991).

[65] T. Bohr and A. Pikovsky, *Anomalous Diffusion in the Kuramoto-Sivashinsky Equation*, Phys. Rev. Lett. **70**, 2892 (1993).

[66] J. L. Hansen, *Large Scale Structures and Particle Motion in Chaotic Dynamical Systems* (Thesis, Niels Bohr Institute, 1997).

[67] Y. Kuramoto, *Diffusion-Induced Chaos in Reaction Systems*, Suppl. Progr. Theor. Phys. **64**, 346 (1978).

[68] H. Sakaguchi, *Phase Turbulence and Mutual Entrainment in a Coupled Oscillator System*, Progr. Theor. Phys. **83**, 169 (1990); H. Sakaguchi, *Breakdown of the Phase Dynamics*, Progr. Theor. Phys. **84**, 792 (1990).

[69] A. Torcini, *Order Parameter for the Transition from Phase to Amplitude Turbulence*, Phys. Rev. Lett. **77**, 1047 (1996).

[70] H. Chaté, *Spatiotemporal intermittency regimes of the one-dimensional complex Ginzburg-Landau equation*, Nonlinearity **7**, 185 (1994).

[71] D. Egolf and H. Greenside, *Characterization of the transition from defect- to phase-turbulence*, Phys. Rev. Lett. **74**, 1751 (1995).

[72] P. Manneville and H. Chaté, *Phase turbulence in the two-dimensional complex Ginzburg-Landau equation*, Physica D **96**, 30 (1996).

[73] I. S. Aranson, L. Kramer, and A. Weber, *Theory of interaction and bound states of spiral waves in oscillatory media*, Phys. Rev. E **47**, 3231 (1993).

[74] M. Gabbay, E. Ott, and P. N. Guzdar, *Motion of Scroll Wave Filaments in the Complex Ginzburg-Landau Equation*, Phys. Rev. Lett. **78**, 2012 (1997).

[75] S. Rica and E. Tirapegui, *Analytic description of a state dominated by spiral defects in two-dimensional extended systems*, Physica D **48**, 396 (1991).

[76] C. Elphick and E. Meron, *Dynamics of phase singularities in two-dimensional oscillating systems*, Physica D **53**, 385 (1991).

[77] A. L. Fetter, *Vortices in an Imperfect Bose Gas. IV. Translational Velocity*, Phys. Rev. **151**, 100 (1966).

[78] M. Peach and J. S. Koehler, *The forces exerted on dislocations and the stress field produced by them*, Phys. Rev. **80**, 436 (1950).

[79] K. Kawasaki, *Topological Defects and Non-Equilibrium*, Prog. Theor. Phys. Suppl. **79**, 161 (1984).

[80] U. Ben-Ya'acov, *Unified dynamics of quantum vortices*, Nucl. Phys. B **382**, 597 (1992).

[81] See e.g. M. Spivak, *A Comprehensive Introduction to Differential Geometry*, 2nd edition, Volume II, Chapter 1 (Publish or Perish, Wilmington, Delaware, 1979).

[82] G. K. Batchelor, *An Introduction to Fluid Dynamics* (Cambridge University Press, 1970).

[83] K. Y. Lee, *Vortices and sound waves in superfluids*, CU-TP-652, NI-94-013, cond-mat/9409046.

[84] U. Ben-Ya'acov, *Mechanism of quantum vortices' intercommutation*, Phys. Rev. D **52**, 1065 (1995).

[85] J. Dziarmaga, *Dynamics of Overlapping Vortices in Complex Scalar Fields*, Acta Phys. Pol. **27**, 1943 (1996); J. Dziarmaga, *String model for short range interactions of vortices*, Phys. Rev. D **48**, 3809 (1993).

Paper I

E. Schröder, J. S. Andersen, M. T. Levinsen, P. Alstrøm, and W. I. Goldburg, *Relative Particle Motion in Capillary Waves*, Phys. Rev. Lett. **76**, 4717 (1996).

Paper II

G. Huber, E. Schröder, and P. Alstrøm, *Self-diffusion and relative diffusion in defect turbulence*, Physica D **96**, 1 (1996).

Paper III

E. Schröder, M. T. Levinsen, and P. Alstrøm, *Fractional Brownian Motion of Particles in Capillary Waves*, preprint [to appear in Physica A **239** (1997)].

Paper IV

O. Törnkvist and E. Schröder, *Vortex Dynamics in Dissipative Systems*, Phys. Rev. Lett. **78**, 1908 (1997).

Paper V

A. E. Hansen, E. Schröder, P. Alstrøm, and M. T. Levinsen, *Fractal Particle Trajectories in Capillary Waves, Imprint of Wavelength*, preprint (submitted for publication).